

國立臺灣海洋大學

河海工程學系

碩士學位論文

指導教授：陳正宗 終身特聘教授

加法定理及疊加技巧在含圓形邊界之聲場與
水波問題之應用

Applications of the addition theorem and
superposition technique for acoustic and water
wave problems with circular boundaries

研究生：林羿州 撰

中華民國 98 年 7 月



加法定理及疊加技巧在含圓形邊界之聲場與水
波問題之應用

Applications of the addition theorem and superposition
technique for acoustic and water wave problems with
circular boundaries

研究生：林羿州

Student : Yi-Jhou Lin

指導教授：陳正宗

Advisor : Jeng-Tzong Chen

國立臺灣海洋大學
河海工程學系
碩士論文

A Thesis
Submitted to Department of Harbor and River Engineering
College of Engineering
National Taiwan Ocean University
In Partial Fulfillment of the Requirements
for the Degree of
Master of Science
in
Harbor and River Engineering
July 2009
Keelung, Taiwan, Republic of China

中華民國 98 年 7 月



謝誌

時光飛逝，在努力不懈的學習過程中，隨著論文一章接著一章的完成，也接近了尾聲。回憶當初，感謝陳正宗終身特聘教授讓我有機會加入力學聲響振動實驗室學習並不辭辛勞的指導我，讓我學習到求學之路需要深思熟慮以及嚴謹的態度去面對。也發現持之以恆地努力才是做學問的唯一道路。此外，也感謝師母在生活上的照顧。在撰寫論文過程中，從老師嚴謹審閱修改的態度中，深刻體認了『學問如登山，點滴在心頭』。再者，感謝岳景雲老師提供陳一豪學長論文成果比對，讓我對自己研究的結果如吃了定心丸，使我對自己的研究有了更加有信心。在論文口試期間，承蒙本系岳景雲博士及范佳銘博士、宜蘭大學土木工程系李洋傑博士、中華大學土木與工程資訊學系呂志宗博士、高雄海洋科技大學造船系陳義麟博士、中華技術學院機械系李為民博士、宜蘭大學土木系陳桂鴻博士、中華技術學院航空機械系呂學育博士、屏東科技大學教學資源中心徐文信博士等九位口試委員，不吝指教並提供珍貴意見，讓我在口試答辯過程學習到以不同的觀點去審視問題。在此，深深感謝各位委員，使得本論文瑕疵能減到最少。

在碩士兩年的生活中，很慶幸自己能遇到一群肯付出不求回報的人。在課業及撰寫論文過程當中接受到阿德學長、世璿學長及周克勳學長的提攜，以及對於在同一陣線上聖凱及宏治同學所給予的鼓勵與加油，感到十分溫暖。也感謝相處兩年的朋友：圍捷、清男、仲男、維軒、豐任及明修求學過程中的鼓勵。此外，也在此感謝尚儒、家瑋、天賜、建鋒、振鈞、文哲及胤祥學弟的協助與幫忙。以及毓玲、雅馨、雅鈞、汶珊、佑勳、志豪及宇志學弟妹分擔研究室瑣碎雜務。更要感謝國科會計畫 NSC95-2155-M-019-003-MY2 提拱之碩士生研究助學金，讓我在做研究的過程中無經濟之壓力，能更加專心於學業上。

最後將此篇論文獻給我的家人，在求學過程的包容與體諒，希望自己是您們心中永遠的驕傲。

林羿州 謹誌於

國立台灣海洋大學河海工程學系

中華民國九十八年七月二十八日

Abstract

Based on the null-field integral equation approach, we introduce the degenerate kernel, namely the addition theorem, Fourier series and adaptive observer system to construct the linear algebraic system for solving Helmholtz problems. After obtaining the unknown Fourier coefficient, a linear algebraic system is obtained, the interior potential can be calculated. By introducing the superposition technique, a problem can be decomposed into two parts. One is the fundamental solution of free field and the other is an infinite plane with circular boundaries subject to the specified boundary conditions derived from the addition theorem. After superposing the two solutions, the governing equation and boundary condition are both satisfied. Five advantages: (1) mesh-free generation (2) well-posed model, (3) principal value free (4) elimination of boundary-layer effect (5) exponential convergence, are achieved.

Finally, a general-purpose program for deriving the Helmholtz problems with arbitrary number of circular boundaries and/or cylinders of arbitrary radii and various positions involving the Dirichlet or the Neumann boundary condition was developed.

Two applications in acoustic problem with a point source and water wave problems, were done. Besides, the effect of porous parameter and disorder on the force in case of near-trapped modes was also examined.

Keywords: null-field integral equation, degenerate kernel, addition theorem, Fourier series, adaptive observer system, Helmholtz problems.

摘要

本文利用零場積分方程搭配退化核以及加法定理、傅立葉級數與自適性觀察座標系統求解 Helmholtz 問題並建立線性代數系統。未知的傅立葉係數可藉由線性代數系統輕易地解出，進而求得域內點場量。引入疊加技巧後，可將問題拆解成兩部份。其中一部份為基本解自由場問題與另一部份為無限域含特定邊界條件之圓形邊界值問題，而此特定邊界條件可由加法定理求得級數展開型式。將兩部份的解作疊加之後，控制方程及邊界條件均會滿足。在本方法中有五大優點 (1) 無需網格；(2) 良態模式；(3) 無需主值計算；(4) 無邊界層效應；(5) 指數收斂。最後，本文發展一套程式，求解含任意數目、不同大小與位置的圓孔洞和/或圓柱之 Dirichlet、Neumann 邊界條件之赫姆茲方程問題。除此之外，文中針對點聲源與水波問題進行數值驗證，並且探討錯置與孔隙圓柱對近乎陷阱模態的影響。

關鍵字：零場積分方程、退化核、加法定理、傅立葉級數、自適性觀察座標系統、赫姆茲問題。

Applications of the addition theorem and superposition technique for acoustic and water wave problems with circular boundaries

Contents

Contents	I
Figure captions	III
Notations	VIII
Abstract	X
摘要	XI
Chapter 1 Introduction	
1.1 Overview and motivation	1
1.2 Organization of the thesis	5
Chapter 2 Scattering of sound from point sources by multiple circular cylinders using addition theorem and superposition technique	
Summary	12
2.1 Introduction	12
2.2 Null-field integral formulation for a typical BVP	14
2.2.1 Problem statements for BVP without sources	14
2.2.2 Dual null-field integral formulation- the conventional version	15
2.2.3 Dual null-field integral formulation- the present version	15
2.2.4 Expansions of the fundamental solution and boundary density	16
2.2.4.1 Degenerate (separable) kernel for fundamental solutions	16
2.2.4.2 Fourier series expansion for boundary densities	18
2.2.5 Adaptive observer system	18
2.2.6 Linear algebraic equation	19
2.3 Methods of solution	19
2.3.1 Problem statements	19

2.3.2 Green's function using the addition theorem and superposition technique	20
2.3.3 Green's third-identity approach	20
2.3.4 Equivalence between the solution using the Green's third identity and superposition technique	20
2.4 An illustrative example	21
2.5 Conclusions	23
Chapter 3 Water wave interaction with surface-piercing porous cylinders using the null-field integral equations	
Summary	37
3.1 Introduction	37
3.2 Problem statement and integral formulation	40
3.2.1 Problem statement	40
3.2.2 Linear Algebraic Equation	42
3.2.3 Perturbation of ordered cylinders arrangements	45
3.3 Illustrative examples	45
3.4 Conclusions	48
Chapter 4 Conclusions and further research	
4.1 Conclusions	94
4.2 Further research	95
References	97
Appendix	
Appendix 1 Limiting case of Helmholtz problem to Laplace case ($k \rightarrow 0$)	102

Figure captions

Figure 1-1 (a)	Bump contour	7
Figure 1-1 (b)	Limiting contour	7
Figure 1-2	Mesh generation	8
Figure 1-3	Boundary value problems with arbitrary boundaries	9
Figure 1-4	Near-trapped modes in physics and engineering	10
Figure 1-5	The frame of the thesis	11
Figure 2-6	An infinite plane with arbitrary number of circular cylinders subject to the Dirichlet or Neumann boundary conditions	24
Figure 2-2	Sketch of the null-field integral equation in conjunction with the adaptive observer system	24
Figure 2-3	Infinite plane with arbitrary number of circular cylinders subject to a point sound source at ξ	25
Figure 2-4 (a)	Free field of the fundamental solution	26
Figure 2-4 (b)	Radiation field (a typical BVP)	26
Figure 2-5	Flowchart of the present approach	27
Figure 2-6	An infinite plane with two equal circular cylinders subject to a point sound source	28
Figure 2-7	Distribution potential on the artificial boundaries in the free field (upper part: series-form, lower part: closed-form, $M=20$)	29
Figure 2-8	Distribution potential on the artificial boundaries in the free field versus polar angle	30
Figure 2-9	Relative amplitude of total field versus the probe location y ($M=20$)	30
Figure 2-10 (a)	Convergence test of Parseval's sum for $\partial G(\mathbf{x}, \xi) / \partial n_x$ (real part)	31
Figure 2-10 (b)	Convergence test of Parseval's sum for $\partial G(\mathbf{x}, \xi) / \partial n_x$ (imaginary part)	31

Figure 2-11	Relative amplitude of total field versus the probe location ($M = 20$)	32
Figure 2-12	Relative amplitude of total field versus the probe location ($M = 20$)	32
Figure 2-13	Relative amplitude of total field versus $2b/\lambda$ ($a = 0.2\lambda$ and $M = 20$)	33
Figure 2-14	Relative amplitude of total field versus $2b/\lambda$ ($a = 0.24\lambda$ and $M = 20$)	33
Figure 2-15	Relative amplitude of total field versus $2b/\lambda$ ($a = 0.318\lambda$ and $M = 20$)	34
Figure 2-16	Relative amplitude of total field versus $2b/\lambda$ ($a = 0.477\lambda$ and $M = 20$)	34
Figure 2-17	Infinite plane with two circular holes subject to the Neumann boundary condition under the source point	35
Figure 2-18	Contour of potential using limiting case of $k \rightarrow 0$	36
Figure 2-19	Contour of potential using the image method	36
Figure 3-1	Problem statement of water waves with an array of vertical cylinders	50
Figure 3-2 (a)	Water wave problem with multiple circular cylinders	51
Figure 3-2 (b)	Infinite domain with multiple cylinders subject to incident water wave	51
Figure 3-2 (c)	An interior Helmholtz problem for each circular cylinder	51
Figure 3-2 (d)	An Infinite domain subject to the incident water wave	51
Figure 3-2 (e)	An exterior Helmholtz problem an infinite domain	51
Figure 3-3	Sketch of the BIE for the domain point	52
Figure 3-4	Configuration of (a) four cylinders and (b) sixteen cylinders	52
Figure 3-5	Near-trapped mode for the four cylinders at $ka=4.08482$ ($a/b=0.8, G=0.0, \tau = 0.0, H = 2$)	53
Figure 3-6	Surface-piercing porous cylinders at $ka=4.08482$ ($a/b=0.8, M=20, G=1.0, \tau = 0.0, H = 2$)	54

Figure 3-7	Near-trapped mode for the ordered pile array at $ka=4.08482$ ($a/b=0.8, G=0.0, M=20, \tau = 0.0, H = 2$)	54
Figure 3-8	Near-trapped mode for the six cylinders at $ka=2.92921$ ($a/b=0.8,$ $G=0.0, \tau = 0.0, H = 2$)	55
Figure 3-9	Near-trapped mode for the ordered pile array at $ka=2.928911$ ($a/b=0.8, G=0.0, M=20, \tau = 0.0, H = 2$)	56
Figure 3-10	Near-trapped mode for the ordered pile array at $ka=2.92921$ ($a/b=0.8, G=0.0, M=20, \tau = 0.0, H = 2$)	56
Figure 3-11	Near-trapped mode for the ordered pile array at $ka=4.08482$ ($a/b=0.8, G=0.0, M=20, \tau = 0.0, H = 2$)	58
Figure 3-12	Horizontal force on the corresponding cylinder of the ordered pile array ($kb/\pi=1.625293, a/d=0.8, M=20, \tau = 0.0, H = 2$)	59
Figure 3-13	Suppression of near-trapped modes by using disorder ($\tau = 0.1, H=2$) [20]	60
Figure 3-14	Suppression of near-trapped modes by using disorder ($a/b=0.8,$ $M=20, H = 2$)	62
Figure 3-15	Free surface elevations for a perturbation of position ($kd/\pi = 1.625293, a/b=0.8, M=20, H = 2$)	65
Figure 3-16	Contour plots of free-surface elevation of a single impermeable cylinder ($G=0.0, \theta_{inc} = 0^\circ, h/a = 5$ and $ka = \pi/2, H = 2$)	66
Figure 3-17	Free-surface elevation of the single impermeable cylinder ($G=0.0, \theta_{inc} = 0^\circ, h/a = 5, ka = \pi/2, H = 1$)	67
Figure 3-18	Contour plots of free-surface elevation of a single porous cylinder ($G=1.0, \theta_{inc} = 0^\circ, h/a = 5$ and $ka = \pi/2, H = 2$)	68
Figure 3-19	Free-surface elevation of a single porous cylinder ($G=1.0, \theta_{inc} = 0^\circ, h/a = 5$ and $ka = \pi/2, H = 1$)	69
Figure 3-20	Contour plots of free-surface elevation of the four impermeable cylinders ($G=0.0, \theta_{inc} = 0^\circ, h/a = 5, 2b/a = 4$ and $ka = \pi/2, H = 2$)	70

Figure 3-21	Free-surface elevation of the arrays of four impermeable cylinders arrays ($G=0.0$, $\theta_{inc} = 0^\circ$, $h/a = 5$, $2b/a = 4$ and $ka = \pi/2$, $H = 1$)	71
Figure 3-22	Contour plots of free-surface elevation of the four porous cylinders ($G=1.0$, $\theta_{inc} = 0^\circ$, $h/a = 5$, $2b/a = 4$ and $ka = \pi/2$, $H = 2$)	72
Figure 3-23	Free-surface elevation of the arrays of four porous cylinders. ($G=1.0$, $\theta_{inc} = 0^\circ$, $h/a = 5$, $2b/a = 4$ and $ka = \pi/2$, $H = 1$)	73
Figure 3-24	Contour plots of free-surface elevation of the four impermeable cylinders ($G=0.0$, $\theta_{inc} = 45^\circ$, $h/a = 5$, $2b/a = 4$ and $ka = \pi/2$, $H = 2$)	74
Figure 3-25	Free-surface elevation of the arrays of four impermeable cylinders ($G=0.0$, $\theta_{inc} = 45^\circ$, $h/a = 5$, $2b/a = 4$ and $ka = \pi/2$, $H = 1$)	75
Figure 3-26	Contour plots of free-surface elevation of the four porous cylinders ($G=1.0$, $\theta_{inc} = 45^\circ$, $h/a = 5$, $2b/a = 4$ and $ka = \pi/2$, $H = 2$)	76
Figure 3-27	Free-surface elevation of the four-cylinder array ($G=1.0$, $\theta_{inc} = 45^\circ$, $h/a = 5$, $2b/a = 4$ and $ka = \pi/2$, $H = 1$)	77
Figure 3-28	Contour plots of free-surface elevation of the four cylinders ($\theta_{inc} = 0^\circ$, $h/a = 5$, $2b/a = 8$ and $ka = \pi/2$, $H = 2$)	78
Figure 3-29	Free-surface elevation of the arrays of four impermeable cylinders ($G=0.0$, $\theta_{inc} = 0^\circ$, $h/a = 5$, $2b/a = 8$ and $ka = \pi/2$, $H = 1$)	79
Figure 3-30	Free-surface elevation of the four porous cylinders ($G=1.0$, $\theta_{inc} = 0^\circ$, $h/a = 5$, $2b/a = 8$ and $ka = \pi/2$, $H = 1$)	80
Figure 3-31	Contour plots of free-surface elevation of the four cylinders ($\theta_{inc} = 45^\circ$, $h/a = 5$, $2b/a = 8$ and $ka = \pi/2$, $H = 2$)	81

Figure 3-32	Free-surface elevation of the arrays of four impermeable cylinders ($G=0.0$, $\theta_{inc} = 45^\circ$, $h/a = 5$, $2b/a = 8$ and $ka = \pi/2$, $H = 1$)	82
Figure 3-33	Free-surface elevation of the four porous cylinders ($G=1.0$, $\theta_{inc} = 45^\circ$, $h/a = 5$, $2b/a = 8$ and $ka = \pi/2$, $H = 1$)	83
Figure 3-34	Contour plots of free-surface elevation of the four cylinders ($\theta_{inc} = 0^\circ$, $h/a = 5$, $2b/a = 4$ and $ka = \pi/2$, $H = 2$)	84
Figure 3-35	Free-surface elevation of the arrays of four impermeable cylinders ($G=0.0$, $\theta_{inc} = 0^\circ$, $h/a = 5$, $2b/a = 4$ and $ka = \pi/2$, $H = 1$)	85
Figure 3-36	Free-surface elevation of the four porous cylinders ($G=1.0$, $\theta_{inc} = 0^\circ$, $h/a = 5$, $2b/a = 4$ and $ka = \pi/2$, $H = 1$)	86
Figure 3-37	Contour plots of free-surface elevation of the six cylinders ($\theta_{inc} = 0^\circ$, $h/a = 5$, $2b/a = 4$ and $ka = \pi/2$, $H = 2$)	87
Figure 3-38	Free-surface elevation of the six impermeable cylinder arrays ($G=0.0$, $\theta_{inc} = 45^\circ$, $h/a = 5$, $2b/a = 4$ and $ka = \pi/2$, $H = 1$)	88
Figure 3-39	Free-surface elevation of the six porous cylinders ($G=1.0$, $\theta_{inc} = 45^\circ$, $h/a = 5$, $2b/a = 4$ and $ka = \pi/2$, $H = 1$)	89
Figure 3-40	Contour plots of free-surface elevation of six cylinders ($\theta_{inc} = 0^\circ$, $h/a = 5$, $2b/a = 4$ and $ka = \pi/2$, $H = 2$)	90
Figure 3-41	Free-surface elevation of the six impermeable cylinders ($G=0.0$, $\theta_{inc} = 90^\circ$, $h/a = 5$, $2b/a = 4$ and $ka = \pi/2$, $H = 1$)	91
Figure 3-42	Free-surface elevation of the six porous cylinders ($G=1.0$, $\theta_{inc} = 90^\circ$, $h/a = 5$, $2b/a = 4$ and $ka = \pi/2$, $H = 1$)	92
Figure 3-43	Contour of the maximum free-surface elevation amplitude for porous cylinders ($a/b=0.8$, $G=1.0$, $\tau = 0$, $M=20$, $H = 2$)	93
Figure 3-44	Contour of the maximum free-surface elevation amplitude for the disorder and porous cylinders ($a/b=0.8$, $G=1.0$, $\tau = 0.1$, $M=20$, $H = 2$)	94

Notations

a	radius of a circular aperture
a_n, b_n	Fourier coefficients of boundary density $u(\mathbf{s})$
p_n, q_n	Fourier coefficients of boundary density $t(\mathbf{s})$
B	boundary
∇^2	Laplacian operator
G	the dimensionless parameter of porosity
k	wave number
$R.P.V.$	Riemann principal value
$C.P.V.$	Cauchy principal value
$H.P.V.$	Hadamard (or called Mangler) principal value
D	domain of interest
D^c	complementary domain
$H_0^{(1)}(\cdot)$	Zerth order Hankel function of the first kind
$J_n(\cdot)$	the n th order Bessel function of the first kind
$J'_n(\cdot)$	the derivative of $J_n(\cdot)$
$Y_n(\cdot)$	the n th order Bessel function of the second kind
$Y'_n(\cdot)$	the derivative of $Y_n(\cdot)$
$U(\mathbf{s}, \mathbf{x})$	kernel function in the singular formulation
$U^I(\mathbf{s}, \mathbf{x})$	degenerate kernel function of $U(\mathbf{s}, \mathbf{x})$ for $R \geq \rho$
$U^E(\mathbf{s}, \mathbf{x})$	degenerate kernel function of $U(\mathbf{s}, \mathbf{x})$ for $\rho > R$
$T(\mathbf{s}, \mathbf{x})$	kernel function in the singular formulation
$T^I(\mathbf{s}, \mathbf{x})$	degenerate kernel function of $T(\mathbf{s}, \mathbf{x})$ for $R > \rho$
$T^E(\mathbf{s}, \mathbf{x})$	degenerate kernel function of $T(\mathbf{s}, \mathbf{x})$ for $\rho > R$
$L(\mathbf{s}, \mathbf{x})$	kernel function in the hypersingular formulation
$L^I(\mathbf{s}, \mathbf{x})$	degenerate kernel function of $L(\mathbf{s}, \mathbf{x})$ for $R > \rho$
$L^E(\mathbf{s}, \mathbf{x})$	degenerate kernel function of $L(\mathbf{s}, \mathbf{x})$ for $\rho > R$
M	truncated terms of Fourier series
$M(\mathbf{s}, \mathbf{x})$	kernel function in the hypersingular formulation
$M^I(\mathbf{s}, \mathbf{x})$	degenerate kernel function of $M(\mathbf{s}, \mathbf{x})$ for $R \geq \rho$
$M^E(\mathbf{s}, \mathbf{x})$	degenerate kernel function of $M(\mathbf{s}, \mathbf{x})$ for $\rho > R$
N	number of the circles
\mathbf{n}	normal vector
\mathbf{n}_s	normal vector at the source point \mathbf{s}
\mathbf{n}_x	normal vector at the field point \mathbf{x}

R	radius of the outer boundary
\mathbf{x}	field point
\mathbf{s}	source point
(R, θ)	polar coordinate of \mathbf{s}
(ρ, ϕ)	polar coordinate of \mathbf{x}
$u(\mathbf{s})$	potential function on the source point \mathbf{s}
$u(\mathbf{x})$	potential function on the field point \mathbf{x}
$t(\mathbf{s})$	normal derivative of $u(\mathbf{s})$ at \mathbf{s}
$t(\mathbf{x})$	normal derivative of $u(\mathbf{x})$ at \mathbf{x}
\mathbf{u}^O	Fourier coefficients of boundary densities for the regions of ocean
\mathbf{u}^C	Fourier coefficients of boundary densities for the cylinder
\mathbf{u}^{inc}	Fourier coefficients of boundary densities for the incident
\mathbf{t}^O	normal derivative of \mathbf{u}^O
\mathbf{t}^C	normal derivative of \mathbf{u}^C
\mathbf{t}^{inc}	normal derivative of \mathbf{u}^{inc}
θ_{inc}	the angle of incident wave
ω	the circular frequency
A	the amplitude of incident wave
k	represents the wave number
μ	shear modulus
ρ_f	the density of the fluid
r	distance between the source point \mathbf{s} and the field point \mathbf{x} , $r \equiv \mathbf{x} - \mathbf{s} $
[\mathbf{U}]	influence matrix of the kernel function $U(\mathbf{s}, \mathbf{x})$
{ \mathbf{u} }	vector of Fourier coefficients $\{a_0 \ a_1 \ b_1 \ \cdots \ a_M \ b_M\}^T$
[\mathbf{T}]	influence matrix of the kernel function $T(\mathbf{s}, \mathbf{x})$
{ \mathbf{t} }	vector of Fourier coefficients $\{p_0 \ p_1 \ q_1 \ \cdots \ p_M \ q_M\}^T$
[\mathbf{I}]	identity matrix
$\delta(\mathbf{x} - \mathbf{s})$	Dirac-delta function
ξ	Location of a concentrated source and image source of Green's function
γ_j	random variable in the range [0,1]
p	the maximum permissible displacement
τ	global disorder parameter

Chapter 1 Introduction

1.1 Overview and motivation

Engineering analysis can be formulated as mathematical models for boundary value problems. For many problems involving complicated geometry shape, several kinds of modeling techniques have been developed including of finite difference method (FDM), the finite element method (FEM), the boundary element method (BEM), the scaled boundary finite-element method (SBFEM), the infinite element method (IEM) and the infinite boundary element method (IBEM). FDM approximates the derivatives in the differential equations which govern either problem using some types of truncated Taylor expansion and therefore express them in terms of the values at a number of discrete mesh points. FDM has main difficulties of the technique in the consideration of curved complex geometries and the application of boundary condition. For the case of general boundaries, the regular finite difference grid is unable to accurately reproduce the geometry of the problem. In the past decade, FEM has been widely applied to carry out many engineering problems. FEM utilizes a weighted residual method of the minimum potential energy theorem. The disadvantages of FEM are inconvenient in moving boundary problems, modeling infinite regions, concentrated load and need to deal with quantities of data, especially for three-dimensional problems and motion problems. BEM was developed as a response to the above difficulties. The method requires only discretization of the boundary thus reducing to deal with quantities of data in numerical implementation. BEM is suitable for the general boundaries regardless of the dimensionality of the problem. Because of the problem formulation in terms of fundamental solutions, discontinuities and singularities can be modeled without special difficulties. There are two independent boundary integral equations involved in the dual boundary element method (DBEM). One is the singular integral equation, and the other one is the hypersingular integral equation. Most of the previous researches have been focused on the singular boundary integral equation. The formulation of a singular boundary integral equation could provide sufficient conditions to ensure a unique solution to solve general problems. Since BEM utilizes the discretization concept of

FEM as well as the limitation, whether the supplement is meaningful or not depends on its absolutely superior area than FEM, BEM and meshless methods can be seen as a supplement of BEM of FEM. e. g., crack problems using the dual BEM and large-scale problems using fast multiple BEM.

Although BEM has been involved as an alternative numerical method for solving engineering problems, there are still five critical issues of concern. Five goals: (1) principal value free (2) well-posed model, (3) elimination of boundary-layer effect (4) mesh-free generation (5) exponential convergence, are the main focuses in this thesis.

(1) Principal value free

The conventional BEM faces the singularity. First, Guiggiani [27] has derived the free terms for Laplace and Navier equations using differential geometry and bump contour approach in Figure 1-1(a). Second, Gray and Manne [2] have employed a limiting process to ensure a finite value from an interior point to boundary by using a symbolic software in Figure 1-1(b). It is found that integral equation for the domain point and null-field integral equation yield the same algebraic equation when the limit is taken from the inside or from the outside of the region. Both limits represent the same algebraic equation that is an approximate counterpart of the boundary integral equation. For the case of a smooth boundary, the left-hand side term is $\pi u(x)$ or $\pi t(x)$ rather than $2\pi u(x)$ or $2\pi t(x)$ for the domain point or 0 for the point outside the domain. A proof for the Laplace case was done [8].

(2) Well-posed model

In order to avoid calculating the singular integrals, the null-field approach or fictitious BEM yields an ill-conditioned system. The influence matrix is not diagonally dominated and needs preconditioning. To move the fictitious boundary to the real boundary or to collocate the null-field point on the real boundary can make the linear algebraic system well-posed. However, singularity occurs. We may wonder whether it is possible to push the null-field point on the real boundary but free of calculating principal values for singular and hypersingular integrals. The answer is yes and the key idea is to describe the jump behavior of potential distribution in the separate region

using degenerate kernels for fundamental solutions. Therefore, degenerate kernels, namely separable kernels, are employed to represent the potential of the perforated domain which satisfies the governing equation.

(3) Elimination of boundary-layer effect

It is well known that boundary-layer effect appears in the conventional BEM. Chen and Hong in Taiwan [6] as well as Chen et al. in China [4] independently extended the idea of relative quantity to two regularization techniques which the boundary densities are subtracted by constant and linear terms. For the stress calculation, Sladek et al. [48] used a regularized version of the stress boundary integral equation (σ BEM) to compute the correct values of stresses close to the boundary. In this thesis, boundary-layer effect is eliminated by using the null-field integral equation approach.

(4) Mesh-free generation

In Figure 1-2, domain type methods, FEM and FDM, have been widely used to solve the engineering problem. Although BEM is free of domain discretization, boundary mesh generation is also required since collocation point is on the boundary. This thesis introduces the generalized Fourier coefficients for circular boundary free of mesh generation.

(5) Exponential convergence

BEM is very popular for boundary value problems with general geometries since it requires discretization on the boundary only. Regarding constant, linear and quadratic elements, the discretization scheme does not take the special geometry into consideration. Figure 1-3 shows randomly distributed apertures and/or inclusions with square, elliptic and circular shapes. Crouch and Mogilevskaya [19] utilized Somigliana's formula and Fourier series for elasticity problems with circular boundaries. Mogilevskaya and Crouch [40] have solved the problem of an infinite plane containing arbitrary number of circular inclusions based on the complex singular integral equation. They combined the series expansion technique with a complex boundary integral equation method. Kress has proved that the exponential convergence instead of linear

algebraic convergence in the BEM by using the degenerate kernels and Fourier expansion [30]. This thesis takes advantage of this fast rate of exponential convergence to derive the Green's function and solutions of plane wave problems with circular boundaries by using Fourier series in conjunction with degenerate kernels.

In this thesis, we employ the addition theorem and superposition technique to solve the scattering problem with multiple circular cylinders arising from point sound and plane wave. Using the superposition technique, the problem can be decomposed into two individual parts. One is the free-space fundamental solution. The other is a typical boundary value problem (BVP) with specified boundary conditions derived from the addition theorem by translating the fundamental solution. Following the success of the null-field integral formulation to solve the typical BVP of the Helmholtz equation with Fourier densities, the second-part solution is easily obtained after collocating the observation point exactly on the real boundary and matching the boundary condition. This method can be seen as a semi-analytical approach since errors attribute from the truncation of Fourier series.

Engineering applications containing multiple circular cylinders are demonstrated to see the validity of present method. In addition, the convergence test with various number of terms for Fourier series is studied. Problems of the point sound and plane wave are demonstrated to see the validity of present method. Since radial basis functions can represent body source [23-26, 52].

The trapped modes were studied in different fields, such as string vibration, hydraulic engineering, earthquake engineering, ocean engineering and physics as described below in Figure 1-4.

(1) String vibration

A string vibration can be modeled by a wave equation. When this system is subject to an incident wave, the spring may have a near-trapped mode under a certain spring layout and incident wave number.

(2) Hydraulic engineering

In hydraulic engineering, certain harmonic waves may exist at a depth discontinuity,

but are unable to propagate from shallow to deep water as shown in Fig. 1-4 [46, 33]. This phenomenon also belongs to one kind of near-trapped modes.

(3) Earthquake engineering

In earthquake engineering, surface wave may seriously result in damage for structures. For a thin-layer inclusion in a half-space medium, trapped wave may be present, e. g., Love wave [34] or Stonely wave.

(4) Ocean engineering

In ocean engineering, the construction of offshore platform is subjected to wave loads all the year. Researchers [20, 51] proposed a simplified model of linear theory to simulate the interaction between cylinders subject to the incident wave. In this analysis, a specific distance between cylinders in companion with a certain wave number may cause a near-trapped mode. Discussions on this topic will be addressed in this thesis.

(5) Quantum physics

The trapped mode, previously mentioned, occurs in physics as well as engineering. The bound state in a square-well potential in quantum mechanics is another case of trapped waves.

Duclos and Clément [20] extended to consider arrays of unevenly spaced cylinders, displaced randomly from a regular array according to a disorder parameter. However, Duclos and Clément [20] only considered the impermeable cylinders. On the other hand, Williams and Li [51] calculated the free-surface elevation and force for the porous cylinders. We not only consider the water-wave interaction with arrays of surface-piercing porous cylinders, but also consider the effect of disorder on the resultant force in case of near-trapped modes.

1.2 Organization of the thesis

In this thesis, the null-field integral equations in conjunction with the addition theorem and Fourier series are employed to solve the point sound sources and water wave problem. The focus of each chapter is summarized below:

In the chapter 2, we proposed the addition theorem and superposition technique to solve the scattering problem of two identical cylinders subject to a point source. Regarding the BVP with circular boundaries, we have proposed a BIEM formulation by using degenerate kernels, null-field integral equation and Fourier series in companion with adaptive observer system. A general-purpose program for solving the problems with arbitrary number, sizes and various locations of circular cylinders was developed. Therefore, not only the sound scattering problems from a point source but also electromagnetic scattering problems can be solved by using the present approach. Good agreement is observed after comparing with theoretical and experiment data.

In the chapter 3, not only a new approach was employed to investigate the water-wave interaction with arrays of surface-piercing porous cylinders, but also the effect of porous parameter and disorder on the force in case of near-trapped modes was also examined. Impermeable cylinder case can be treated as a special case of zero parameter. Numerical results including the free-surface elevation and resultant forces on each cylinder have been presented to illustrate the effect of porous and disorder parameter on the force in case of trapped modes. It is found that the disorder is more sensitive to suppress the occurrence of near-trapped modes than the porosity.

Finally, some conclusions are made and the further researches are indicated in chapter 4. The frame of the thesis is shown in Figure 1-5.

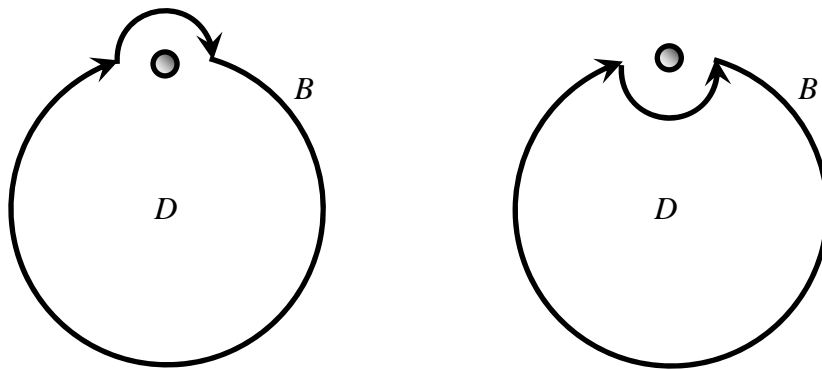


Figure 1-1 (a) Bump contour

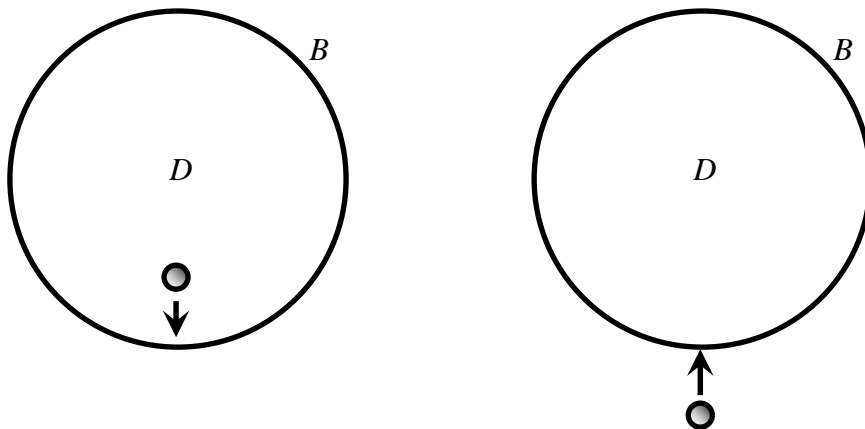


Figure 1-1 (b) Limiting contour

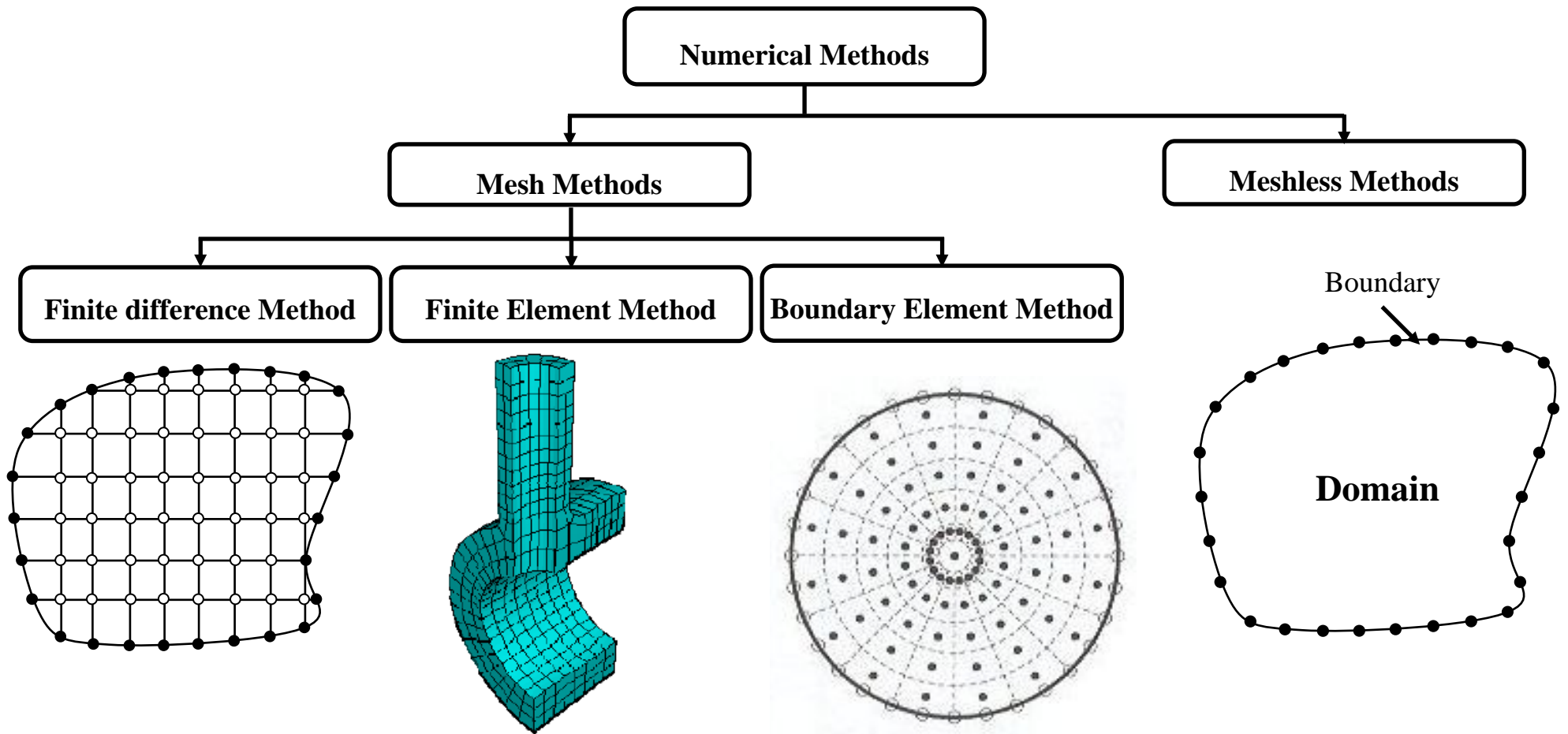


Figure 1-2 Mesh generation

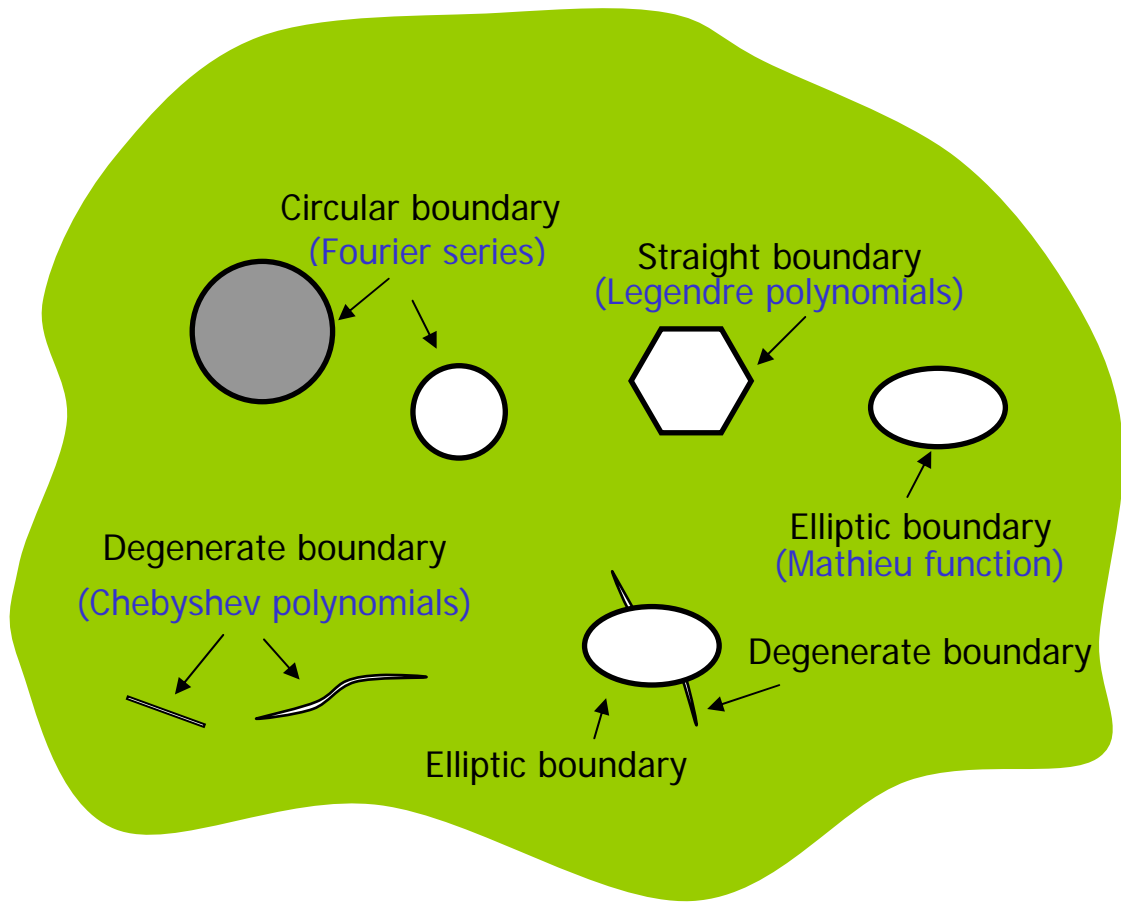


Figure 1-3 Boundary value problems with arbitrary boundaries

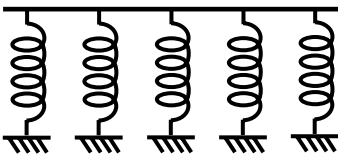
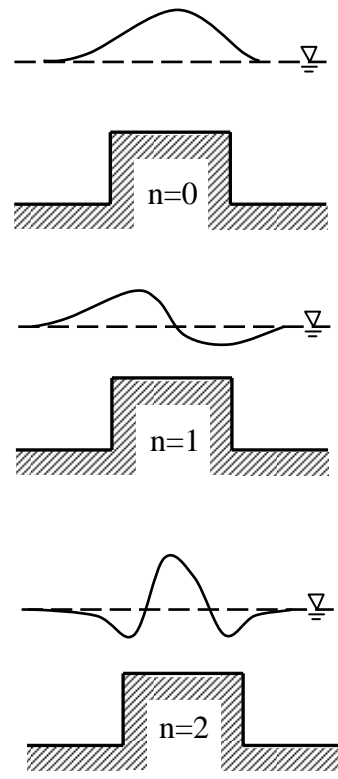
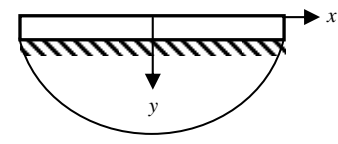
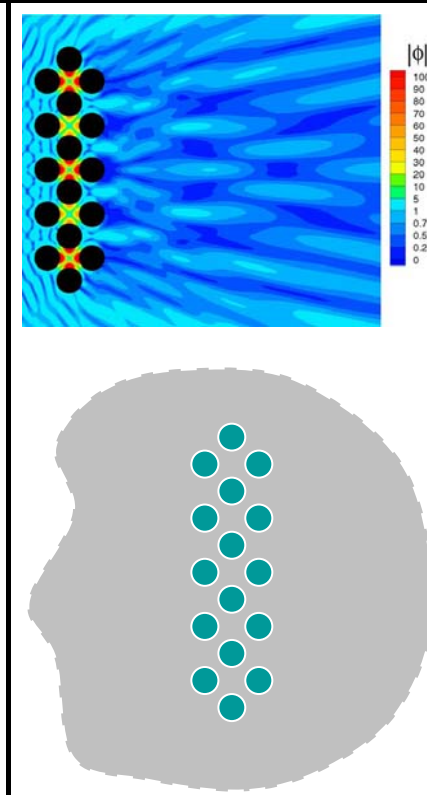
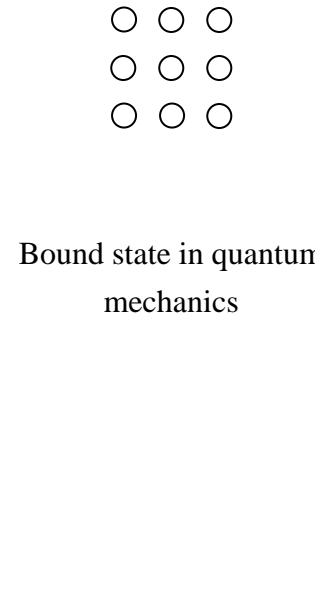
Engineering and physics in the trapped mode				
String vibration	Hydraulic engineering	Earthquake engineering	Coastal engineering	Quantum physics
	 <p>Trapped modes on a ridge</p>	 <p>Love wave in a layer-elastic half-space</p>	 <p>Near-trapped mode in water wave</p>	 <p>Bound state in quantum mechanics</p>

Figure 1-4 Near-trapped modes in physics and engineering

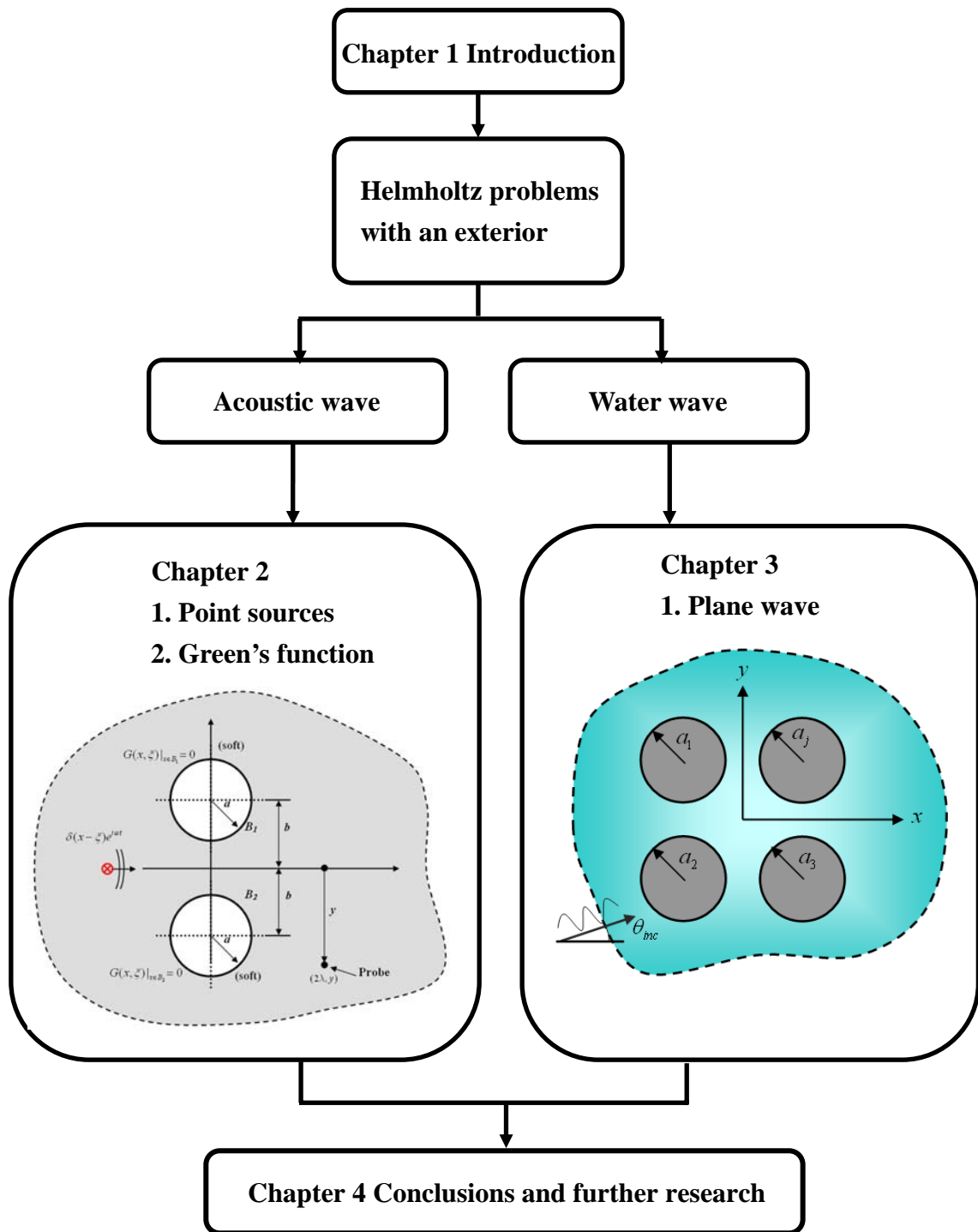


Figure 1-5 The frame of the thesis

Chapter 2 Scattering of sound from point sources by multiple circular cylinders using addition theorem and superposition technique

Summary

In this chapter, we employ the addition theorem and superposition technique to solve the scattering problem with multiple circular cylinders arising from point sound sources. Using the superposition technique, the problem can be decomposed into two individual parts. One is the free-space fundamental solution. The other is a typical boundary value problem (BVP) with specified boundary conditions derived from the addition theorem by translating the fundamental solution. Following the success of null-field boundary integral formulation to solve the typical BVP of the Helmholtz equation with Fourier densities, the second-part solution is easily obtained after collocating the observation point exactly on the real boundary and matching the boundary condition. The total solution is obtained by superimposing the two parts which are the fundamental solution and the semi-analytical solution of the Helmholtz problem. An example was demonstrated to validate of the present approach. The parameter study of size and spacing between cylinders are addressed. The results are well compared with the available theoretical solutions and experimental data.

2.1 Introduction

Multiple scattering problems occur in many applications related to various areas of applied science, e.g. acoustics [45, 1], electromagnetism [29, 44], elasticity [42] and water-wave [35] problems. Mathematically speaking, the scattering field appears as the superposition of free field and radiation field. A better understanding of scattering phenomenon requires a precise knowledge of the influence of the different geometrical and physical parameters of the problem. Owing to the complexity of this problem, a numerical solution is always resorted, especially in the case where the number, radii and positions of objects are arbitrary. It can be consulted with the textbook of Martin [38].

Many researchers investigated the point-source problems in the past years. Row [43, 44] successfully measured the experimental data of the interaction between two circular cylinders within an infinite domain. When the point source is far away the scatter, the problem can be seen as a multiple scattering problem subject to the plane wave. Sherer [45] developed an analytical method for solving the scattering problem with multiple rigid circular cylinders arranged in an arbitrary configuration. He used the Hankel transform method to calculate the incident field and determined the scattering fields from each cylinder in the collection through the separation of variables. The scattering problem from an array of circular cylinders with oblique incidence plane wave is investigated by Henin *et al.* [29]. Not only TM but also TE incident plane waves were considered. Interaction between two penetrable cylinders subject to the oblique incidence were studied by Yousif and Köhler [53]. Some special cases of normal incidence, small radii, perfectly conducting cylinders and a single cylinder are also considered.

Recently, Chen and his group developed the null-field integral equation in conjunction with the degenerate kernel to solve many engineering problems [8, 9, 10, 17]. They claimed that their approaches is one kind of semi-analytical approach since the error comes from truncating the terms of Fourier series. However, the ill-conditioned problem is arisen when the null-field integral equations are used. That is why people prefer collocation on boundary even though there are some singularity issues to solve. Nonsingular formulation of the Trefftz method was studied by Li *et al.* [31]. If the BEM is employed, Cauchy principal value or finite part concept is required to calculate the singular or hypersingular integrals [50]. An idea using the null-field integral formulation but collocating on the real boundary without singularity is proposed by Chen and his coworkers [8, 9, 10, 17]. Five advantages, mesh-free generation, well-posed model, free of calculating principal value, elimination of boundary-layer effect and exponential convergence, are obtained. They also extended their approach to derive the anti-plane dynamic Green's function [14]. Not only perfect but also imperfect interface problems were addressed. Chen *et al.* [12] also have proposed an logical approach to construct the Green's function of Laplace operator by using the addition theorem and the

superposition technique.

In this chapter, the addition theorem and superposition technique are employed to solve the scattering problem with multiple circular cylinders arising from point sound sources. The problem is decomposed into two parts. One is the problem of the fundamental solution for the free field. The other is a typical BVP with specified boundary conditions derived from the addition theorem by translating the fundamental solution. Following the success of null-field boundary integral formulation in conjunction with degenerate kernel to solve the typical BVP, the second part solution can be easily obtained after collocating the observation point exactly on the real boundary and matching boundary condition. The total solution is obtained by superimposing the two parts. An example was demonstrated to validate the proposed approach. The parameters of size and spacing of cylinders are considered. The results are compared well with the available theoretical solutions and experimental data.

2.2 Null-field integral formulation for a typical BVP

2.2.1 Problem statements for BVP without sources

A typical BVP with H randomly distributed circular cylinders bounded in an infinite domain enclosed with the boundaries, B_j ($j = 1, 2, \dots, H$),

$$B = \bigcup_{j=1}^H B_j, \quad (2-1)$$

is considered here. The field $u(x)$ satisfies

$$(\nabla^2 + k^2)u(\mathbf{x}) = 0, \quad \mathbf{x} \in D, \quad (2-2)$$

where D is the domain, ∇^2 is the Laplacian operator, k is the wave number which is the angular frequency over the speed of sound. The boundary condition can be specified to either Dirichlet or Neumann type as follows:

$$u(\mathbf{x}) = u, \quad \mathbf{x} \in B, \quad (2-3)$$

$$\text{or } \frac{\partial u(\mathbf{x})}{\partial n_x} = t, \quad \mathbf{x} \in B. \quad (2-4)$$

This problem is a typical BVP, and can be easily solved by using the null-field integral approach.

2.2.2 Dual null-field integral formulation- the conventional version

Based on the dual boundary integral formulations [8] for the domain point, we have

$$2\pi u(\mathbf{x}) = \int_B T(\mathbf{s}, \mathbf{x})u(\mathbf{s})dB(\mathbf{s}) - \int_B U(\mathbf{s}, \mathbf{x})t(\mathbf{s})dB(\mathbf{s}), \quad \mathbf{x} \in D, \quad (2-5)$$

$$2\pi t(\mathbf{x}) = \int_B M(\mathbf{s}, \mathbf{x})u(\mathbf{s})dB(\mathbf{s}) - \int_B L(\mathbf{s}, \mathbf{x})t(\mathbf{s})dB(\mathbf{s}), \quad \mathbf{x} \in D, \quad (2-6)$$

where \mathbf{s} and \mathbf{x} are the source and field points, respectively, $t(\mathbf{s}) = \partial u(\mathbf{s})/\partial n_s$, B is the boundary, n_s and n_x denote the outward normal vectors at the source point \mathbf{s} and field point \mathbf{x} , respectively. The kernel function $U(\mathbf{s}, \mathbf{x})$ is the fundamental solution which satisfies

$$(\nabla^2 + k^2)U(\mathbf{s}, \mathbf{x}) = 2\pi\delta(\mathbf{x} - \mathbf{s}), \quad (2-7)$$

where $\delta(\mathbf{x} - \mathbf{s})$ denotes the Dirac-delta function. The other kernel functions can be obtained as

$$T(\mathbf{s}, \mathbf{x}) = \frac{\partial U(\mathbf{s}, \mathbf{x})}{\partial n_s}, \quad (2-8)$$

$$L(\mathbf{s}, \mathbf{x}) = \frac{\partial U(\mathbf{s}, \mathbf{x})}{\partial n_x}, \quad (2-9)$$

$$M(\mathbf{s}, \mathbf{x}) = \frac{\partial^2 U(\mathbf{s}, \mathbf{x})}{\partial n_s \partial n_x}. \quad (2-10)$$

By moving the field point \mathbf{x} to the boundary, the dual boundary integral equations can be obtained as follows:

$$\pi u(\mathbf{x}) = C.P.V. \int_B T(\mathbf{s}, \mathbf{x})u(\mathbf{s})dB(\mathbf{s}) - R.P.V. \int_B U(\mathbf{s}, \mathbf{x})t(\mathbf{s})dB(\mathbf{s}), \quad \mathbf{x} \in B, \quad (2-11)$$

$$\pi t(\mathbf{x}) = H.P.V. \int_B M(\mathbf{s}, \mathbf{x})u(\mathbf{s})dB(\mathbf{s}) - C.P.V. \int_B L(\mathbf{s}, \mathbf{x})t(\mathbf{s})dB(\mathbf{s}), \quad \mathbf{x} \in B, \quad (2-12)$$

where *R.P.V.* is the Riemann principal value, *C.P.V.* is the Cauchy principal value and *H.P.V.* is the Hadamard (or called Mangler) principal value. By moving the field point to the complementary domain, the dual null-field integral equations are shown as:

$$0 = \int_B T(\mathbf{s}, \mathbf{x})u(\mathbf{s})dB(\mathbf{s}) - \int_B U(\mathbf{s}, \mathbf{x})t(\mathbf{s})dB(\mathbf{s}), \quad \mathbf{x} \in D^c, \quad (2-13)$$

$$0 = \int_B M(\mathbf{s}, \mathbf{x})u(\mathbf{s})dB(\mathbf{s}) - \int_B L(\mathbf{s}, \mathbf{x})t(\mathbf{s})dB(\mathbf{s}), \quad \mathbf{x} \in D^c, \quad (2-14)$$

where “ D^c ” denotes the complementary domain.

2.2.3 Dual null-field integral formulations- the present version

By introducing the degenerate kernel, the collocation points can be exactly located on the real boundary free of calculating singular integrals in the sense of principal value. Therefore, the integral equations for the domain point and null-field integral equations

in the interior problem are represented as

$$2\pi u(\mathbf{x}) = \int_B T^I(\mathbf{s}, \mathbf{x})u(\mathbf{s})dB(\mathbf{s}) - \int_B U^I(\mathbf{s}, \mathbf{x})t(\mathbf{s})dB(\mathbf{s}), \quad \mathbf{x} \in D \cup B, \quad (2-15)$$

$$2\pi t(\mathbf{x}) = \int_B M^I(\mathbf{s}, \mathbf{x})u(\mathbf{s})dB(\mathbf{s}) - \int_B L^I(\mathbf{s}, \mathbf{x})t(\mathbf{s})dB(\mathbf{s}), \quad \mathbf{x} \in D \cup B, \quad (2-16)$$

and

$$0 = \int_B T^E(\mathbf{s}, \mathbf{x})u(\mathbf{s})dB(\mathbf{s}) - \int_B U^E(\mathbf{s}, \mathbf{x})t(\mathbf{s})dB(\mathbf{s}), \quad \mathbf{x} \in D^c \cup B, \quad (2-17)$$

$$0 = \int_B M^E(\mathbf{s}, \mathbf{x})u(\mathbf{s})dB(\mathbf{s}) - \int_B L^E(\mathbf{s}, \mathbf{x})t(\mathbf{s})dB(\mathbf{s}), \quad \mathbf{x} \in D^c \cup B. \quad (2-18)$$

For the exterior problem, the domain of interest is in the external region of the circular boundary and the complementary domain is in the internal region of the circle.

Therefore, the null-field integral equations are represented as

$$2\pi u(\mathbf{x}) = \int_B T^E(\mathbf{s}, \mathbf{x})u(\mathbf{s})dB(\mathbf{s}) - \int_B U^E(\mathbf{s}, \mathbf{x})t(\mathbf{s})dB(\mathbf{s}), \quad \mathbf{x} \in D \cup B, \quad (2-19)$$

$$2\pi t(\mathbf{x}) = \int_B M^E(\mathbf{s}, \mathbf{x})u(\mathbf{s})dB(\mathbf{s}) - \int_B L^E(\mathbf{s}, \mathbf{x})t(\mathbf{s})dB(\mathbf{s}), \quad \mathbf{x} \in D \cup B, \quad (2-20)$$

and

$$0 = \int_B T^I(\mathbf{s}, \mathbf{x})u(\mathbf{s})dB(\mathbf{s}) - \int_B U^I(\mathbf{s}, \mathbf{x})t(\mathbf{s})dB(\mathbf{s}), \quad \mathbf{x} \in D^c \cup B, \quad (2-21)$$

$$0 = \int_B M^I(\mathbf{s}, \mathbf{x})u(\mathbf{s})dB(\mathbf{s}) - \int_B L^I(\mathbf{s}, \mathbf{x})t(\mathbf{s})dB(\mathbf{s}), \quad \mathbf{x} \in D^c \cup B. \quad (2-22)$$

where the superscripts of “ T ” and “ E ” are selected interior and exterior degenerate kernels for fundamental solutions. The explicit forms of degenerate kernels will be elaborated on later.

2.2.4 Expansions of the fundamental solution and boundary density

The closed-form fundamental solution as previously mentioned is

$$U(\mathbf{s}, \mathbf{x}) = \frac{-i\pi H_0^{(1)}(kr)}{2}, \quad (2-23)$$

where $r \equiv |\mathbf{s} - \mathbf{x}|$ is the distance between the source point and the field point, $H_0^{(1)}$ is the first kind Hankel function of zeroth order, and i is the imaginary number ($i^2 = -1$). To fully utilize the property of circular geometry, the mathematical tools, degenerate (separable or finite rank) kernel and Fourier series, are adopted for analytical calculation of boundary integrals.

2.2.4.1 Degenerate (separable) kernel for fundamental solution

In the polar coordinates, the field point \mathbf{x} and source point \mathbf{s} can be expressed

as (ρ, ϕ) and (R, θ) , respectively. By employing the addition theorem for separating the source point and field point, kernel functions, $U(\mathbf{s}, \mathbf{x})$, $T(\mathbf{s}, \mathbf{x})$, $L(\mathbf{s}, \mathbf{x})$ and $M(\mathbf{s}, \mathbf{x})$, are expanded in terms of degenerate kernel as shown below:

$$U(\mathbf{s}, \mathbf{x}) = \begin{cases} U^I(\mathbf{s}, \mathbf{x}) = \frac{-i\pi}{2} \sum_{m=0}^{\infty} \varepsilon_m J_m(k\rho) H_m^{(1)}(kR) \cos[m(\theta - \phi)], & R \geq \rho, \\ U^E(\mathbf{s}, \mathbf{x}) = \frac{-i\pi}{2} \sum_{m=0}^{\infty} \varepsilon_m J_m(kR) H_m^{(1)}(k\rho) \cos[m(\theta - \phi)], & R < \rho, \end{cases} \quad (2-24)$$

$$T(\mathbf{s}, \mathbf{x}) = \begin{cases} T^I(\mathbf{s}, \mathbf{x}) = \frac{-\pi ki}{2} \sum_{m=0}^{\infty} \varepsilon_m J_m(k\rho) H_m^{(1)}(kR) \cos[m(\theta - \phi)], & R > \rho, \\ T^E(\mathbf{s}, \mathbf{x}) = \frac{-\pi ki}{2} \sum_{m=0}^{\infty} \varepsilon_m J'_m(kR) H_m^{(1)}(k\rho) \cos[m(\theta - \phi)], & R < \rho, \end{cases} \quad (2-25)$$

$$L(\mathbf{s}, \mathbf{x}) = \begin{cases} L^I(\mathbf{s}, \mathbf{x}) = \frac{-\pi ki}{2} \sum_{m=0}^{\infty} \varepsilon_m J'_m(k\rho) H_m^{(1)}(kR) \cos[m(\theta - \phi)], & R > \rho, \\ L^E(\mathbf{s}, \mathbf{x}) = \frac{-\pi ki}{2} \sum_{m=0}^{\infty} \varepsilon_m J_m(kR) H_m^{(1)}(k\rho) \cos[m(\theta - \phi)], & R < \rho, \end{cases} \quad (2-26)$$

$$M(\mathbf{s}, \mathbf{x}) = \begin{cases} M^I(\mathbf{s}, \mathbf{x}) = \frac{-\pi k^2 i}{2} \sum_{m=0}^{\infty} \varepsilon_m J'_m(k\rho) H_m^{(1)}(kR) \cos[m(\theta - \phi)], & R \geq \rho, \\ M^E(\mathbf{s}, \mathbf{x}) = \frac{-\pi k^2 i}{2} \sum_{m=0}^{\infty} \varepsilon_m J'_m(kR) H_m^{(1)}(k\rho) \cos[m(\theta - \phi)], & R < \rho, \end{cases} \quad (2-27)$$

where superscripts “ T ” and “ E ” denote the interior and exterior cases for the expressions of kernel, respectively, and ε_m is the Neumann factor

$$\varepsilon_m = \begin{cases} 1, & m = 0, \\ 2, & m = 1, 2, \dots, \infty. \end{cases} \quad (2-28)$$

Mathematically speaking, the expressions of fundamental solution in Eqs. (2-24)-(2-27) are termed degenerate kernels (or separable kernels) which can expand the kernel to sums of products of function of the field point \mathbf{x} alone and functions of the source point \mathbf{s} alone. If the finite sum of series is considered, the kernel is finite rank. As we shall see in the later sections, the theory of boundary integral equations with degenerate kernel is nothing more than the linear algebra. Since the potentials resulted from $T(\mathbf{s}, \mathbf{x})$ and $L(\mathbf{s}, \mathbf{x})$ are discontinuous across the boundary, the potentials of $T(\mathbf{s}, \mathbf{x})$ and $L(\mathbf{s}, \mathbf{x})$ for $R \rightarrow \rho^+$ and $R \rightarrow \rho^-$ are different. This is the reason why $R = \rho$ is not included in the expression for the degenerate kernels of $T(\mathbf{s}, \mathbf{x})$ and $L(\mathbf{s}, \mathbf{x})$ in Eqs. (2-25) and (2-26). The degenerate kernels simply serve as the means to evaluate regular integrals analytically and take the limits analytically. The reason is that integral equation for the domain point of Eq. (2-15) and the null-field integral equation of Eq. (2-17) yield the same algebraic

equation when the limit is taken from the inside or from the outside of the region. Both limits represent the same algebraic equation that is an approximate counterpart of the boundary integral equation, that for the case of a smooth boundary has in the left-hand side term $\pi u(\mathbf{x})$ or $\pi t(\mathbf{x})$ rather than $2\pi u(\mathbf{x})$ or $2\pi t(\mathbf{x})$ for the domain point or 0 for the point outside the domain. Besides, the limiting case to the boundary is also addressed. The continuous and jump behavior across the boundary is well captured by the Wronskian property of Bessel function J_m and Y_m bases

$$W(J_m(kR), Y_m(kR)) = Y'_m(kR)J_m(kR) - Y_m(kR)J'_m(kR) = \frac{2}{\pi kR} \quad (2-29)$$

as shown below

$$\int_0^{2\pi} (T^I(\mathbf{s}, \mathbf{x}) - T^E(\mathbf{s}, \mathbf{x})) \cos(m\theta) R d\theta = 2\pi \cos(m\phi), \quad \mathbf{x} \in B, \quad (2-30)$$

$$\int_0^{2\pi} (T^I(\mathbf{s}, \mathbf{x}) - T^E(\mathbf{s}, \mathbf{x})) \sin(m\theta) R d\theta = 2\pi \sin(m\phi), \quad \mathbf{x} \in B. \quad (2-31)$$

After employing Eqs. (2-30)-(2-31), Eq. (2-19) and Eq. (2-21) yield the same linear algebraic equation when \mathbf{x} is exactly located the boundary from the domain or the complementary domain. A proof for the Laplace case done found by Chen *et al.* [8].

2.2.4.2 Fourier series expansion for boundary densities

We apply the Fourier series expansion to approximate the boundary density and its normal derivative as expressed by

$$u(s) = a_0 + \sum_{n=1}^{\infty} (a_n \cos n\theta + b_n \sin n\theta), \quad s \in B, \quad (2-32)$$

$$t(s) = p_0 + \sum_{n=1}^{\infty} (p_n \cos n\theta + q_n \sin n\theta), \quad s \in B, \quad (2-33)$$

where a_n, b_n, p_n and q_n ($n=0,1,2,\dots$) are the Fourier coefficients and θ is the polar angle. In the real computation, the integrals can be analytically calculated by employing the orthogonal property of Fourier series and only M terms is used in the summation instead of infinite terms. The present method is one kind of semi-analytical methods since errors only occur from to the truncation of Fourier series.

2.2.5 Adaptive observer system

In order to fully employ the property of degenerate kernels for circular boundaries, an adaptive observer system is addressed as shown in Figure 2-2. For the boundary integrals, the origin of the observer system can be adaptively located on the center of the

corresponding boundary contour. The dummy variable in the circular boundary integration is the angle instead of radial coordinate R . By using the adaptive system, all the integrals can be easily calculated for multiply-connected problems.

2.2.6 Linear algebraic equation

In order to calculate the Fourier coefficients, N ($N=2M+1$) boundary nodes for each circular boundary are located uniformly on each circular boundary. From Eqs. (2-17) and (2-18) or Eqs. (2-21) and (2-22), we have

$$0 = \sum_{i=1}^H \int_{B_i} T(\mathbf{s}, \mathbf{x}) u(\mathbf{s}) dB(\mathbf{s}) - \sum_{i=1}^H \int_{B_i} U(\mathbf{s}, \mathbf{x}) t(\mathbf{s}) dB(\mathbf{s}), \quad x \in D^c \cup B, \quad (2-34)$$

$$0 = \sum_{i=1}^H \int_{B_i} M(\mathbf{s}, \mathbf{x}) u(\mathbf{s}) dB(\mathbf{s}) - \sum_{i=1}^H \int_{B_i} L(\mathbf{s}, \mathbf{x}) t(\mathbf{s}) dB(\mathbf{s}), \quad x \in D^c \cup B. \quad (2-35)$$

It is noted that the integration path is clockwise. For the integral of the circular boundary B_i , the kernels ($U(\mathbf{s}, \mathbf{x})$, $T(\mathbf{s}, \mathbf{x})$, $L(\mathbf{s}, \mathbf{x})$ and $M(\mathbf{s}, \mathbf{x})$) are expressed by using the degenerate kernels and setting the origin at the center of B_i . The boundary densities ($u(\mathbf{s})$ and $t(\mathbf{s})$) are substituted by using the Fourier series. After discretizing Eq. (2-34), a linear algebraic system yields

$$[U]\{t\} = [T]\{u\}, \quad (2-36)$$

where $[U]$ and $[T]$ are the influence matrices with a dimension of $N \times (2M+1)$ by $N \times (2M+1)$, $\{u\}$ and $\{t\}$ denote the column vectors of Fourier coefficients with a dimension of $N \times (2M+1)$ by 1 for $\{u\}$ and $\{t\}$, respectively. All the unknown coefficients can be solved by using the linear algebraic equation. Then the unknown boundary data can be determined and the potential is obtained by substituting the boundary data into Eq. (2-15) or Eq. (2-19). Based on the null-field integral equation approach, successful applications to Laplace [15], Helmholtz [17], biharmonic [13] and biHelmholtz [32] problems have been done.

2.3 Methods of solution

2.3.1 Problem statements

The problem which we would like to study is the scattering problem with multiple cylinders arising from a point source as shown in Figure 2-3. The problem is governed by the Helmholtz operator as follows:

$$(\nabla^2 + k^2)G(\mathbf{x}, \xi) = 2\pi\delta(\mathbf{x} - \xi), \quad x \in D, \quad (2-37)$$

and the domain is bounded by

$$B = \bigcup_{j=1}^H B_j. \quad (2-38)$$

Here, the cylinders are specified to soft boundaries as

$$G(\mathbf{x}, \xi) = 0, \quad x \in B. \quad (2-39)$$

The purposed approach for solving the problem will be elaborated on the next section.

2.3.2 Green's function using the addition theorem and superposition technique

The scattering problem subject to a point sound source is shown in Figure 2-3. It can be decomposed into two parts, the fundamental solution (free field) and the radiation field, as shown in Figures 2-4(a) and 2-4(b). Based on the addition theorem, the fundamental solution can be separated into the series form using Eq. (2-24). For matching the boundary condition, the superposition of the artificial boundary condition ($G_f(\mathbf{x}, \xi)$) in Figure 2-4(a) and the radiation boundary condition ($G_r(\mathbf{x}, \xi)$) in Figures 2-4(b) must satisfy the original boundary condition in Figure 2-3. The second part (radiation field) is a typical BVP and can be easily solved by employing the null-field integral equation approach as mentioned in Section 2. For clarity, the flowchart of our method is shown in Figure 2-5.

2.3.3 Green's third-identity approach

Based on the Green's third identity, with respect to two systems u and v , we have

$$\int_D u(\mathbf{x})\nabla^2 v(\mathbf{x})dD(\mathbf{x}) = \int_B u(\mathbf{x})\frac{\partial v(\mathbf{x})}{\partial n}dB(\mathbf{x}) - \int_D \nabla u(\mathbf{x})\nabla v(\mathbf{x})dD(\mathbf{x}), \quad (2-40)$$

$$\begin{aligned} & \int_D [u(\mathbf{x})\nabla^2 v(\mathbf{x})dD(\mathbf{x}) - v(\mathbf{x})\nabla^2 u(\mathbf{x})dD(\mathbf{x})] \\ & = \int_B [u(\mathbf{x})\frac{\partial v(\mathbf{x})}{\partial n} - v(\mathbf{x})\frac{\partial u(\mathbf{x})}{\partial n}]dB(\mathbf{x}). \end{aligned} \quad (2-41)$$

By selecting the fundamental solution $U(\mathbf{x}, \mathbf{s})$ as u and the Green's function $G(\mathbf{s}, \xi)$ as v , the Green's third identity gives

$$\begin{aligned} 2\pi G(\mathbf{x}, \xi) & = \int_B T(\mathbf{s}, \mathbf{x})G(\mathbf{s}, \xi)dB(\mathbf{s}) - \int_B U(\mathbf{s}, \mathbf{x})\frac{\partial G(\mathbf{s}, \xi)}{\partial n_s}dB(\mathbf{s}) \\ & + U(\xi, \mathbf{x}), \quad x \in D. \end{aligned} \quad (2-42)$$

2.3.4 Equivalence between the solution using the Green's third identity and superposition technique

The boundary integral equation for the free field problem can be written as:

$$2\pi G_f(\mathbf{x}, \xi) = \int_B T(\mathbf{s}, \mathbf{x}) G_f(\mathbf{s}, \xi) dB(\mathbf{s}) - \int_B U(\mathbf{s}, \mathbf{x}) \frac{\partial G_f(\mathbf{s}, \xi)}{\partial n_s} dB(\mathbf{s}) + U(\xi, \mathbf{x}), \quad \mathbf{x} \in D, \quad (2-43)$$

where $G_f(\mathbf{x}, \xi)$ is the free field. The boundary integral equation for the typical boundary value problem can be written as

$$2\pi G_r(\mathbf{x}, \xi) = \int_B T(\mathbf{s}, \mathbf{x}) G_r(\mathbf{s}, \xi) dB(\mathbf{s}) - \int_B U(\mathbf{s}, \mathbf{x}) \frac{\partial G_r(\mathbf{s}, \xi)}{\partial n_s} dB(\mathbf{s}), \quad \mathbf{x} \in D. \quad (2-44)$$

where $G_r(\mathbf{x}, \xi)$ is the second part solution for the typical BVP. By superimposing G_f and G_r in Eqs. (2-43) and (2-44), respectively, we have

$$2\pi[G_f(\mathbf{s}, \xi) + G_r(\mathbf{s}, \xi)] = \int_B T(\mathbf{s}, \mathbf{x})[G_f(\mathbf{s}, \xi) + G_r(\mathbf{s}, \xi)] dB(\mathbf{s}) - \int_B U(\mathbf{s}, \mathbf{x}) \left[\frac{\partial G_f(\mathbf{s}, \xi)}{\partial n_s} + \frac{\partial G_r(\mathbf{s}, \xi)}{\partial n_s} \right] dB(\mathbf{s}) + U(\xi, \mathbf{x}), \quad \mathbf{x} \in D. \quad (2-45)$$

where $G_f(\mathbf{s}, \xi) + G_r(\mathbf{s}, \xi)$ and $\partial G_f(\mathbf{s}, \xi)/\partial n_s + \partial G_r(\mathbf{s}, \xi)/\partial n_s$ satisfy the original boundary conditions. By comparing Eq. (2-45) with Eq. (2-42), we can find $G(\mathbf{x}, \xi) = G_f(\mathbf{x}, \xi) + G_r(\mathbf{x}, \xi)$. Therefore, we have proven the mathematical equivalence between the solution of Green's third identity and that of superposition technique.

2.4 An illustrative example

We consider an infinite plane with two identical circular cylinders subject to a point sound source as shown in Figure 2-6. The radii of the two identical cylinders are a . The locations of source and probe are at $(-100, 0)$ and $(2\lambda, y)$, respectively, where λ is the wave length. The distance between the two centers of identical cylinders is $2b$. The boundary conditions are the Dirichlet types ($G(\mathbf{x}, \xi) = 0$) due to the soft cylinders. The potential distribution along the artificial boundary for the free field is shown in Figures 2-7 and 2-8 versus circular boundary and polar angle, respectively. Both the closed-form formula of Eq. (2-23) and series-form formula of Eq. (2-24) are given. After obtaining the total field at the probe, the relative amplitude is defined by dividing the total field with respect to the free field at $(x, 0)$. By considering $\lambda = \pi$, $b = 0.5\pi$ and $a = 0.05\pi$, the relative amplitude of the total field versus the probe location of y is shown in Figure 2-9. The results agree well with theoretical results and experimental data by Row [44].

The convergence rate is examined by using the Parseval's sum in Figures 2-10(a) and 2-10(b), for real and imaginary parts, respectively. It is found that only few terms for Fourier series are required. In the real calculation, twenty terms are adopted. By changing the size of cylinder (a) and the same parameters of $\lambda = \pi$ and $b = \pi/2$, the relative amplitudes are shown in Figures 2-11 and 2-12 for different sizes of cylinders $a = 0.2\lambda$ and $a = 0.318\lambda$, respectively. Agreement with Row's data is observed. By setting the fixed probe at $(2\lambda, 0)$, the relative amplitudes versus the space between the two cylinders for $a = 0.2\lambda$, 0.24λ , 0.318λ and 0.477λ are shown in Figures 2-13 ~ 2-16, respectively, to see the effect of distance between the two cylinders on various sizes of cylinders. All the results in Figures 2-13 ~ 2-16 agree well with the theoretical and experimental data by Row [44]. Although only two cylinders are used in this proposed approach, our approach can be extended to deal with multiple cylinders problems. In this example, efficiency of the proposed method of the sound scattering problem is verified.

In addition, it can be extended to deal with scattering problem in different engineering areas, e.g. water-wave problem or electromagnetism, by following the same concept.

An infinite plane with two circular holes

We extend to an infinite plane with two circular holes as shown in Figure 2-17. The source point is located at $\xi = (3.85, 0)$. The centers of the two holes are located at $(0, 0)$ and $(2.1, 0)$. The radii of a_1 and a_2 are 0.4 and 1.0, respectively. The distance between the two centers is $2b = 2.1$. Although we solve the Helmholtz equation, the Laplace solution can be obtained as a special case of a limiting wave number near zero. In real implementation, the wave number is chosen to be 10^{-6} . It is observed that computer fails if k is smaller than 10^{-6} . The numerical result by using the near-zero wave number in the Helmholtz program agree well with that of the Laplace case as shown in Figure 2-18. Besides, the data of the image method is also provided for comparison in Figure 2-19. Good agreement is obtained.

2.5 Conclusions

In this chapter, we proposed the addition theorem and superposition technique to solve the scattering problem of two identical cylinders subject to a point source. Regarding the BVP with circular boundaries, we have proposed a BIEM formulation by using degenerate kernels, null-field integral equation and Fourier series in companion with adaptive observer system. This method is a semi-analytical approach for the problems with circular boundaries since only truncation error in the Fourier series is involved. A general-purpose program for solving the problems with arbitrary number, sizes and various locations of circular cylinders was developed. Therefore, not only the sound scattering problems from a point source but also electromagnetic scattering problems can be solved by using the present approach. Good agreement is observed after comparing with theoretical and experiment data.

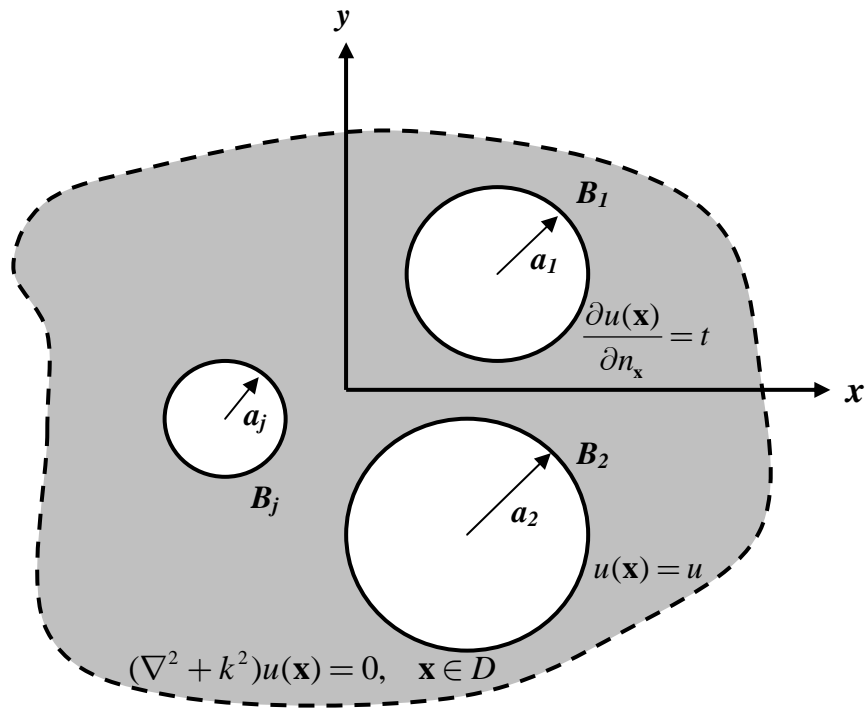


Figure 2-1 An infinite plane with arbitrary number of circular cylinders subject to the Dirichlet or Neumann boundary conditions

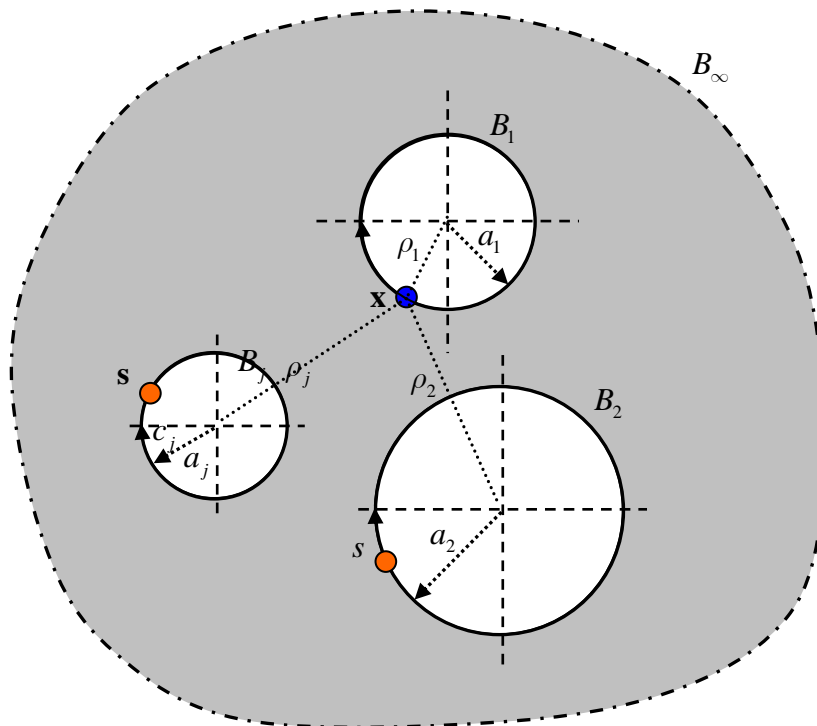


Figure 2-2 Sketch of the null-field integral equation in conjunction with the adaptive observer system

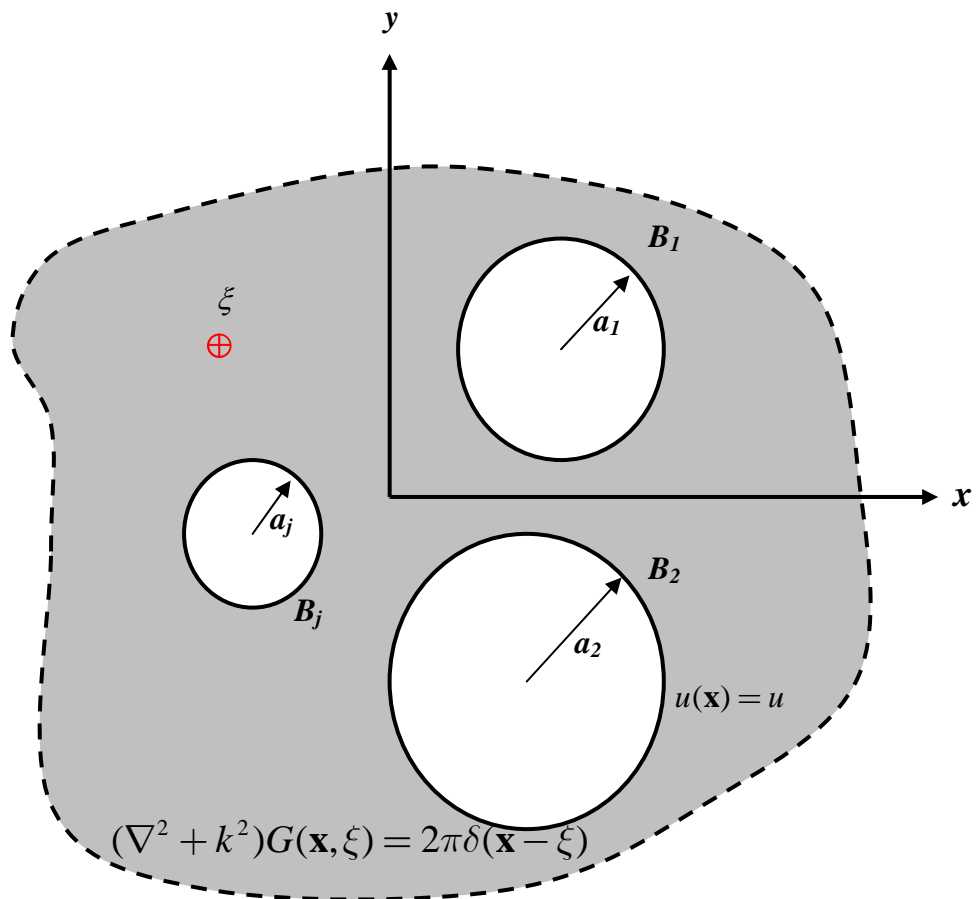


Figure 2-3 Infinite plane with arbitrary number of circular cylinders subject to a point sound source at ξ

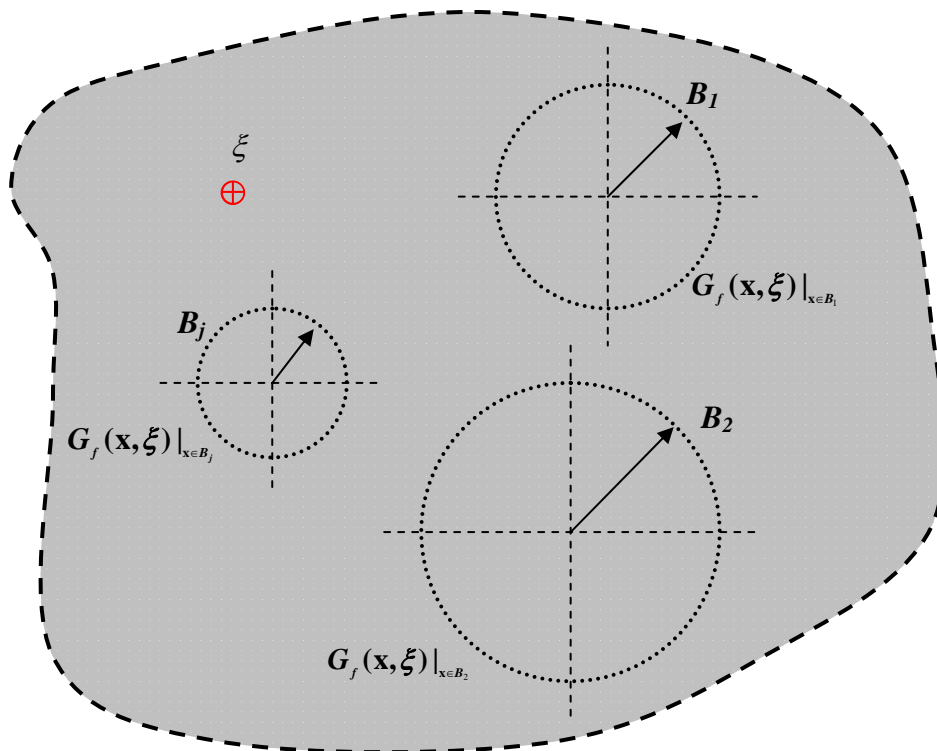


Figure 2-4(a) Free field of the fundamental solution

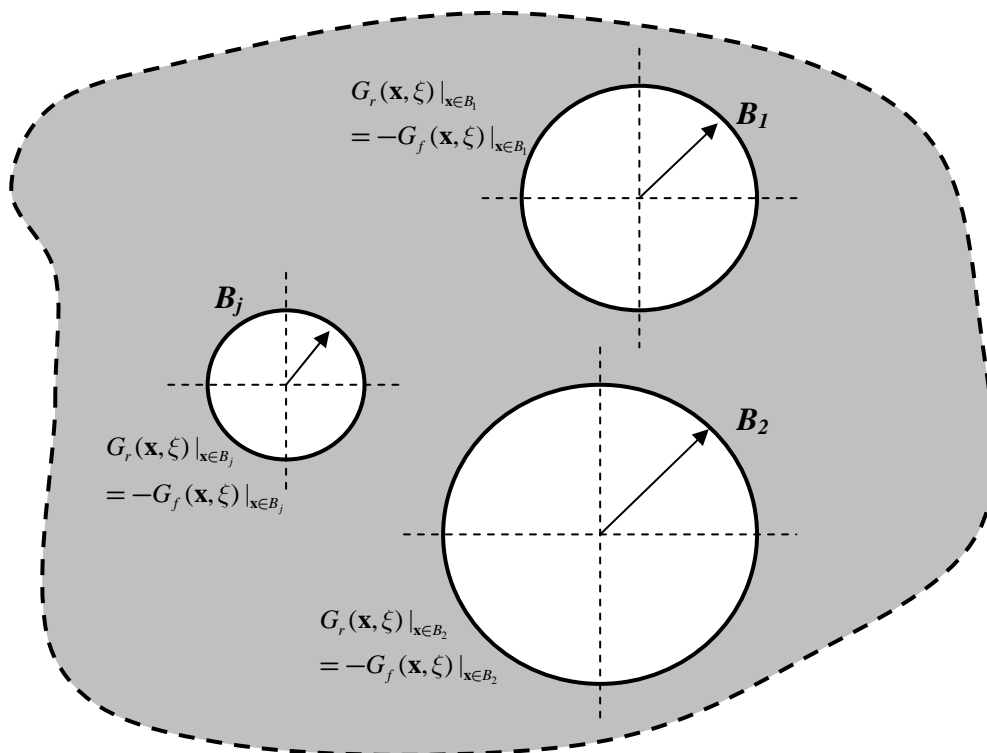


Figure 2-4(b) Radiation field (a typical BVP)

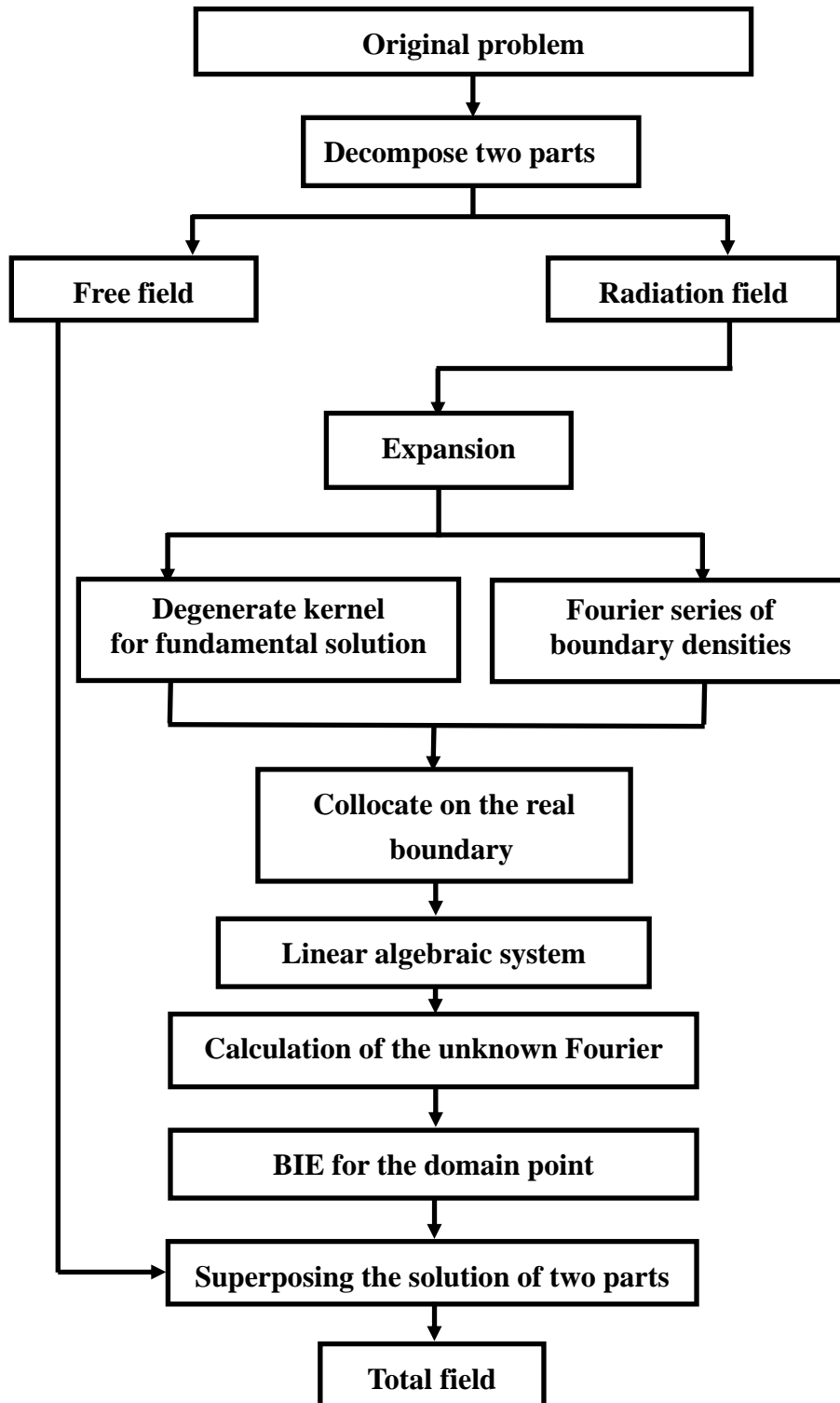


Figure 2-5 Flowchart of the present approach

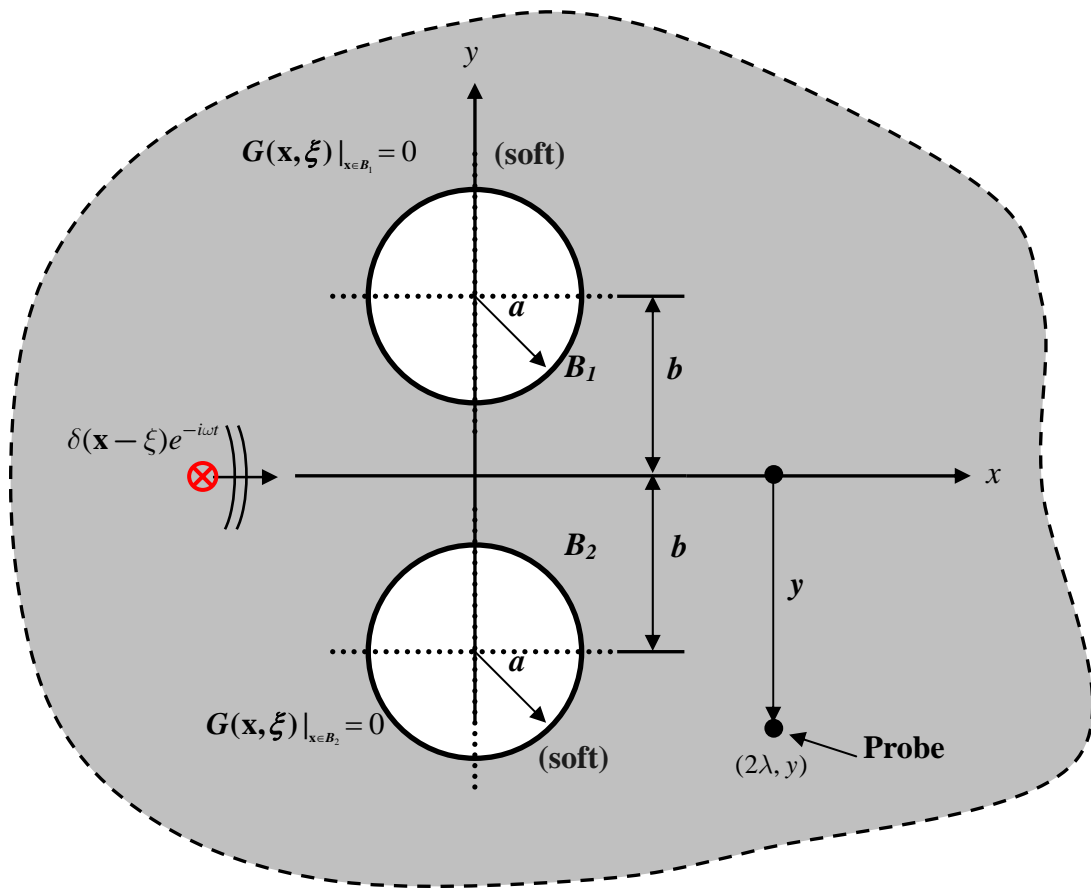


Figure 2-6 An infinite plane with two equal circular cylinders subject to a point sound source

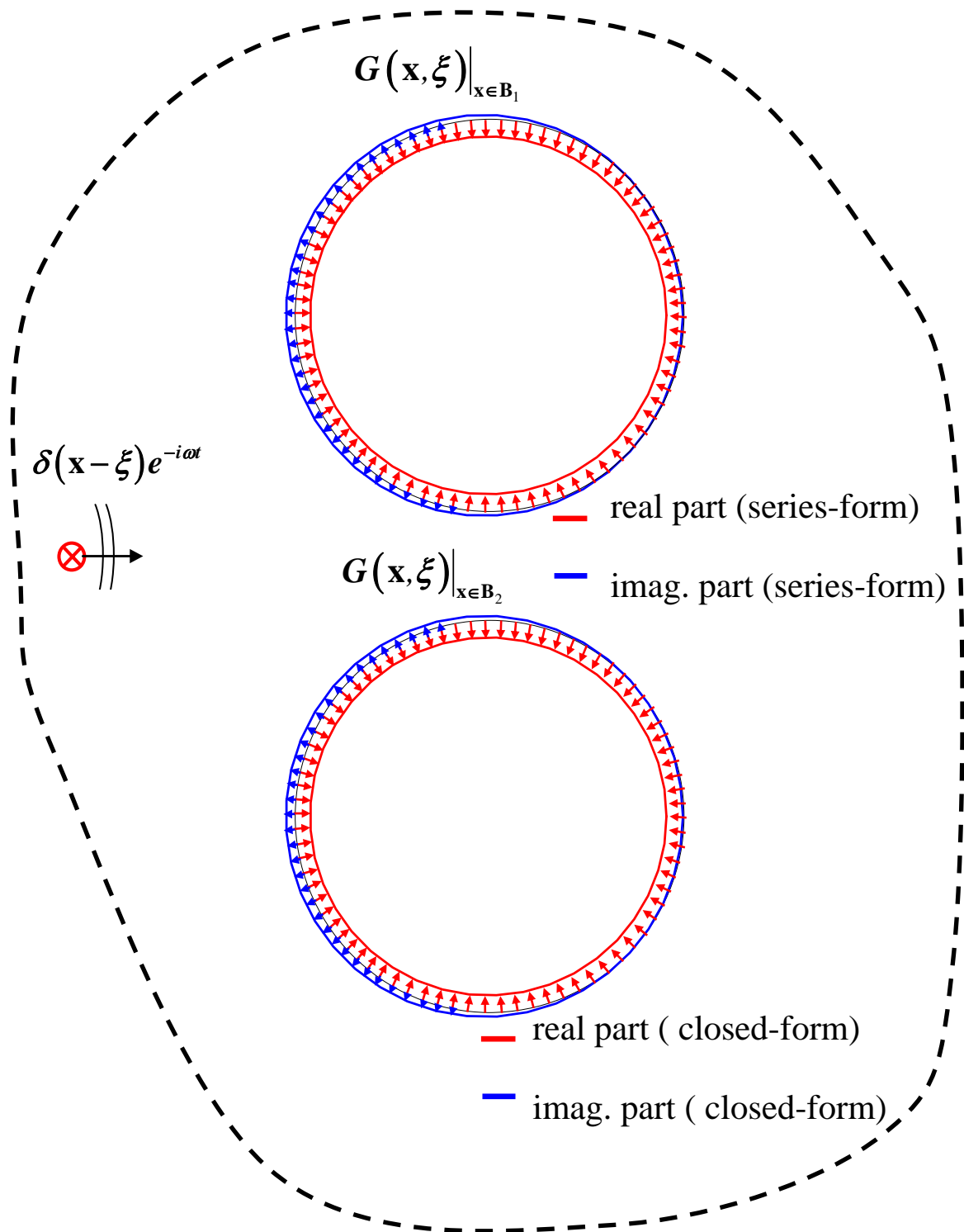


Figure 2-7 Distribution potential on the artificial boundaries in the free field (upper part: series-form, lower part: closed-form, $M=20$)

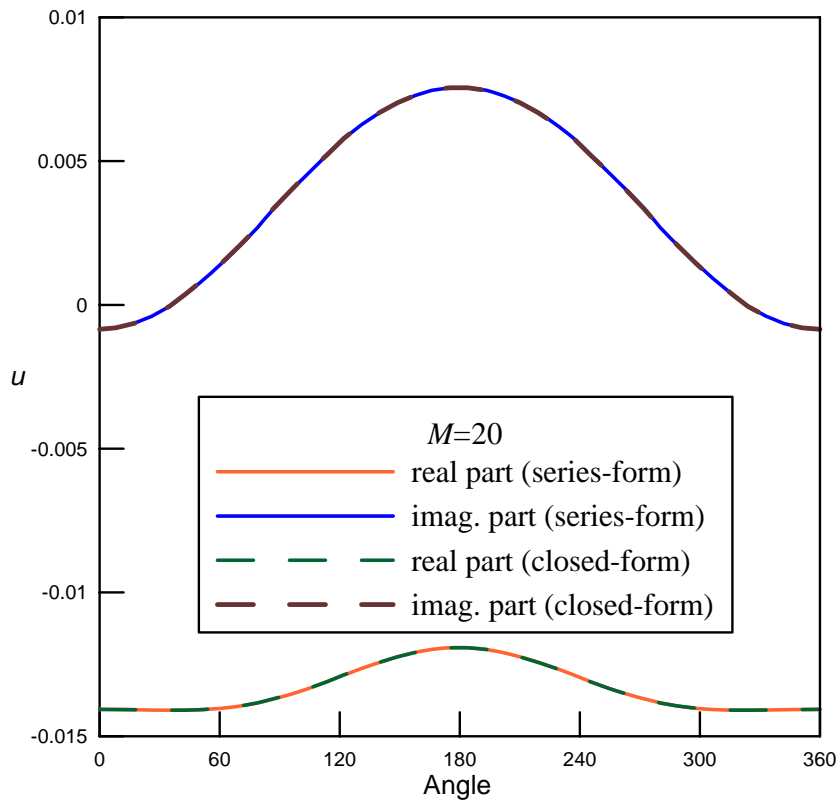


Figure 2-8 Distribution potential on the artificial boundaries in the free field versus polar angle

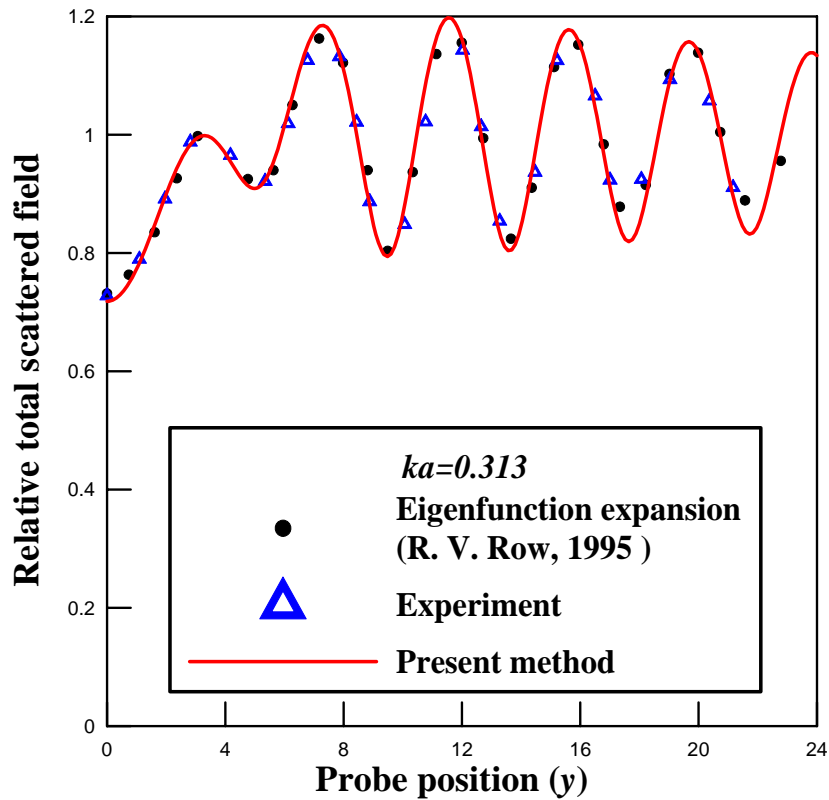


Figure 2-9 Relative amplitude of total field versus the probe location y ($M=20$)

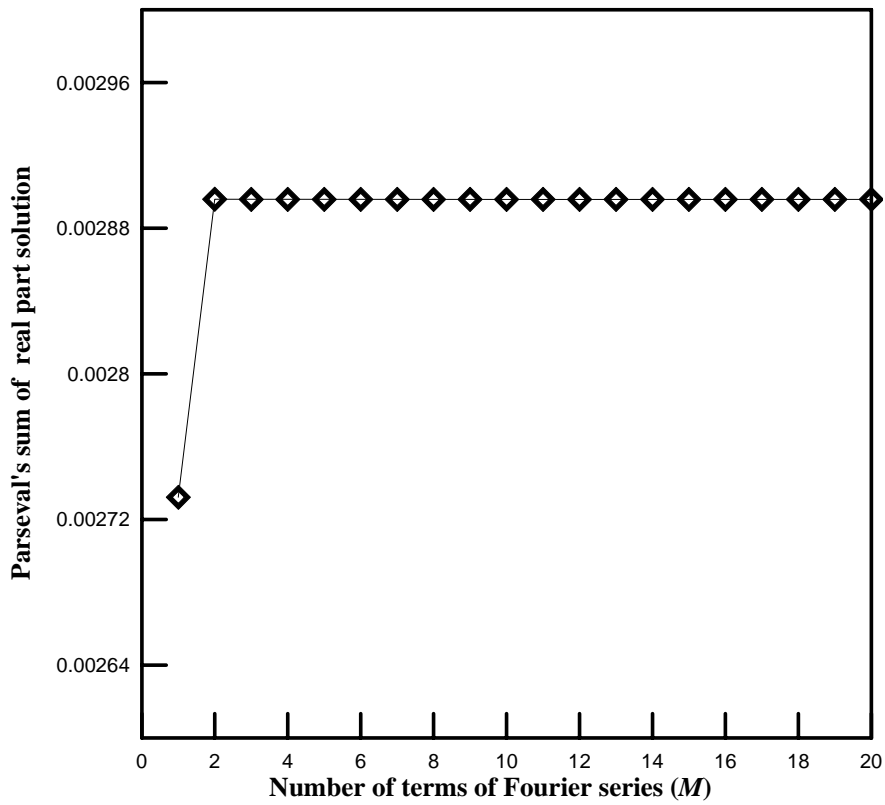


Figure 2-10(a) Convergence test of Parseval's sum for $\partial G(\mathbf{x}, \xi) / \partial n_x$ (real part)

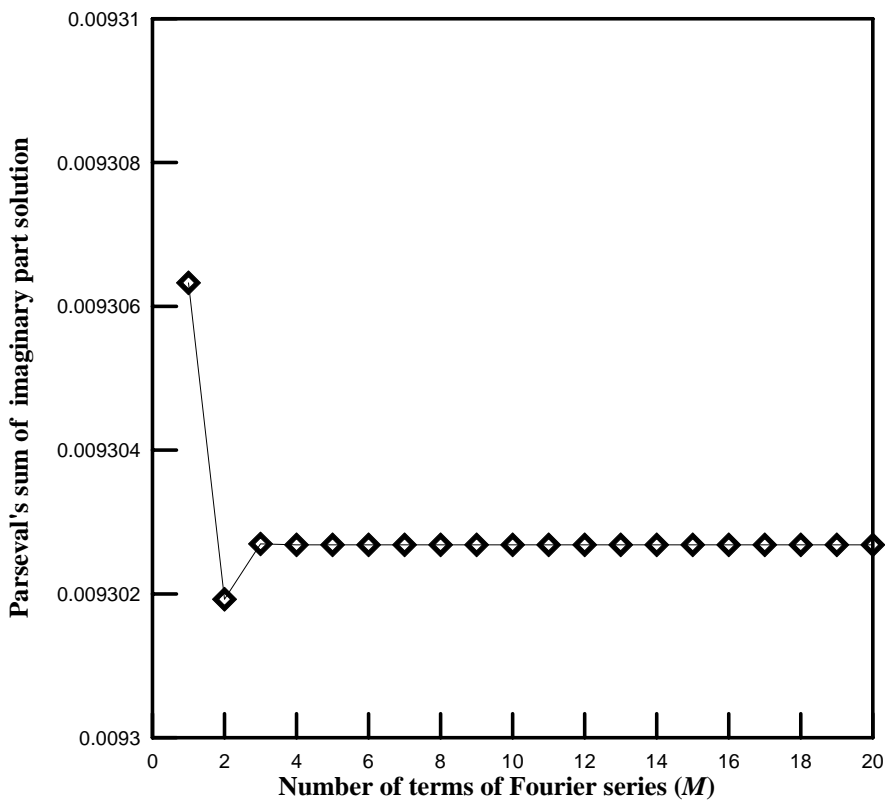


Figure 2-10(b) Convergence test of Parseval's sum for $\partial G(\mathbf{x}, \xi) / \partial n_x$ (imaginary part)

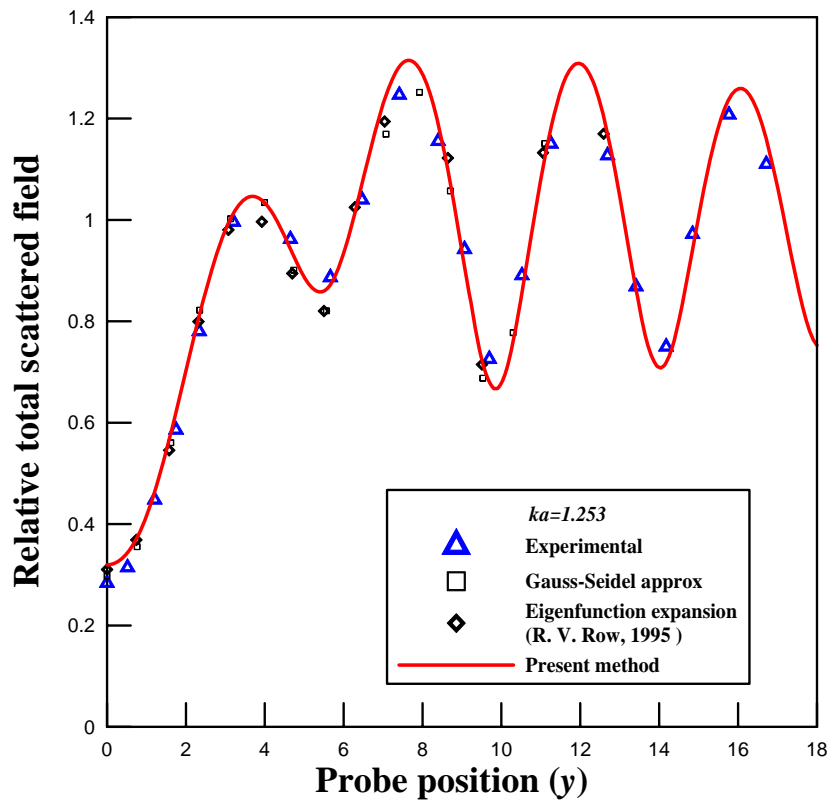


Figure 2-11 Relative amplitude of total field versus the probe location ($M=20$)

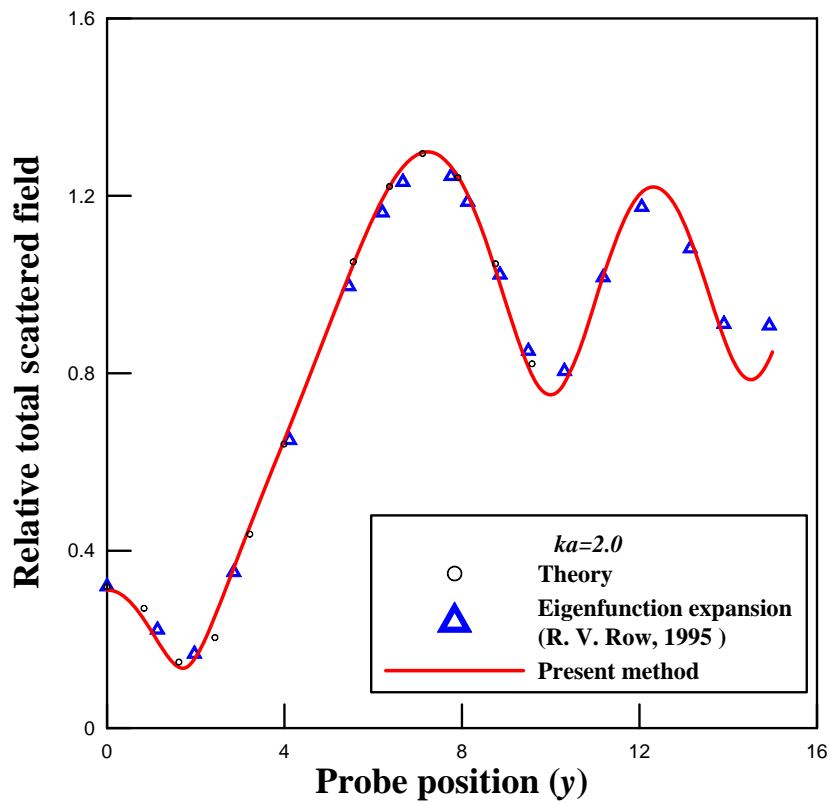


Figure 2-12 Relative amplitude of total field versus the probe location ($M=20$)

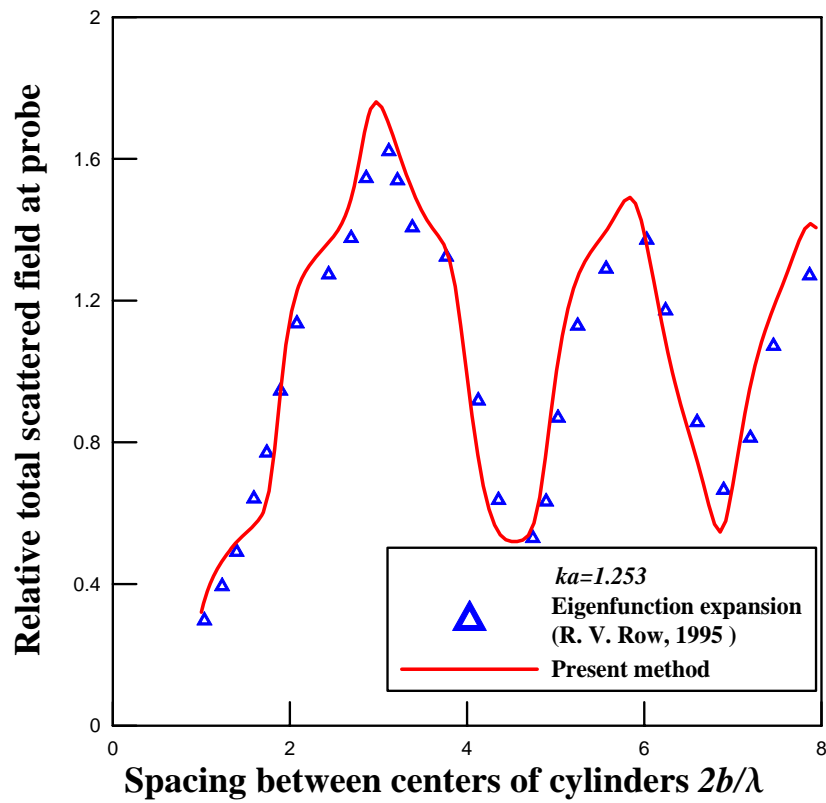


Figure 2-13 Relative amplitude of total field versus $2b/\lambda$ ($a = 0.2\lambda$ and $M = 20$)

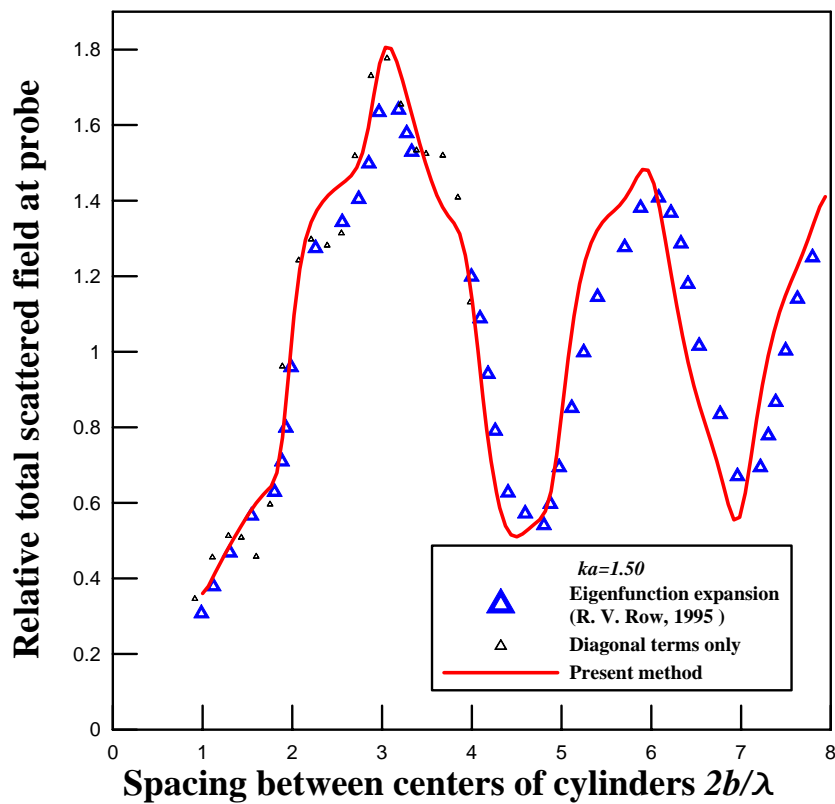


Figure 2-14 Relative amplitude of total field versus $2b/\lambda$ ($a = 0.24\lambda$ and $M = 20$)

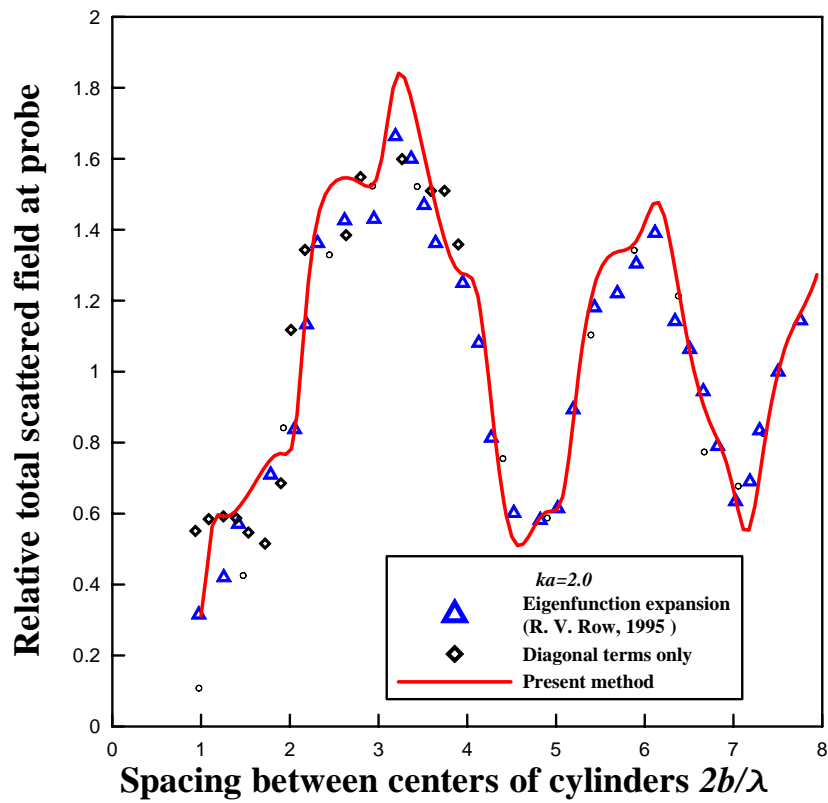


Figure 2-15 Relative amplitude of total field versus $2b/\lambda$ ($a = 0.318\lambda$ and $M = 20$)

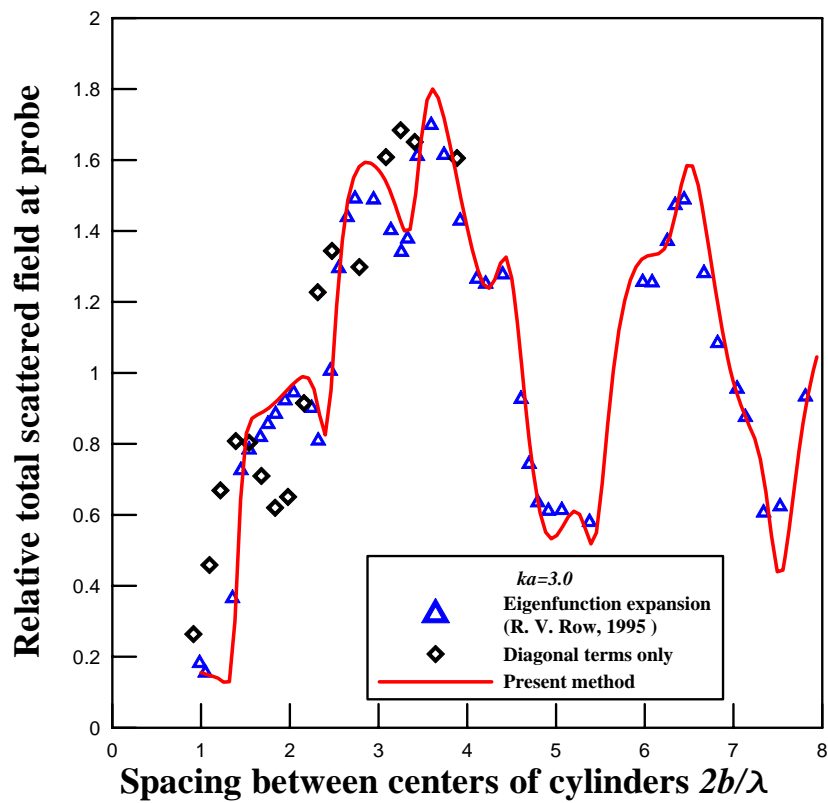


Figure 2-16 Relative amplitude of total field versus $2b/\lambda$ ($a = 0.477\lambda$ and $M = 20$)

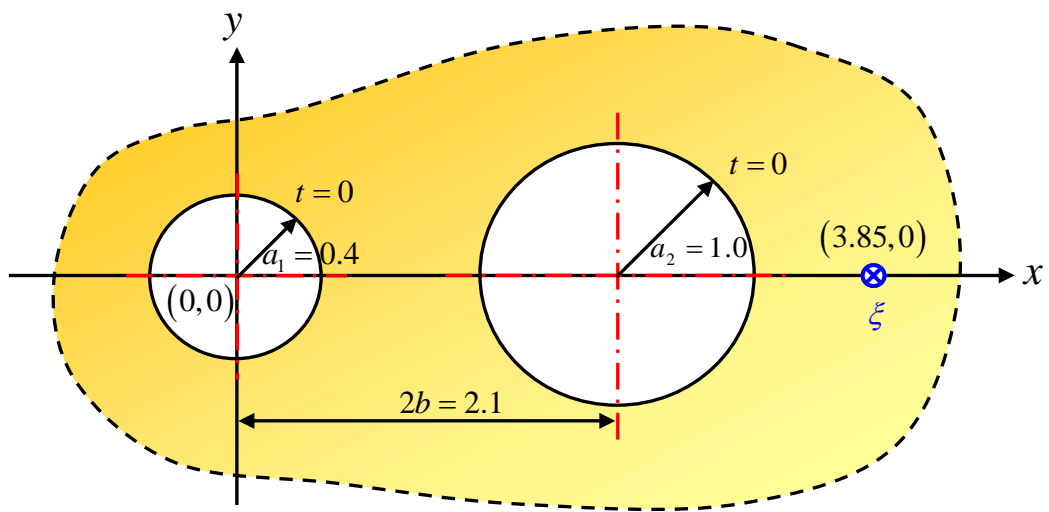


Figure 2-17 Infinite plane with two circular holes subject to the Neumann boundary condition under the source point

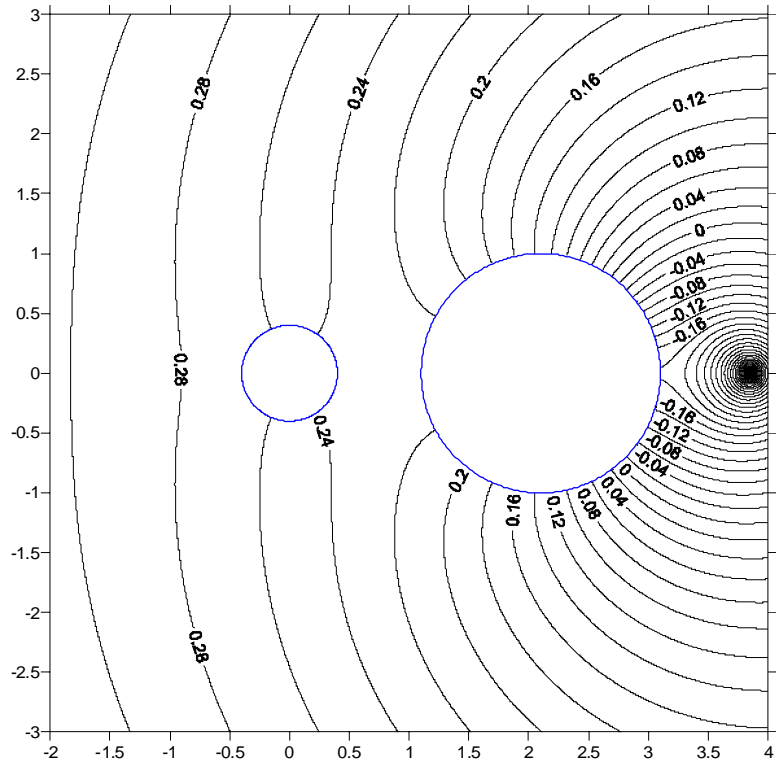


Figure 2-18 Contour of potential using limiting case of $k \rightarrow 0$

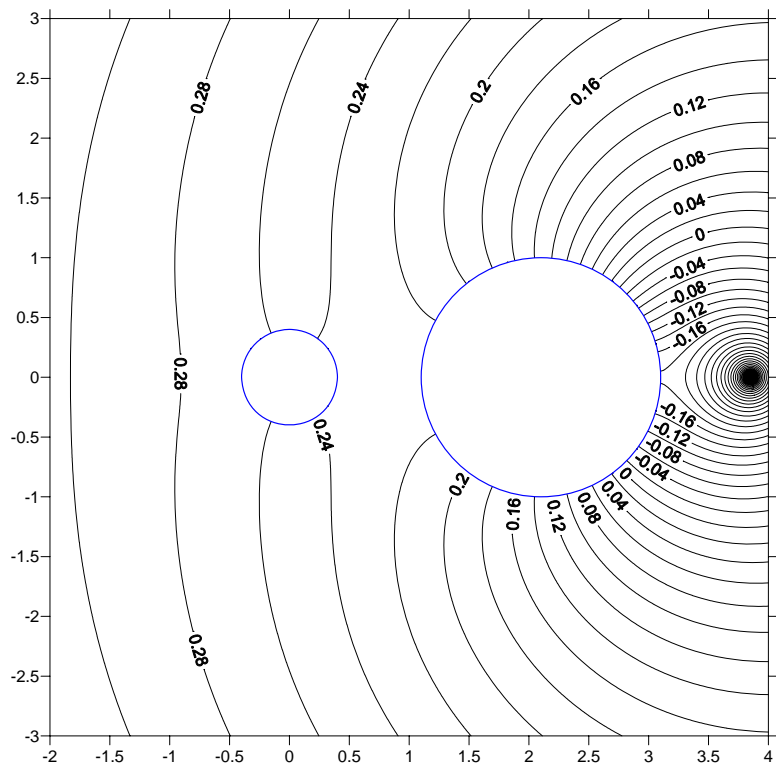


Figure 2-19 Contour of potential using the image method

Chapter 3 Water wave interaction with surface-piercing porous cylinders using the null-field integral equations

Summary

Following the successful experiences of solving water-wave scattering problems for multiple impermeable cylinders [16], we extend the null-field integral formulation to deal with the problems of surface-piercing porous cylinders in this chapter. The null-field integral equations in conjunction with the addition theorem and Fourier series are employed to solve the water-wave problem. In the implementation, the null-field point can be exactly located on the real boundary free of calculating the Cauchy and Hadamard principal values thanks to the introduction of degenerate kernels for fundamental solution. This method can be seen as a semi-analytical approach since errors attribute from the truncation of Fourier series. Not only a systematic approach is proposed but also the effect on the near-trapped modes due to porous cylinders and disorder of layout is examined. It is found that the disorder is more sensitive to suppress the occurrence of near-trapped modes than the porosity. The free-surface elevation is consistent with the results of William and Li [51] and those by using the conventional BEM. Besides, the numerical results of the force on the surface of cylinders agree well with those in the literature.

3.1 Introduction

A general problem in offshore engineering is to determine the wave loading exerted upon a circular cylinder. For a single cylinder, an analytical solution was available by MacCamy and Fuchs [41]. For the general case, we always resort to semi-analytical or numerical solutions. A semi-analytical solution using the wave function expansion was obtained by Spring and Monkmeyer [47] for the diffraction of linear waves by arrays of cylinders. Later, the interaction of water waves with arrays of circular cylinders was studied by Linton and Evans [35] in a similar way of Twersky approach. Linton and

Evans [35] extended this approach to calculate the force in a more neat form. However, the convergence behavior of the null-field integral equation approach is superior to that of Linton and Evans method. For the boundary integral solution, it converges to L_2 energy sense in an exponential order. It is noted that we can deal with other shape of cross section in our approach, if the degenerate kernels corresponding to the special geometry are available. For example, degenerate kernel for the ellipse can be found in the book of Morse and Feshbach [37]. Also, the work of the elliptic case using the method of Linton and Evans is given in the Martin's book [38], and the numerical results are implemented by Chatjigeorgiou and Mavrakos [18]. On the other hand, some formulae are not found in the mathematical handbook or were not derived by mathematicians for the special geometry. That is to say, we have a challenging work in deriving the degenerate kernel for a special geometry case. Besides, our approach can be applied to problems containing both circular and elliptical cylinders since we introduce adaptive coordinate system and vector decomposition. For the Linton and Evans approach, it may have difficulty in their formulation since the addition theorem for translating the polar coordinates to the elliptical coordinates and vice versa is not available to the authors' best knowledge. Simply speaking, the addition theorem is not available to transform Bessel to Mathieu functions when a problem contains circle and ellipse together.

Regarding numerical methods, Au and Brebbia [2, 3] employed the boundary element method (BEM) to calculate the elevation of free surface as well as the resultant force by using constant, linear and quadratic elements. By discretizing the boundary in a more genius way, Zhu and Moule [54] obtained a more accurate result. Chen [5] used the composite BEM to determine the free-surface elevation for the porous cylinders. Besides, Chen *et al.* [16] employed the null-field integral equation approach to study the near-trapped mode. To determine the singular integrals is a critical issue in the boundary integral equation method (BIEM). The present paper is based on the null-field BIEM while the singular integrals are transformed to series sum free of principal-value calculation using bump contour.

Localized oscillations in unbounded media are always referred to trapped modes in different contexts. For example, acoustic resonance, array-guided surface waves, edge waves, Rayleigh-Bloch waves and bound states are similar physical phenomena. Energy in the guided area is stored and can not radiate to infinity in the case of trap wave number. Water wave diffraction and near trapping by a multi-column structure was studied by Evans and Porter [21]. Near-trapped modes were found for four, five and six cylinders. The wave number to excite the trapped modes was determined numerically by detecting the value of ka which results in the maximum force. Dirichelet and Neumann trapped modes of large number of cylinders (100) in an infinite domain were found to approach those of infinite number of cylinders by Maniar and Newman [39]. Real and absolute values for the free-surface elevation were investigated by Evans and Porter [22]. Trapped modes for a semi-infinite domain was studied by Thompson *et al.* [49]. For multiple cylinders in a channel, trapped modes were also found by Evans and Porter [22]. Mathematically speaking, the array-guided cylinders may result in non-trivial solutions of the homogeneous problem at particular values of wave number. It can be understood as eigenvectors corresponding to eigenvalues of certain differential operators on unbounded domains even though there is no characteristic length as mentioned by Linton and McIver [36].

Duclos and Clément [20] extended to consider arrays of unevenly spaced cylinders, displaced randomly from a regular array according to a disorder parameter. They focused on two effects of this spacing irregularity, reduction of peak forces associated to trapped mode phenomena, and regularization of the transmission coefficient for waves propagating through the arrays. However, Duclos and Clément [20] only considered the impermeable cylinders. On the other hand, Williams and Li [51] calculated the free-surface elevation and force for the porous cylinders. Nevertheless, they did not consider the disorder effect. We may wonder what happen for the near-trapped modes if we simultaneously consider the porous cylinder with a disorder. The effect of porosity parameter on the free-surface elevation, force and near-trapped modes will be examined. Also, the reduction of force in the case of near-trapped mode due to disorder is also our interest.

In this chapter, the hydrodynamics of circular porous cylinders is studied by using the null-field integral equation in conjunction with the addition theorem and the Fourier series. The main difference between the present approach and Linton-Evans method is that we use the BIE instead of the wave function expansion. The unknown coefficient here is the Fourier coefficient on the boundary instead of weighting of wave expansion for the domain. The wave interaction problem can be decomposed into two parts. One is an infinite domain with circular boundaries. The other is an interior problem for each cylinder. The interface condition for the porous cylinder is considered as a similar idea of complex spring in the structural dynamics. Force as well as free-surface elevation were calculated and compared with others to check the validity of our formulation. The parameter study for the disorder and porosity on the effect of near-trapped modes will be investigated.

3.2 Problem statement and integral formulation

3.2.1 Problem statement

Irrotational motion of the inviscid and incompressible fluid is small-amplitude which is defined as velocity potential $\Phi(x, y, z; t)$ based on the linear water wave theory. We assume that there are N vertical circular cylinders mounted at $z = -h$ upward to the free surface as shown in Figure 3-1. The governing equation of the water wave problem is the Laplace equation

$$\nabla^2 \Phi(x, y, z; t) = 0, \quad (x, y, z) \in D, \quad (3-1)$$

where ∇^2 and D are the Laplacian operator and the domain of interest, respectively. For satisfying the boundary conditions of (1) seabed, (2) kinematic boundary conditions and (3) dynamic boundary condition at free surface as shown below:

$$(1) \quad -\frac{\partial \Phi}{\partial n} = 0, \quad z = -h(x, y), \quad (3-2)$$

$$(2) \quad -\Phi_z = \varphi_t - \Phi_x \varphi_x - \Phi_y \varphi_y, \quad z = \varphi(x, y; t), \quad (3-3)$$

$$(3) \quad -\Phi_t + gz + \frac{1}{2}(\Phi_x^2 + \Phi_y^2 + \Phi_z^2) = B(t), \quad z = \varphi(x, y; t), \quad (3-4)$$

where $B(t)$ is the Bernoulli constant, g is the acceleration of gravity and $\varphi(x, y, t)$ is

the free-surface elevation, we assume

$$\Phi(x, y, z, t) = \text{Re}\{u(x, y)f(z)e^{-i\omega t}\}, \quad (3-5)$$

where

$$f(z) = \frac{-igA \cosh k(z+h)}{\omega \cosh kh}, \quad (3-6)$$

in which A is the amplitude of incident wave, ω denotes the angular frequency, k represents the wave number, and $i^2 = -1$. The free-surface elevation is defined by

$$\varphi(x, y, t) = \text{Re}\{\eta(x, y)e^{-i\omega t}\}, \quad (3-7)$$

where

$$\eta(x, y) = Au(x, y). \quad (3-8)$$

The potential of incident wave $u_{inc}(x, y)$ is shown below:

$$\begin{aligned} u_{inc}(x, y) &= e^{ik(x \cos \theta_{inc} + y \sin \theta_{inc})} \equiv e^{ik\rho \cos(\phi - \theta_{inc})} \\ &\equiv e^{ik(\bar{x}_j \cos \theta_{inc} + \bar{y}_j \sin \theta_{inc})} \left[J_0(k\rho_j) + 2 \sum_{n=1}^{\infty} (i)^n J_n(k\rho_j) \cos(n(\phi_j - \theta_{inc})) \right], \end{aligned} \quad (3-9)$$

where θ_{inc} is the angle of incident wave, and $\rho = \sqrt{x^2 + y^2}$, $\phi = \arctan(y/x)$.

Substituting Eq. (3-5) into Eq. (3-1), we have

$$(\nabla^2 + k^2)u(x, y) = 0, \quad (x, y) \in D. \quad (3-10)$$

The boundary conditions are shown below:

$$\frac{\partial u^O}{\partial r} = -\frac{\partial u_j^C}{\partial r} = ikG[u_j^C - u^O], \quad (3-11)$$

where the superscripts “O” and “C” denote the regions of ocean and cylinder, respectively, G is the dimensionless parameter of porosity ($G = \rho\omega\gamma/\mu k$) and the dispersion relationship is

$$k \tanh kh = \frac{\omega^2}{g}. \quad (3-12)$$

The dynamic pressure can be obtained by

$$p = -\rho_f \frac{\partial \Phi}{\partial t} = -\rho_f gA \frac{\cosh k(z+h)}{\cosh kh} u(x, y)e^{-i\omega t}, \quad (3-13)$$

where ρ_f is the density of the fluid. The two components of the first-order force X^j on the j th cylinder are given by integrating the pressure over the circular boundary as shown below:

$$X^j = -\frac{\rho_f g A a_j}{k} \tanh kh \int_0^{2\pi} u(x, y) \begin{Bmatrix} \cos \theta_j \\ \sin \theta_j \end{Bmatrix} d\theta_j, \quad (3-14)$$

where a_j denotes the radius of the j th cylinder.

3.2.2 Linear algebraic equation

After locating the null-field point x_j exactly on the i th circular boundary in Eq. (2-17) as shown in Figure 2-2, we have

$$0 = \sum_{j=0}^N \int_{B_j} T^E(\mathbf{s}, \mathbf{x}) u(\mathbf{s}) dB(\mathbf{s}) - \sum_{j=0}^N \int_{B_j} U^E(\mathbf{s}, \mathbf{x}) t(\mathbf{s}) dB(\mathbf{s}), \quad x \in D^c \cup B, \quad (3-15)$$

where N is the number of circular cylinders and B_l denotes the outer boundary for the bounded domain. In case of the infinite problem in Figure 3-2(a), B_l becomes a circular boundary with an infinite radius. If the radiation condition at infinity is satisfied, the B_l integration is null. The origin of observer system is adaptively chosen at the center of circular boundary under integration. The dummy variable in the circular integration is angle (θ) instead of radial coordinate (R). In the real computation, we select the collocation point on the boundary and the integration path of the outer circle is counterclockwise. Otherwise, it is clockwise. For the integration path B_i , the kernels of $U(\mathbf{s}, \mathbf{x})$ and $T(\mathbf{s}, \mathbf{x})$ are respectively expressed in terms of degenerate kernels of Eqs. (2-24) and (2-25) with respect to the observer origin at the center of the corresponding path. The boundary densities of $u(\mathbf{s})$ and $t(\mathbf{s})$ are substituted by using the Fourier series of Eqs. (2-32) and (2-33), respectively. In the B_j integration, we set the origin of the observer system to collocate at the center c_j of B_j to fully utilize the degenerate kernel and Fourier series. By moving the null-field point exactly on the real boundary B_j from outside of the domain D^c in the numerical implementation, a linear algebraic system is obtained. For the exterior problem of infinite domain in Figure 3-2(b), we have

$$[\mathbf{U}^I] \{ \mathbf{t}^O - \mathbf{t}^{inc} \} = [\mathbf{T}^I] \{ \mathbf{u}^O - \mathbf{u}^{inc} \}. \quad (3-16)$$

For the interior problem of each cylinder in Fig. 3-2(c), we have

$$[\mathbf{U}^E] \{ \mathbf{t}^C \} = [\mathbf{T}^E] \{ \mathbf{u}^C \}, \quad (3-17)$$

where $[\mathbf{U}^I]$, $[\mathbf{T}^I]$, $[\mathbf{U}^E]$ and $[\mathbf{T}^E]$ are the influence matrices with a dimension of

$N \times (2M + 1)$ by $N \times (2M + 1)$, $\{\mathbf{t}^O\}$, $\{\mathbf{t}^{inc}\}$, $\{\mathbf{u}^O\}$, $\{\mathbf{u}^{inc}\}$, $\{\mathbf{t}^C\}$ and $\{\mathbf{u}^C\}$ denote the column vectors of Fourier coefficients with a dimension of $N \times (2M + 1)$ by 1 in which those are defined as follows:

$$[\mathbf{U}^I] = \begin{bmatrix} \mathbf{U}_{00}^I & \mathbf{U}_{01}^I & \cdots & \mathbf{U}_{0N}^I \\ \mathbf{U}_{10}^I & \mathbf{U}_{11}^I & \cdots & \mathbf{U}_{1N}^I \\ \vdots & \vdots & \ddots & \vdots \\ \mathbf{U}_{N0}^I & \mathbf{U}_{N1}^I & \cdots & \mathbf{U}_{NN}^I \end{bmatrix}, \quad (3-18)$$

$$[\mathbf{T}^I] = \begin{bmatrix} \mathbf{T}_{00}^I & \mathbf{T}_{01}^I & \cdots & \mathbf{T}_{0N}^I \\ \mathbf{T}_{10}^I & \mathbf{T}_{11}^I & \cdots & \mathbf{T}_{1N}^I \\ \vdots & \vdots & \ddots & \vdots \\ \mathbf{T}_{N0}^I & \mathbf{T}_{N1}^I & \cdots & \mathbf{T}_{NN}^I \end{bmatrix}, \quad (3-19)$$

$$[\mathbf{U}^E] = \begin{bmatrix} \mathbf{U}_{00}^E & 0 & \cdots & 0 \\ 0 & \mathbf{U}_{11}^E & \cdots & 0 \\ \vdots & \vdots & \ddots & \vdots \\ 0 & 0 & \cdots & \mathbf{U}_{NN}^E \end{bmatrix}, \quad (3-20)$$

$$[\mathbf{T}^E] = \begin{bmatrix} \mathbf{T}_{00}^E & 0 & \cdots & 0 \\ 0 & \mathbf{T}_{11}^E & \cdots & 0 \\ \vdots & \vdots & \ddots & \vdots \\ 0 & 0 & \cdots & \mathbf{T}_{NN}^E \end{bmatrix}, \quad (3-21)$$

$$\{\mathbf{u}^O\} = \begin{Bmatrix} \mathbf{u}_0^O \\ \mathbf{u}_1^O \\ \vdots \\ \mathbf{u}_N^O \end{Bmatrix}, \quad \{\mathbf{u}^{inc}\} = \begin{Bmatrix} \mathbf{u}_0^{inc} \\ \mathbf{u}_1^{inc} \\ \vdots \\ \mathbf{u}_N^{inc} \end{Bmatrix}, \quad \{\mathbf{t}^O\} = \begin{Bmatrix} \mathbf{t}_0^O \\ \mathbf{t}_1^O \\ \vdots \\ \mathbf{t}_N^O \end{Bmatrix}, \quad \{\mathbf{t}^{inc}\} = \begin{Bmatrix} \mathbf{t}_0^{inc} \\ \mathbf{t}_1^{inc} \\ \vdots \\ \mathbf{t}_N^{inc} \end{Bmatrix}, \quad (3-22)$$

$$\{\mathbf{u}^C\} = \begin{Bmatrix} \mathbf{u}_0^C \\ \mathbf{u}_1^C \\ \vdots \\ \mathbf{u}_N^C \end{Bmatrix}, \quad \{\mathbf{t}^C\} = \begin{Bmatrix} \mathbf{t}_0^C \\ \mathbf{t}_1^C \\ \vdots \\ \mathbf{t}_N^C \end{Bmatrix}, \quad (3-23)$$

where the first subscript “ j ” ($j=0, 1, 2, \dots, N$) in $[\mathbf{U}_{ji}^E]$, $[\mathbf{T}_{ji}^E]$, $[\mathbf{U}_{ji}^I]$ and $[\mathbf{T}_{ji}^I]$ denotes the index of the j th circular boundary where the collocation point is located and

the second subscript “ i ” ($i=0, 1, 2, \dots, N$) denotes the index of the i th circular boundary when integrating on each boundary data $\{\mathbf{t}^O - \mathbf{t}^{inc}\}$, $\{\mathbf{u}^O - \mathbf{u}^{inc}\}$ in Figure 3-2(d), $\{\mathbf{t}^C\}$ and $\{\mathbf{u}^C\}$ in Figure 3-2(c), N is the number of circular cylinders in the domain and the number M indicates the truncated terms of Fourier series. It is noted that $\{\mathbf{u}^{inc}\}$ and $\{\mathbf{t}^{inc}\}$ in Figure 3-2(e) are the free-surface elevation and flux due to the incident wave. The coefficient matrix of the linear algebraic system is partitioned into blocks, and each off-diagonal block corresponds to the influence matrices between two different circular boundaries. The diagonal blocks are the influence matrices due to itself in each individual circle. After uniformly collocating the point along the k th circular boundary, the submatrix can be written as

$$[\mathbf{U}_{ji}] = \begin{bmatrix} \mathbf{U}_{ji}^{0c}(\phi_1) & \mathbf{U}_{ji}^{1c}(\phi_1) & \mathbf{U}_{ji}^{2s}(\phi_1) & \cdots & \mathbf{U}_{ji}^{Mc}(\phi_1) & \mathbf{U}_{ji}^{Ms}(\phi_1) \\ \mathbf{U}_{ji}^{0c}(\phi_2) & \mathbf{U}_{ji}^{1c}(\phi_2) & \mathbf{U}_{ji}^{2s}(\phi_2) & \cdots & \mathbf{U}_{ji}^{Mc}(\phi_2) & \mathbf{U}_{ji}^{Ms}(\phi_2) \\ \mathbf{U}_{ji}^{0c}(\phi_3) & \mathbf{U}_{ji}^{1c}(\phi_3) & \mathbf{U}_{ji}^{2s}(\phi_3) & \cdots & \mathbf{U}_{ji}^{Mc}(\phi_3) & \mathbf{U}_{ji}^{Ms}(\phi_3) \\ \vdots & \vdots & \vdots & & \vdots & \vdots \\ \mathbf{U}_{ji}^{0c}(\phi_{2M}) & \mathbf{U}_{ji}^{1c}(\phi_{2M}) & \mathbf{U}_{ji}^{2s}(\phi_{2M}) & \cdots & \mathbf{U}_{ji}^{Mc}(\phi_{2M}) & \mathbf{U}_{ji}^{Ms}(\phi_{2M}) \\ \mathbf{U}_{ji}^{0c}(\phi_{2M+1}) & \mathbf{U}_{ji}^{1c}(\phi_{2M+1}) & \mathbf{U}_{ji}^{2s}(\phi_{2M+1}) & \cdots & \mathbf{U}_{ji}^{Mc}(\phi_{2M+1}) & \mathbf{U}_{ji}^{Ms}(\phi_{2M+1}) \end{bmatrix}, \quad (3-24)$$

$$[\mathbf{T}_{ji}] = \begin{bmatrix} \mathbf{T}_{ji}^{0c}(\phi_1) & \mathbf{T}_{ji}^{1c}(\phi_1) & \mathbf{T}_{ji}^{2s}(\phi_1) & \cdots & \mathbf{T}_{ji}^{Mc}(\phi_1) & \mathbf{T}_{ji}^{Ms}(\phi_1) \\ \mathbf{T}_{ji}^{0c}(\phi_2) & \mathbf{T}_{ji}^{1c}(\phi_2) & \mathbf{T}_{ji}^{2s}(\phi_2) & \cdots & \mathbf{T}_{ji}^{Mc}(\phi_2) & \mathbf{T}_{ji}^{Ms}(\phi_2) \\ \mathbf{T}_{ji}^{0c}(\phi_3) & \mathbf{T}_{ji}^{1c}(\phi_3) & \mathbf{T}_{ji}^{2s}(\phi_3) & \cdots & \mathbf{T}_{ji}^{Mc}(\phi_3) & \mathbf{T}_{ji}^{Ms}(\phi_3) \\ \vdots & \vdots & \vdots & \ddots & \vdots & \vdots \\ \mathbf{T}_{ji}^{0c}(\phi_{2M}) & \mathbf{T}_{ji}^{1c}(\phi_{2M}) & \mathbf{T}_{ji}^{2s}(\phi_{2M}) & \cdots & \mathbf{T}_{ji}^{Mc}(\phi_{2M}) & \mathbf{T}_{ji}^{Ms}(\phi_{2M}) \\ \mathbf{T}_{ji}^{0c}(\phi_{2M+1}) & \mathbf{T}_{ji}^{1c}(\phi_{2M+1}) & \mathbf{T}_{ji}^{2s}(\phi_{2M+1}) & \cdots & \mathbf{T}_{ji}^{Mc}(\phi_{2M+1}) & \mathbf{T}_{ji}^{Ms}(\phi_{2M+1}) \end{bmatrix}, \quad (3-25)$$

where ϕ_i ($i=1, 2, \dots, 2M+1$) is the polar angle of the collocating point \mathbf{x}_m along the boundary. It is noted that the superscript “0s” in Eq. (3-24) disappears since $\sin(0\theta) = 0$, and the element of $[\mathbf{U}_{ji}]$ and $[\mathbf{T}_{ji}]$ are defined as

$$U_{ji}^{nc} = \int_{B_i} U(s_i, \mathbf{x}_m) \cos(n\theta_i) R_i d\theta_i \quad (3-26)$$

$$U_{ji}^{ns} = \int_{B_i} U(s_i, \mathbf{x}_m) \sin(n\theta_i) R_i d\theta_i \quad (3-27)$$

$$T_{ji}^{nc} = \int_{B_i} T(s_i, \mathbf{x}_m) \cos(n\theta_i) R_i d\theta_i \quad (3-28)$$

$$T_{ji}^{ms} = \int_{B_i} T(s_i, x_m) \sin(n\theta_i) R_i d\theta_i \quad (3-29)$$

where $n=1, 2, \dots, M$. By matching interface condition of in Eq. (3-11) and assembling matrices of Eqs. (3-16) and (3-17), we have

$$\begin{bmatrix} \mathbf{T}^I & -\mathbf{U}^I & 0 & 0 \\ 0 & 0 & \mathbf{T}^E & -\mathbf{U}^E \\ 0 & -\mathbf{I} & 0 & -\mathbf{I} \\ ikG & 0 & -ikG & \mathbf{I} \end{bmatrix} \begin{Bmatrix} \mathbf{u}^O \\ \mathbf{t}^O \\ \mathbf{u}^C \\ \mathbf{t}^C \end{Bmatrix} = \begin{bmatrix} \mathbf{W}_{inc} \\ 0 \\ 0 \\ 0 \end{bmatrix}, \quad (3-30)$$

where the matrix $[\mathbf{I}]$ is an identity matrix and $\mathbf{W}_{inc} = [\mathbf{T}^I] \{\mathbf{u}^{inc}\} - [\mathbf{U}^I] \{\mathbf{t}^{inc}\}$ is the forcing term. After obtaining the unknown Fourier coefficients, we can obtain the free-surface elevation by using Eq. (2-19).

3.2.3 Perturbation of ordered cylinder arrangements

An arrangement of 16 cylinders according to a regular three-rows disposition is shown in Figure 3-4(b). For the purpose of disturbing the regular arrangement, a perturbation of disposition is given. The displacement of each cylinder center apart from its original periodical position is defined as follows:

$$\begin{aligned} \Delta x_j &= \gamma_j p \tau \cos(2\pi\gamma_j), \\ \Delta y_j &= \gamma_j p \tau \sin(2\pi\gamma_j), \end{aligned} \quad (3-31)$$

where γ_j is a random variable in the range $[0,1]$, the maximum permissible displacement p is equal to $b-a$ and τ is a global disorder parameter. The distance between the two centers of identical cylinders is $2b$ where the radii of cylinders are a .

3.3 Illustrative examples

Effect of the disorder (τ) as well as the porous parameter (G) on the near-trapped modes will be addressed here. Figure 3-5 (a) and (b) show the original state for the trapped mode without disturbance due to disorder ($\tau = 0$) and porous parameter ($G=0$) in the case of wave number $k=4.08482$ by using Evans and Porter's approach and our approach, respectively. Both figures show the contour of absolute value of free-surface

elevation for $a/b=0.8$. As predicted by Evans and Porter [22], we reconfirm that over 150 times of the amplitude of incident wave and 54 times of the force over one isolated cylinder by using our approach. By considering the surface-piercing cylinder, the influence of porosity on the magnitude of the free-surface elevation in the vicinity of a four-cylinders array is obvious as shown in Figure 3-6. The reduced order of $1/2$ is observed for $G=1$. For the array of three sets (10 cylinders), the near-trapped mode is also observed by using our approach as shown in Figure 3-7. For one set of six cylinders, Figure 3-8 (a) and (b) also show the contour plots of trapped modes by using Evan and Porter's approach and our method, respectively. For the three sets of fourteen cylinders, the near-trapped modes are shown in Figure 3-9. Figure 3-10 shows the near-trapped mode for the five sets of twenty two cylinders. Both figures are the results of zero disorder. For the five sets of sixteen cylinders as shown in Figure 3-4, contour plots of the maximum free-surface elevation are shown in Figures 3-11 (a) and (b) by using the Duclos and Clément method [20] and our approach, respectively. A near-trapped mode also appears for the same wave number of $k=4.08482$ as the case of four cylinders in Figure 3-5. The maximum wave amplitude is predicted to be about 150 times by using both approaches. We also show the 3-D plot of our result in Figure 3-11 (c). Figures 3-13 (a) and (b) show the force experienced by cylinder No.3 of the linear array in Figure 3-4(b) and cylinder 1 of four cylinder (Figure 3-4(a)) of the circular cylinders by using the Duclos and Clément's method [20] and our approach, respectively. Agreement is observed for the maximum resultant force. For this critical wave number, we find a very large and sharp peak up to 46 times the force on a single identical cylinder in the same field.

Effect of disorder (impermeable case)

As shown in Figure 3-11 (a), an original state without disorder and porous effect is considered. Here, the effect of disorder is our main concern. Following the definition of disorder parameter τ , two random cases of $\tau = 0.1$ were reported by Duclos and Clément [20] as shown in Figures 3-13 (a) and (b). The appearance of the near-trapped mode is dramatically suppressed. To test the accuracy of our approach for the disorder

effect, Figures 3-14 (a)-(e) show that the contour plots of the trapped modes are effectively suppressed for $\tau = 0.1$, $\tau = 0.3$, $\tau = 0.5$, $\tau = 0.7$ and $\tau = 0.9$, respectively. The corresponding 3D plots are also shown in Figures 3-15 (a)-(e).

Effect of porous parameter (disorder free)

For the single impermeable cylinder ($G=0$), two approaches, the BEM and the null-field BIEM, are employed to calculate the free-surface elevation by Chen and the author, respectively. Contour plots are shown in Figures 3-16 (a) and (b), respectively. For the 3D plot, the results by using the three approaches, Linton and Evans's approach, the BEM and the null-field BIEM, are shown in Figures 3-17 (a)-(c), respectively. For the porous cylinder of $G = 1$, the results of the free-surface elevation in contour plot and 3D plot are shown in Figures 3-18 and 3-19.

For the four impermeable cylinders, zero degree incident wave is considered for simplicity. The contour distribution and 3D plot of the free surface elevation shown in Figures 3-20 and 3-21. For the porous case of porosity $G = 1$, the results of the free-surface elevation in contour plot and 3D plot are shown in Figures. 3-22 and 3-23.

Effect of impinging angle of incident wave

For the 45 degrees of incident wave to impermeable cylinders, the contour and 3D plots of the free-surface elevation are shown in Figures 3-24 and 3-25, respectively. To consider the porous effect ($G = 1$), the contour distribution and 3D plot of the free-surface elevation are shown in Figure 3-26 and 3-27.

Effect of spacing

The parameter of b/a is chosen as 2 for Figures 3-20~3-27. If the space is double, i.e., $b/a=4$, we obtained all the results as shown in Figures 3-28~3-33 for comparison with Figures 3-20~3-27. For six cylinders in one array, Figures 3-34 (a) and (b) show the contour plots of free-surface elevation for the impermeable and porous cases, respectively. Available result of William and Li's [51] 3D plot for the free-surface elevation of impermeable case in Figure 3-35 (a) matches well with our data in Figure 3-35 (b). For the porous case of $G=1$, our data matches well with the William and Li's

result as shown in Figures 3-36 (a) and (b). For the 45 degrees of incident wave in this case, our results are shown in Figures 3-37 (a) and (b) for impermeable and porous case, respectively. Their 3D plots are shown in Figures 3-38 and 3-39. Similarly, the results of the 90 degrees are also shown in Figures 3-40~3-42. To verify the effect of porous parameter on the trapped mode of sixteen cylinders in Figure 3-11, Figure 3-43 shows the contour of the maximum free-surface elevation. The maximum value of 150 reduces to 75 due to the porous parameter of $G=1.0$.

Effect of porous parameter and disorder together

To verify both the effects of disorder and porosity, a sixteen-cylinders example is demonstrated here. Figure 3-11 shows the contour of the free-surface elevation without disorder and porosity. By considering the perturbation parameter $\tau = 0.1$, the maximum free-surface elevation dramatically reduces to 3.90 from the original value of 150 in Figure 3-11. By only considering the porous cylinder without disorder, the maximum free-surface elevation in Figure 3-43 is deduced to half (75) in Figure 3-11 (150). If the perturbation parameter and porosity are simultaneously considered, the maximum free-surface elevation reduces to 2.70 in Figure 4-44. It indicates that disorder dominate the maximum free-surface elevation.

3.4 Conclusions

In this chapter, not only a systematic approach was employed to investigate the water-wave interaction with arrays of surface-piercing porous cylinders, but also the effect of porosity and disorder on the force in case of trapped modes was also examined. The case of impermeable cylinder case can be treated as a special case with $G=0$. Addition theorem or so-called the degenerate kernel is adopted in the null-field integral formulation. Therefore, the singular integrals using bump integrals for principal values can be avoided. Numerical results including the free-surface elevation and resultant forces on each cylinder have been presented to illustrate the effect of porous and disorder parameters on the force in case of trapped modes. It is found that the disorder is more sensitive to suppress the occurrence of near-trapped modes than the porosity.

Good agreements are observed after comparing with the results obtained in the literature.

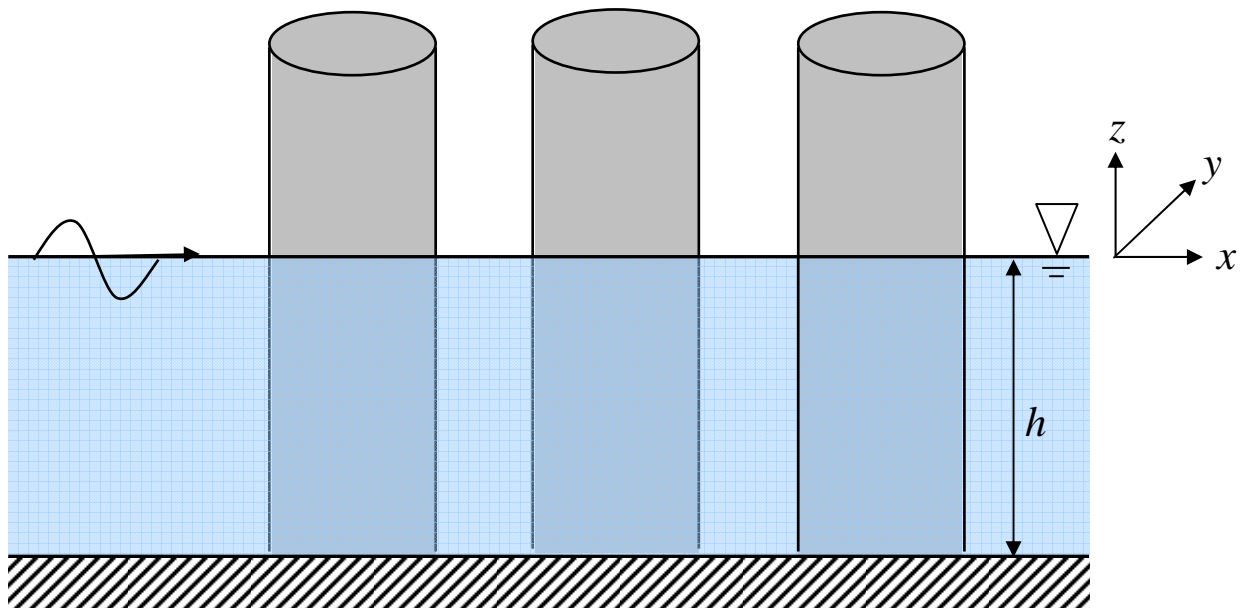


Figure 3-1 Problem statement of water waves with an array of vertical cylinders

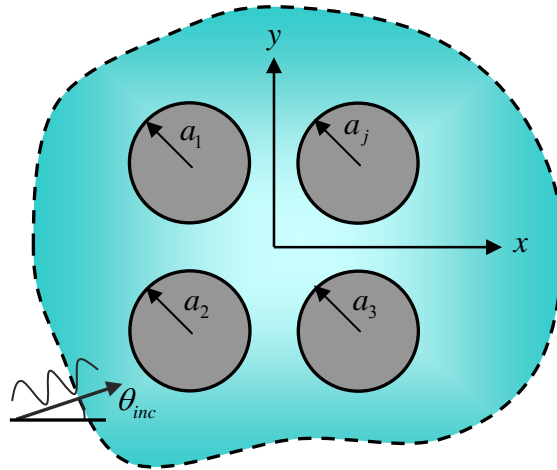


Figure 3-2 (a) Water wave problem with multiple circular cylinders

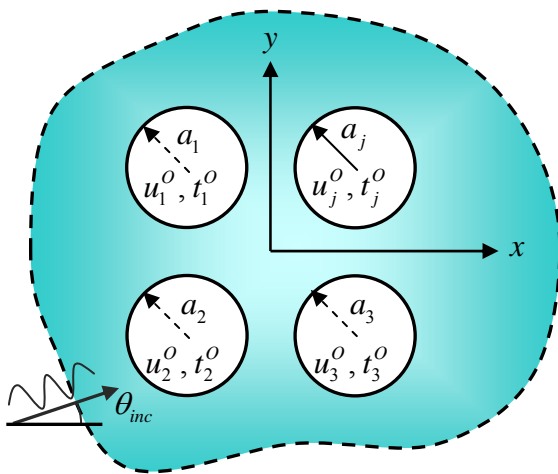


Figure 3-2 (b) Infinite domain with multiple cylinders subject to incident water wave

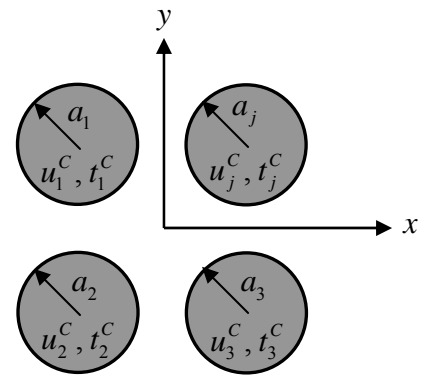


Figure 3-2 (c) An interior Helmholtz problem for each circular cylinder

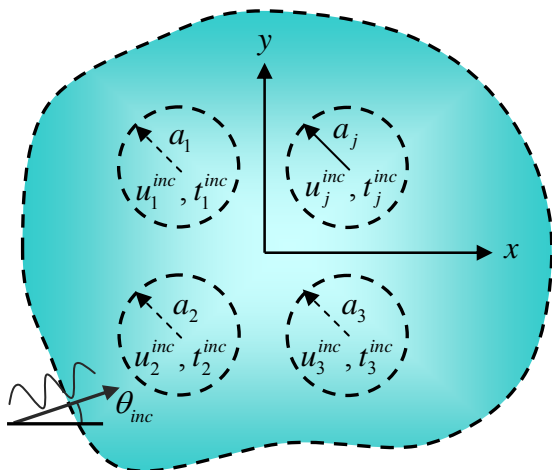


Figure 3-2 (d) An infinite domain subject to the incident water wave

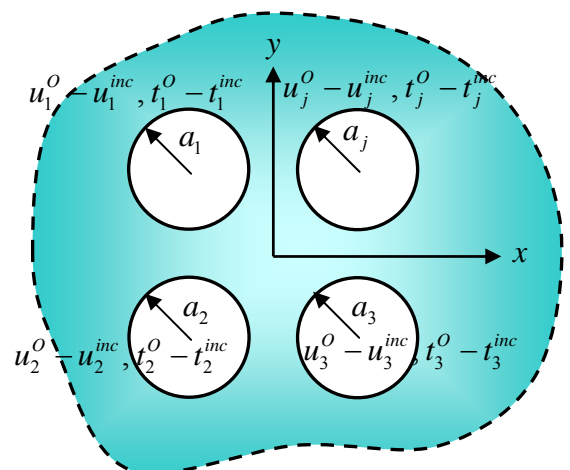


Figure 3-2 (e) An exterior Helmholtz problem in an infinite domain

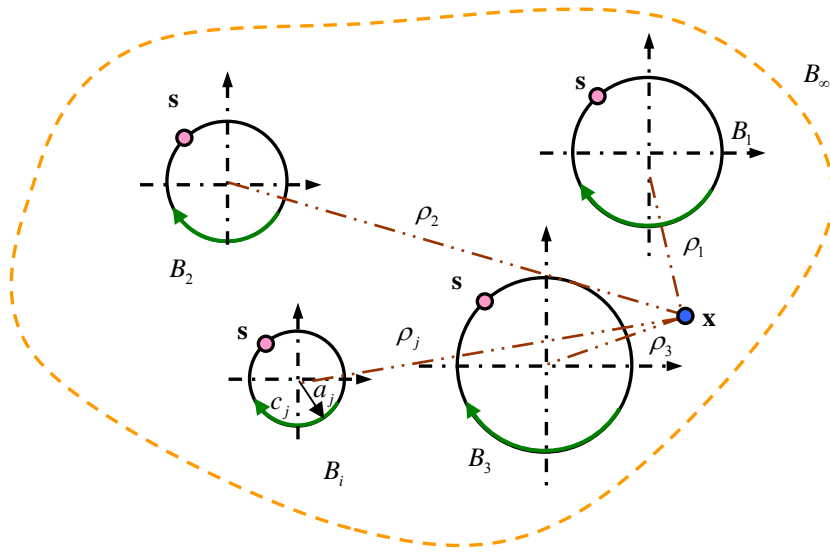
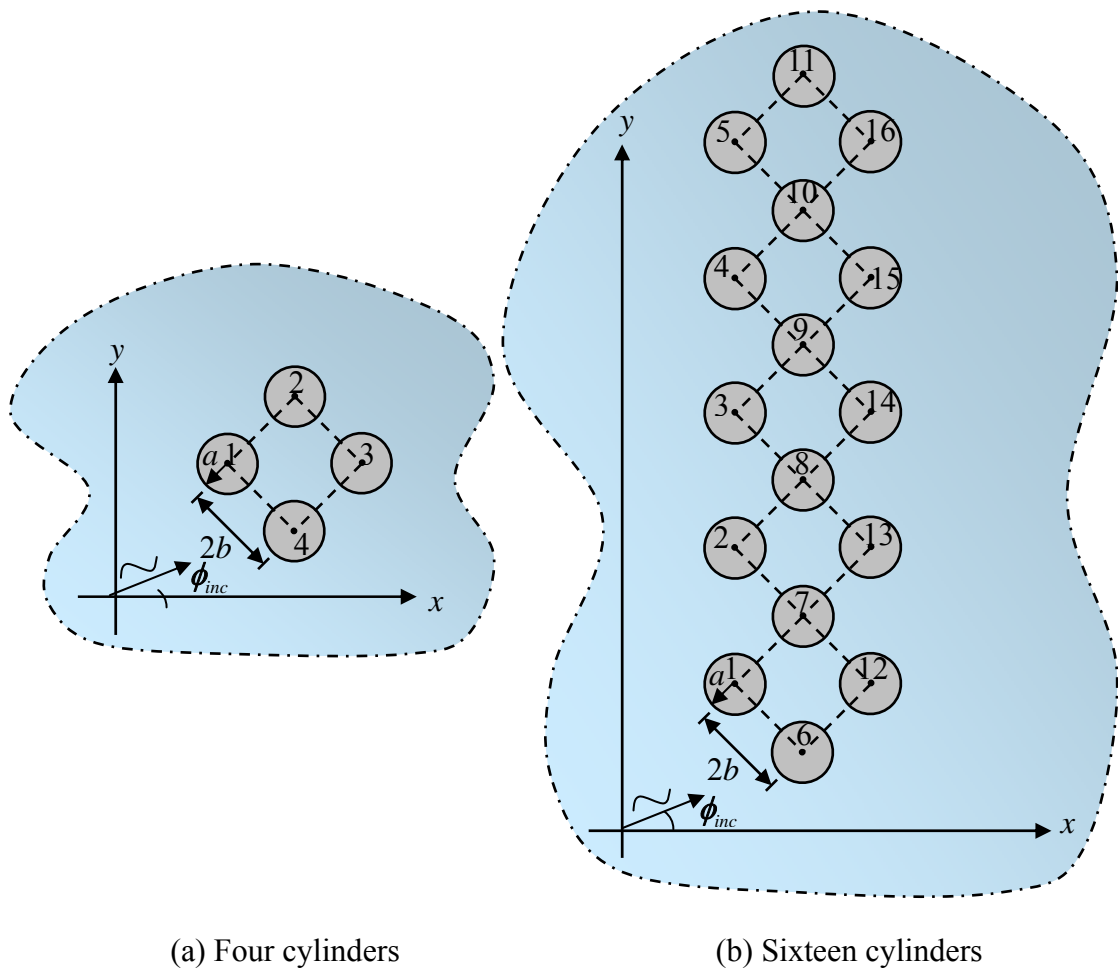


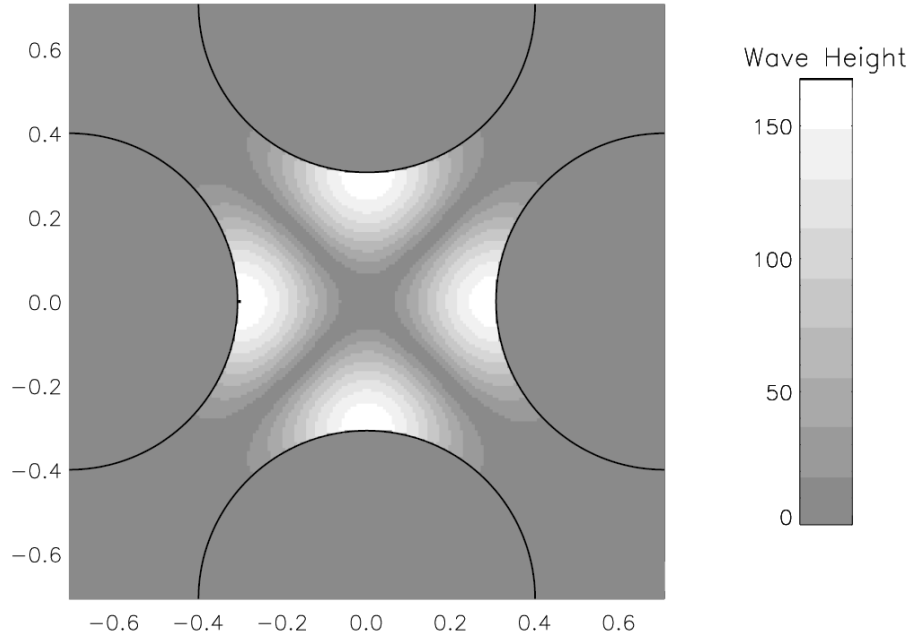
Figure 3-3 Sketch of the BIE for the domain point



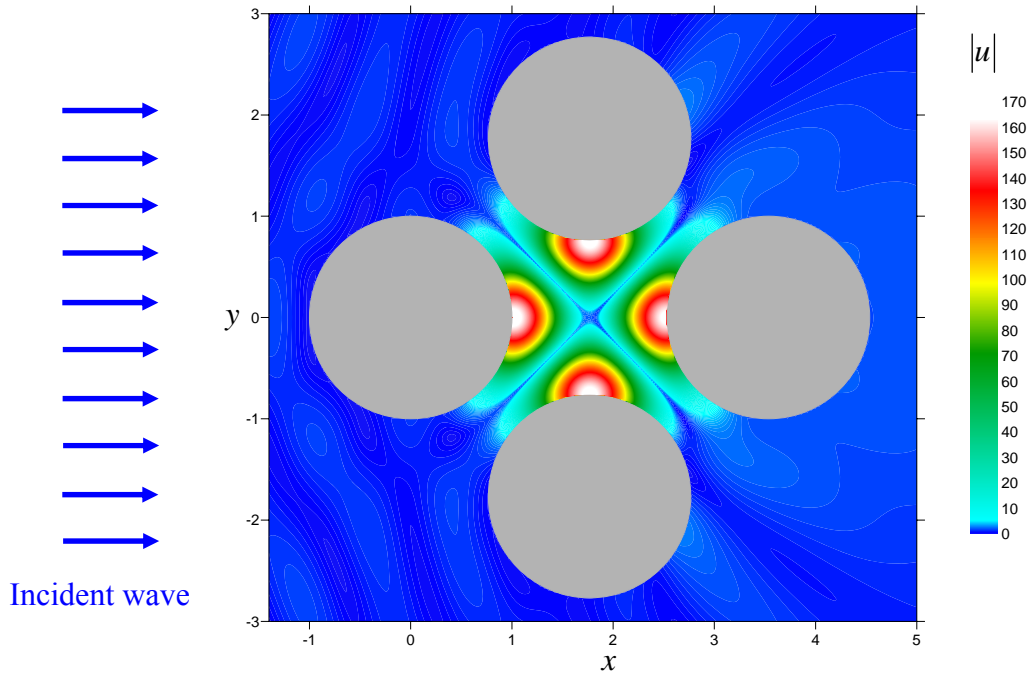
(a) Four cylinders

(b) Sixteen cylinders

Figure 3-4 Configuration of (a) four cylinders and (b) sixteen cylinders



(a) Evans and Porter [22]



(b) Present method ($M=20$)

Figure 3-5 Near-trapped mode for the four cylinders at $ka=4.08482$ ($a/b=0.8$, $G=0.0$, $\tau=0.0$, $H=2$)

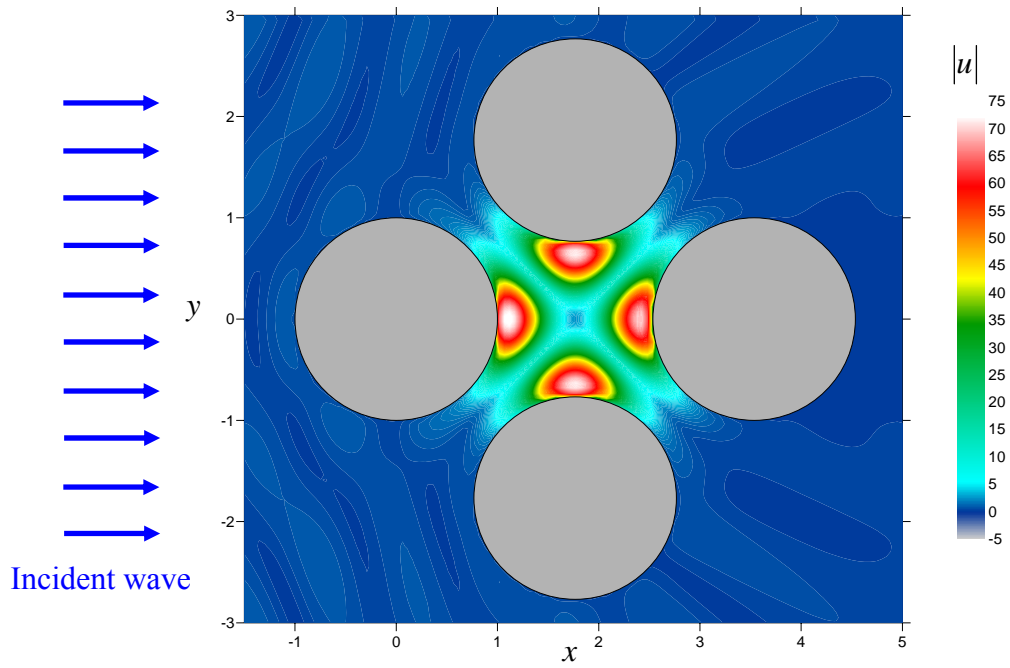


Figure 3-6 Surface-piercing porous cylinders at $ka=4.08482$ ($a/b=0.8$, $M=20$, $G=1.0$, $\tau = 0.0$, $H = 2$)

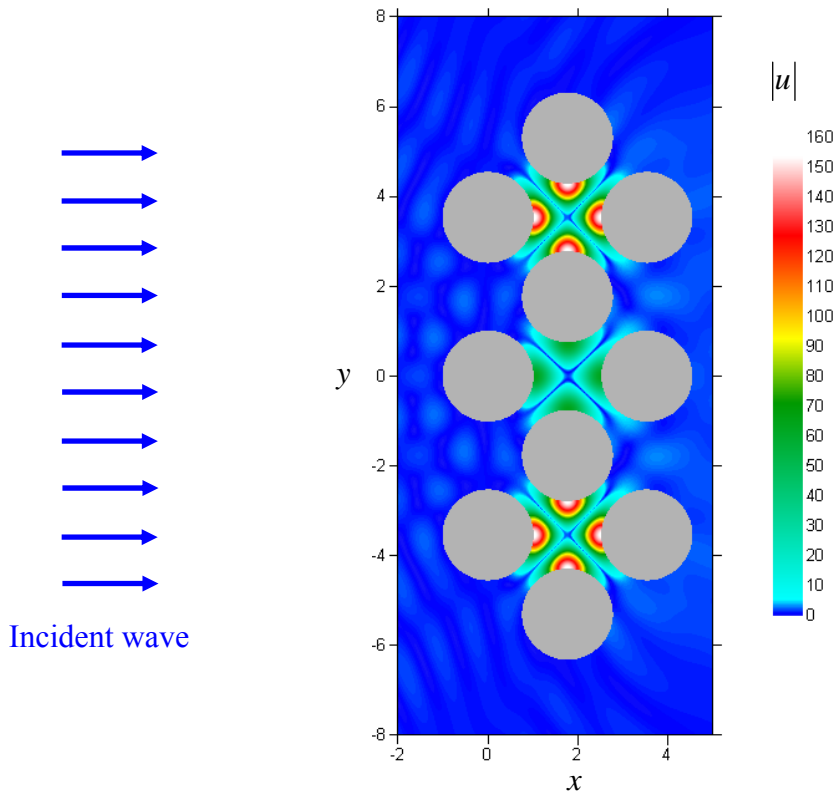
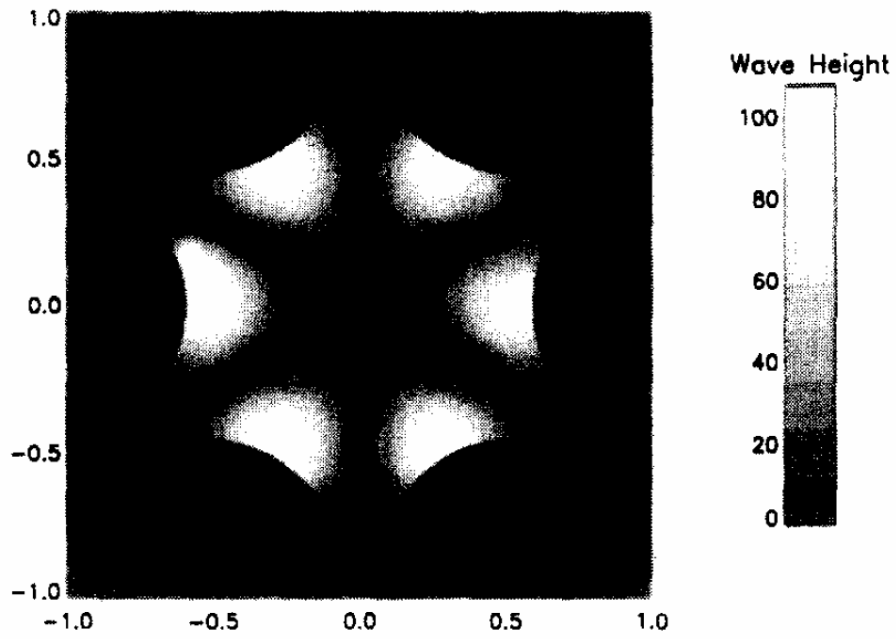
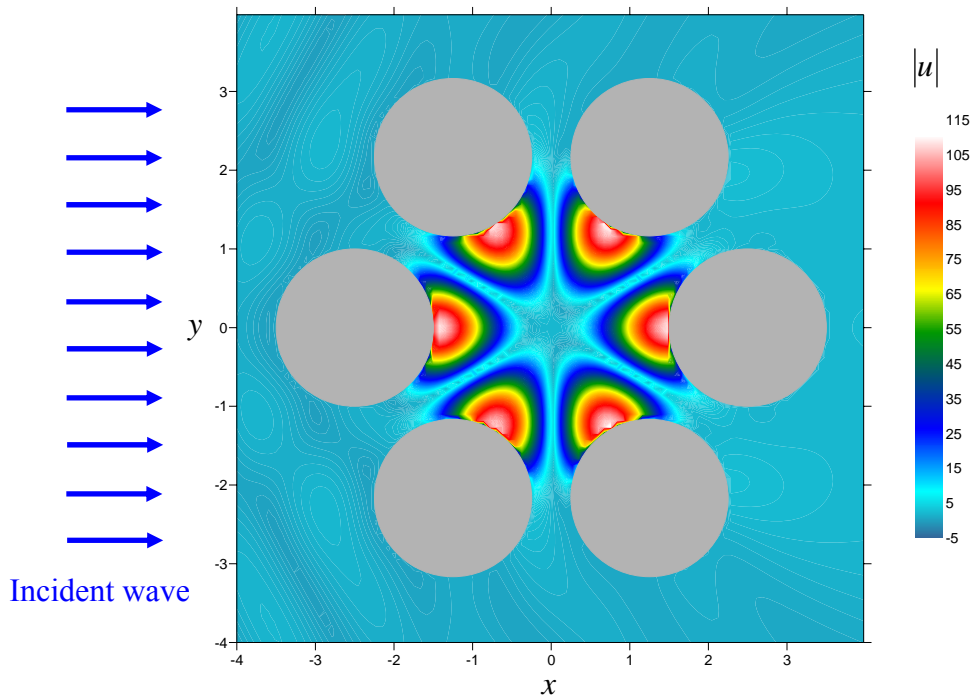


Figure 3-7 Near-trapped mode for the ordered pile array at $ka=4.08482$ ($a/b=0.8$, $G=0.0$, $M=20$, $\tau = 0.0$, $H = 2$)



(a) Evans and Porter [21]



(b) Present method ($M=20$) (2009)

Figure 3-8 Near-trapped mode for the six cylinders at $ka=2.92921$ ($a/b=0.8$, $G=0.0$, $\tau = 0.0$, $H = 2$)

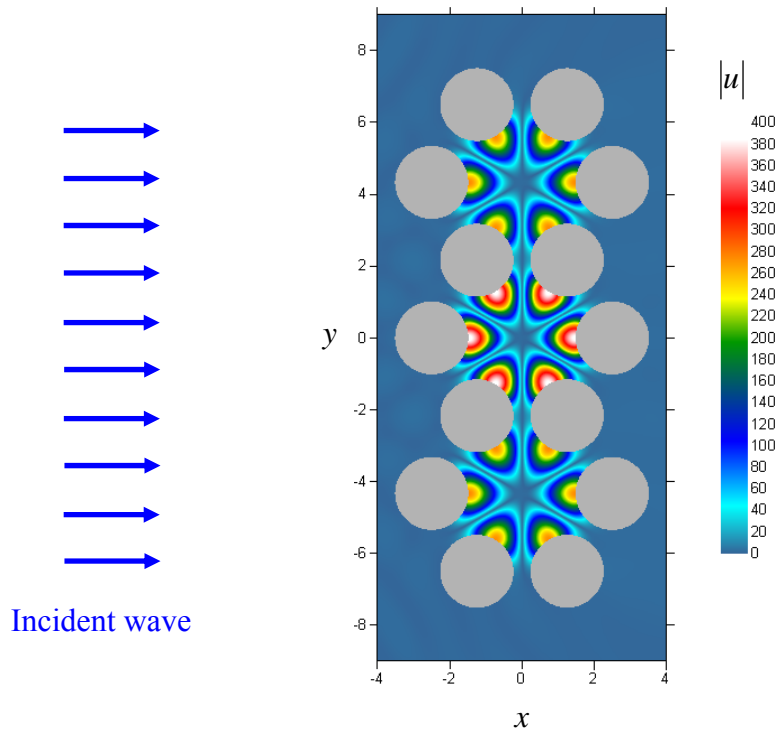


Figure 3-9 Near-trapped mode for the ordered pile array at $ka=2.928911$ ($a/b=0.8$, $G=0.0$, $M=20$, $\tau = 0.0$, $H = 2$)

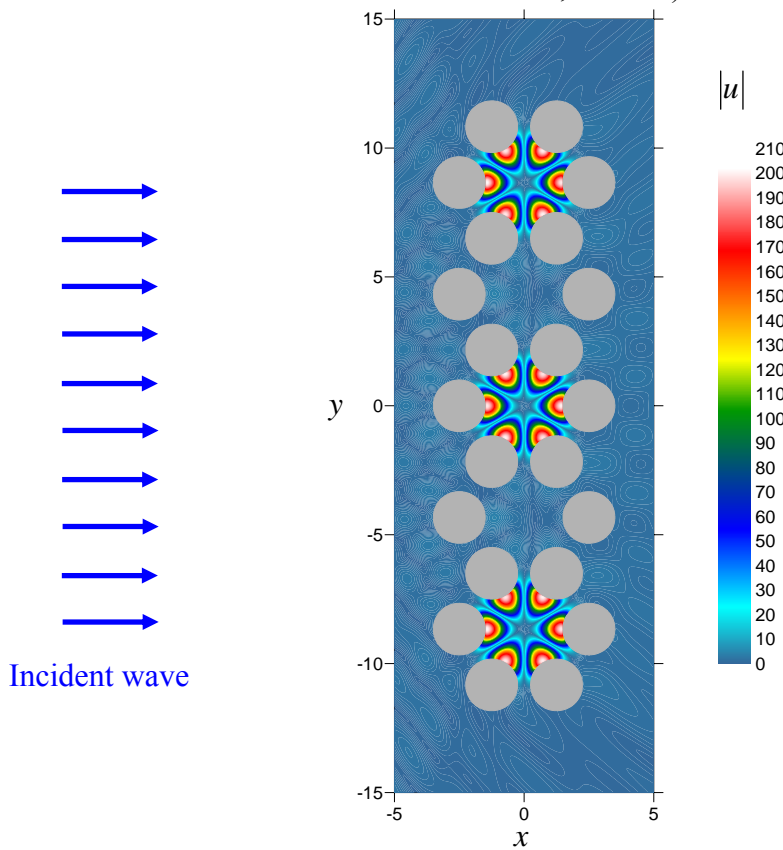
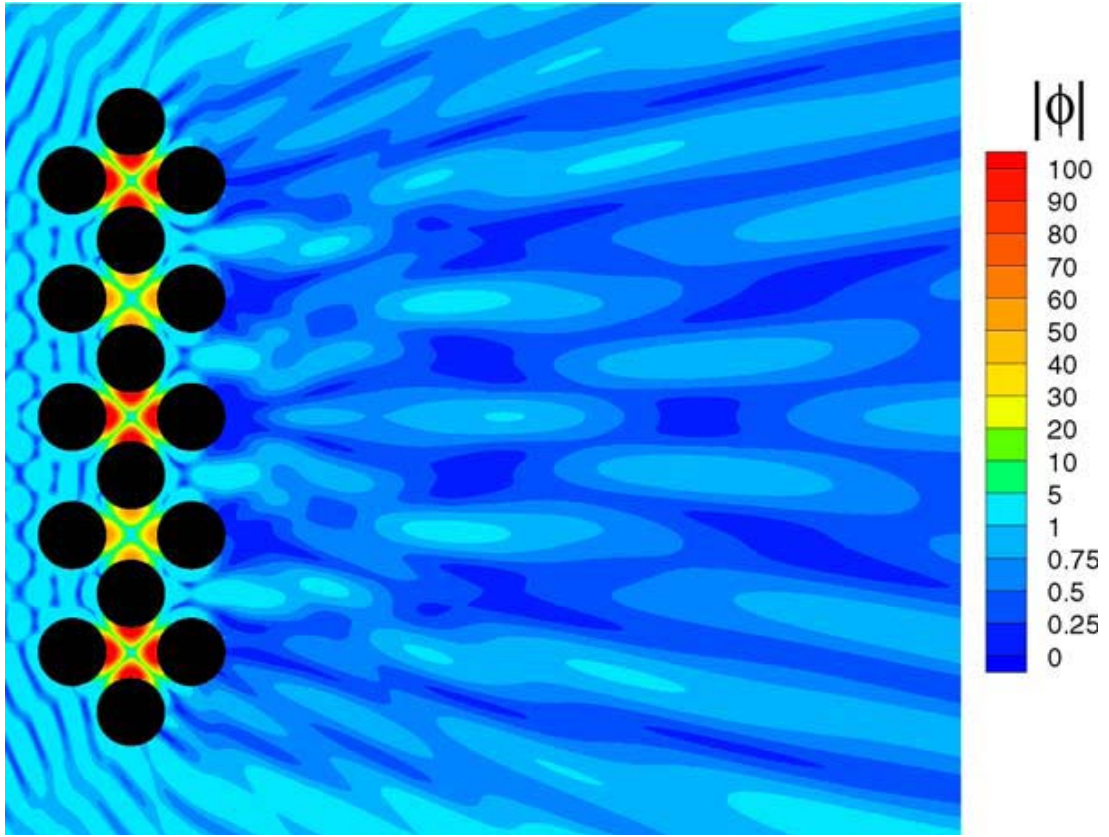
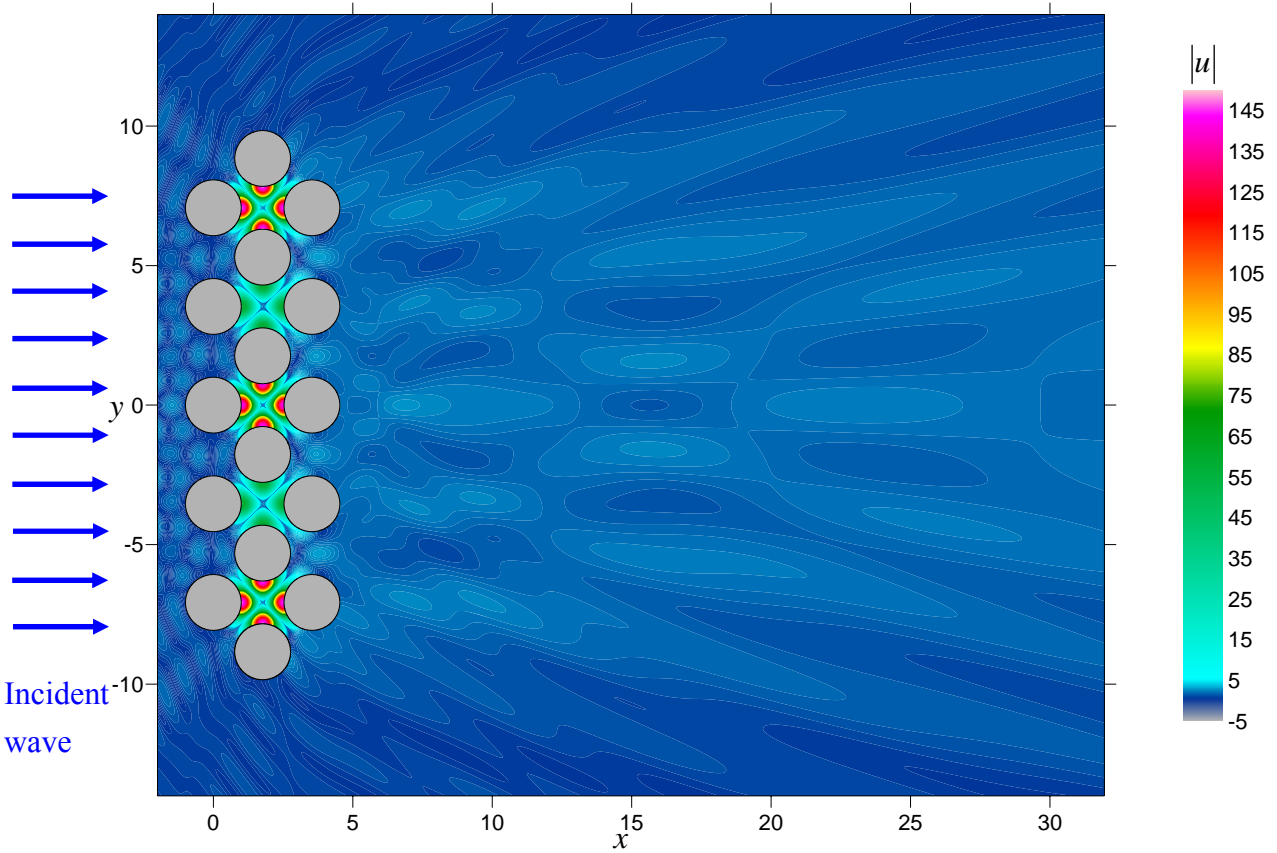


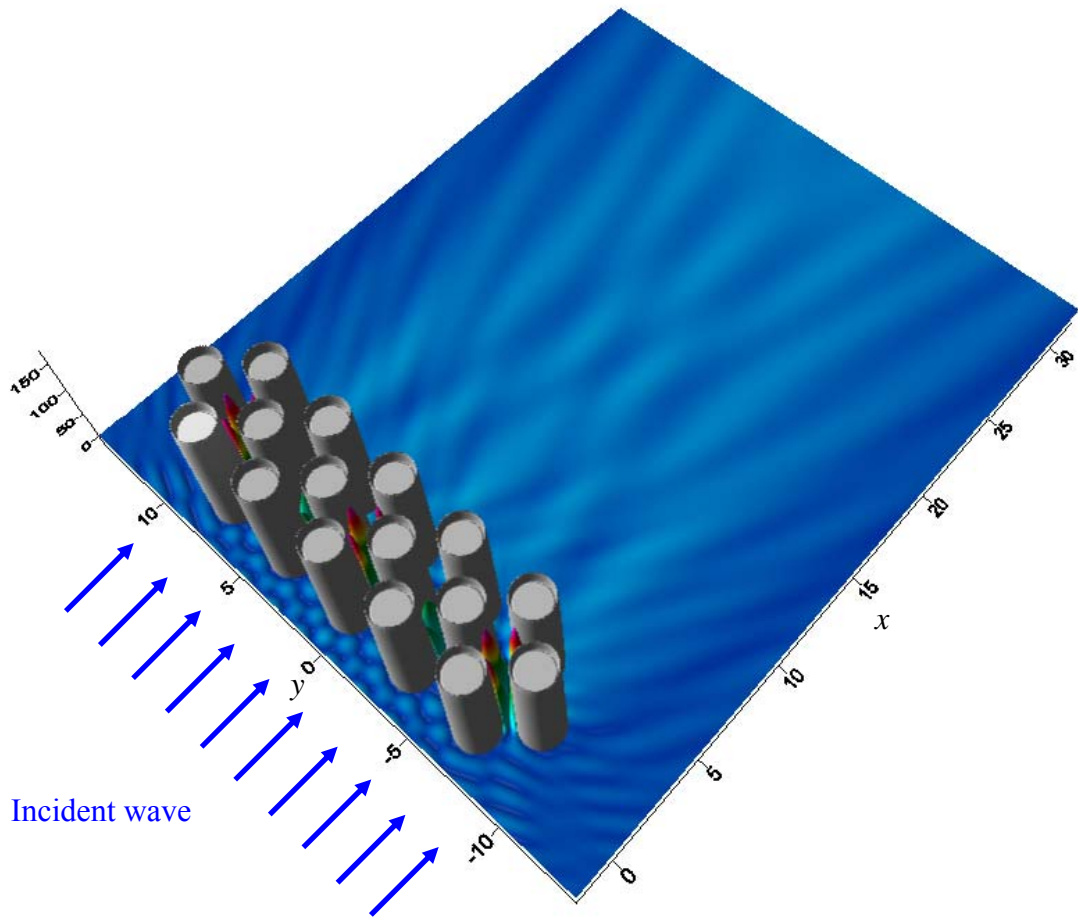
Figure 3-10 Near-trapped mode for the ordered pile array at $ka=2.92921$ ($a/b=0.8$, $G=0.0$, $M=20$, $\tau = 0.0$, $H = 2$)



(a) Contour plot by Duclos and Clément [20]

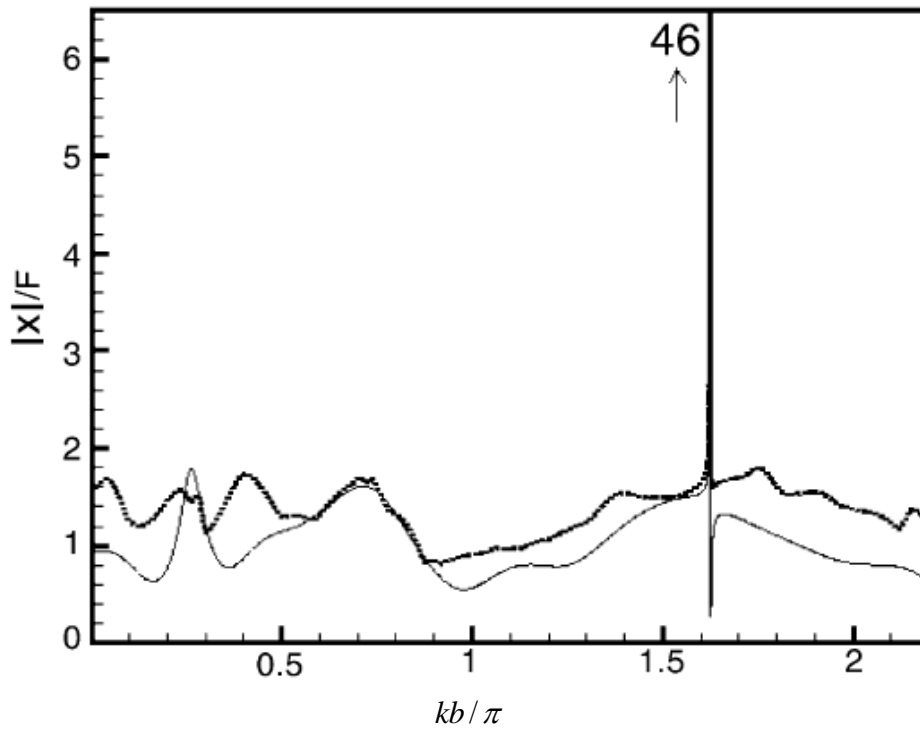


(b) Contour plot by the present method ($M=20$)

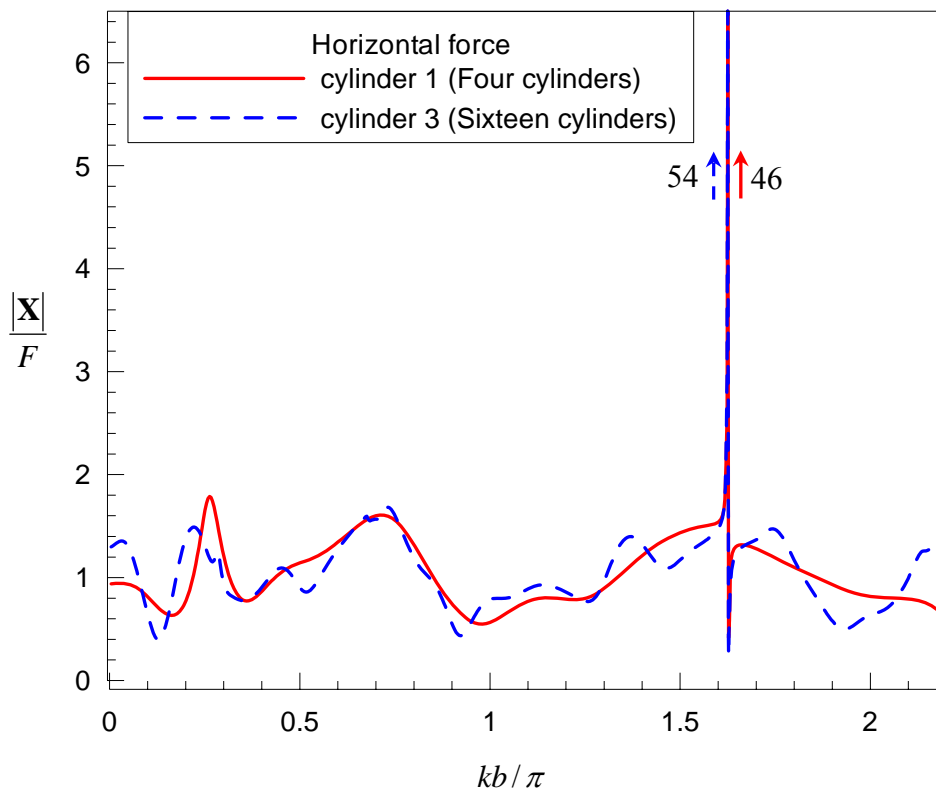


(c) Free-surface elevations by the present method ($M=20$)

Figure 3-11 Near-trapped mode for the ordered pile array at $ka=4.08482$ ($a/b=0.8$, $G=0.0$, $M=20$, $\tau=0.0$, $H=2$)

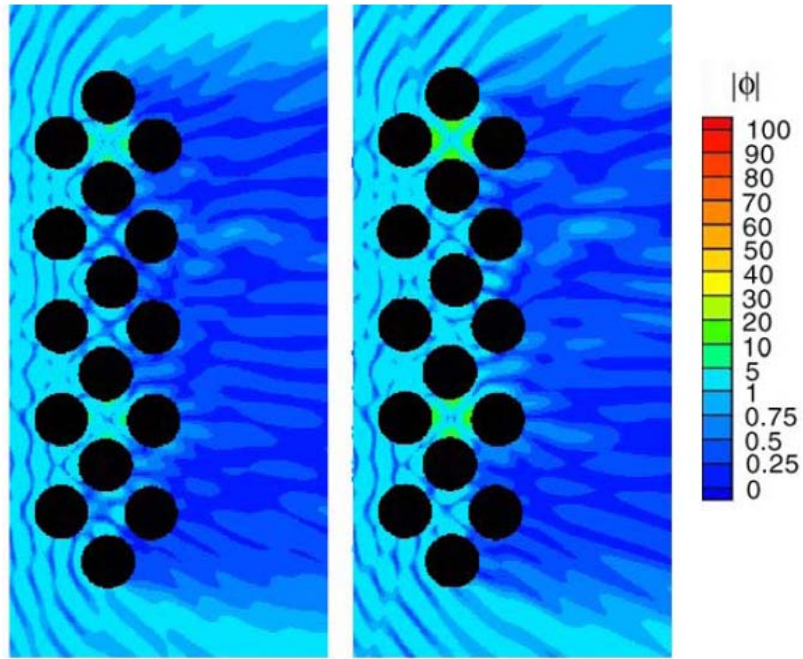


(a) Duclos and Clément [20]



(b) Present method ($M=20$)

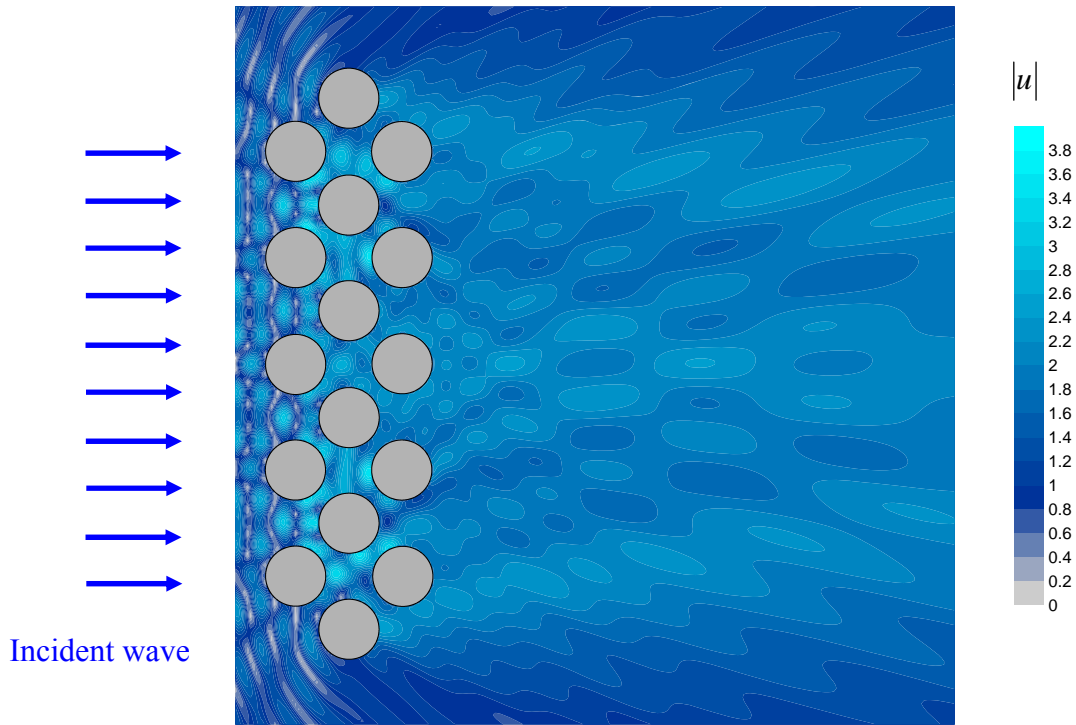
Figure 3-12 Horizontal force on the corresponding cylinder of the ordered pile array
 ($kb/\pi=1.625293$, $a/b=0.8$, $M=20$, $\tau = 0.0$, $H = 2$)



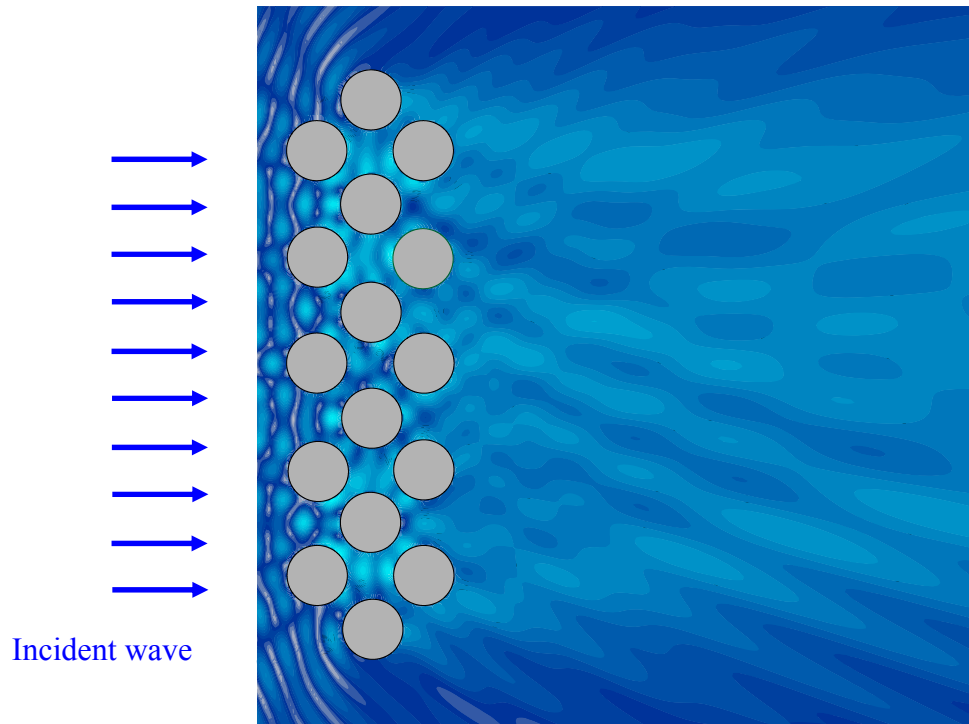
(a) Random case 1

(b) Random case 2

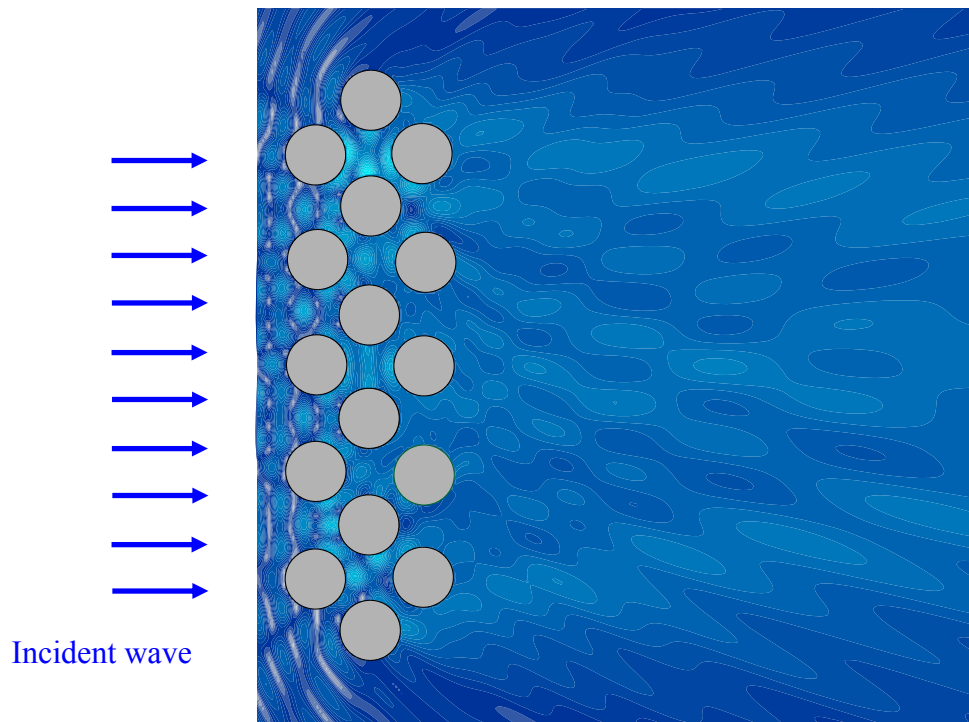
Figure 3-13 Suppression of near-trapped modes by using disorder ($\tau = 0.1, H=2$) [20]



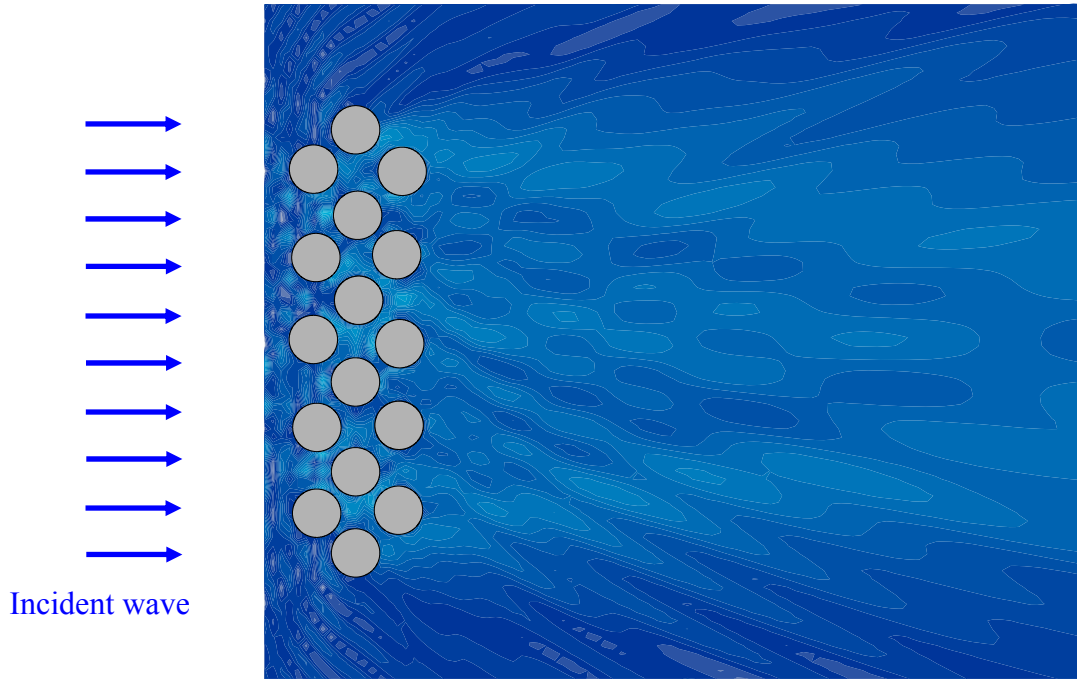
(a) displaced array ($\tau = 0.1$)



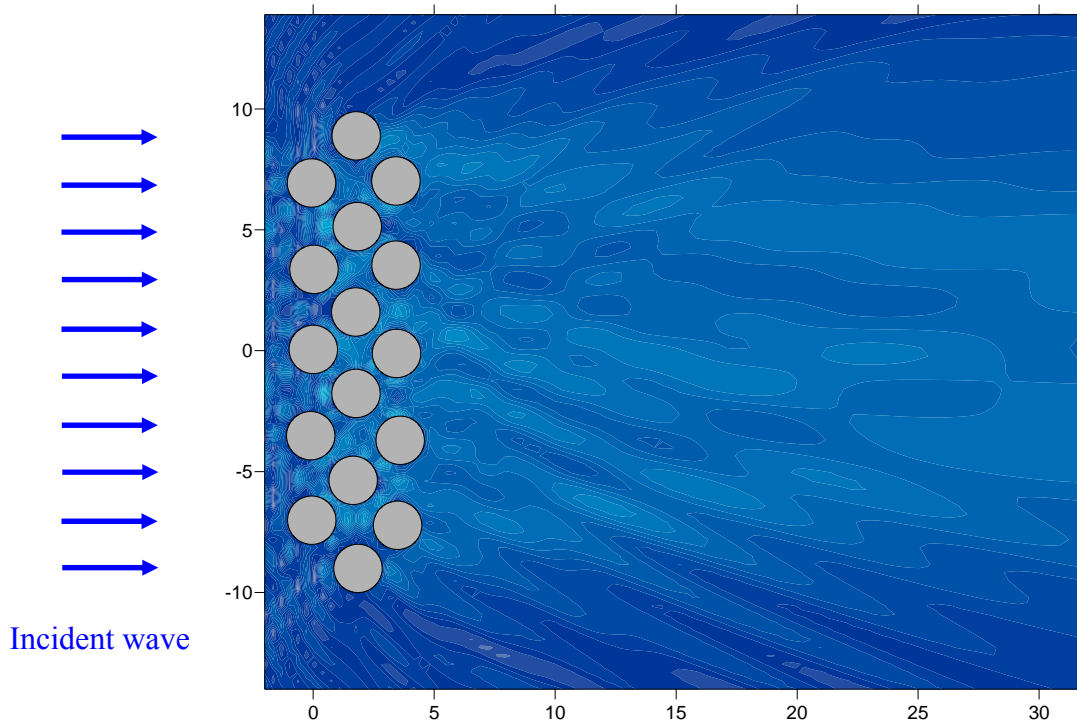
(b) displaced array ($\tau = 0.3$)



(c) displaced array ($\tau = 0.5$)

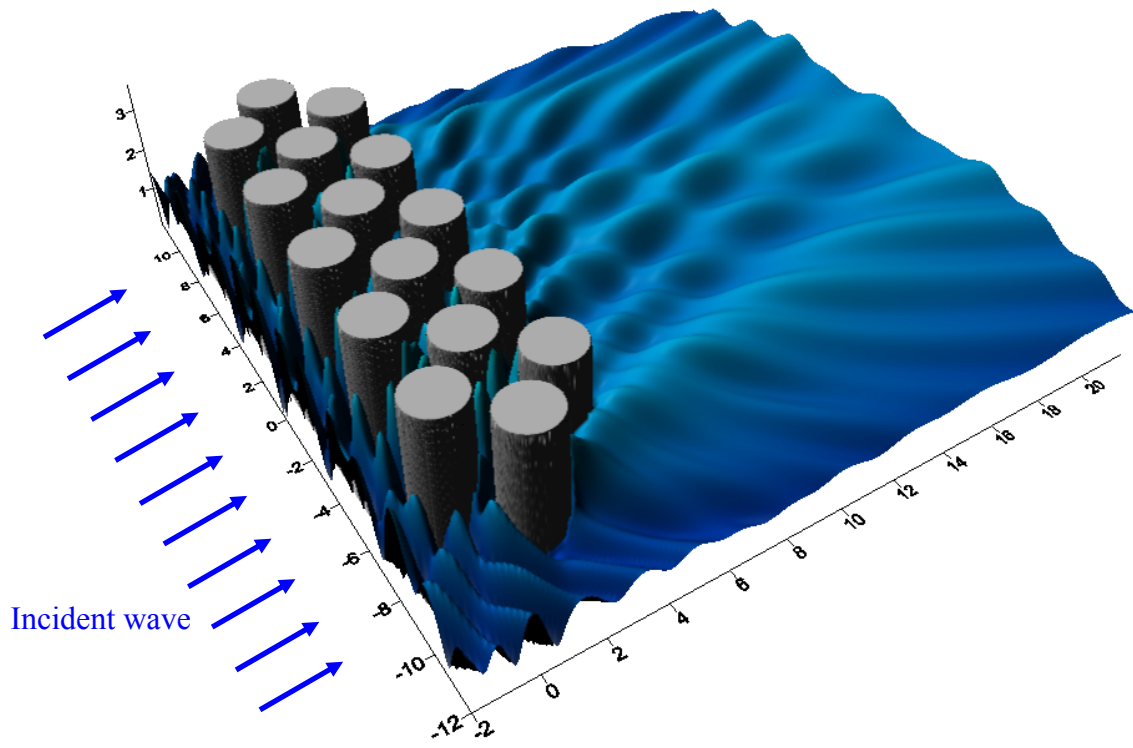


(d) displaced array ($\tau = 0.7$)

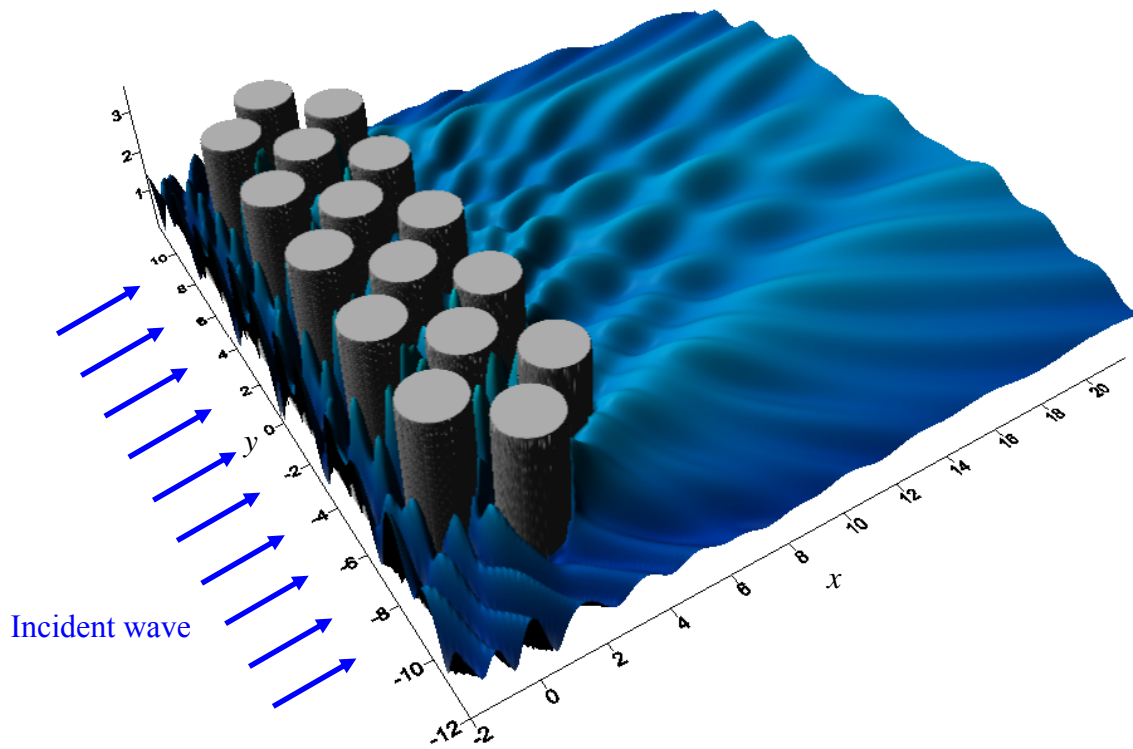


(e) displaced array ($\tau = 0.9$)

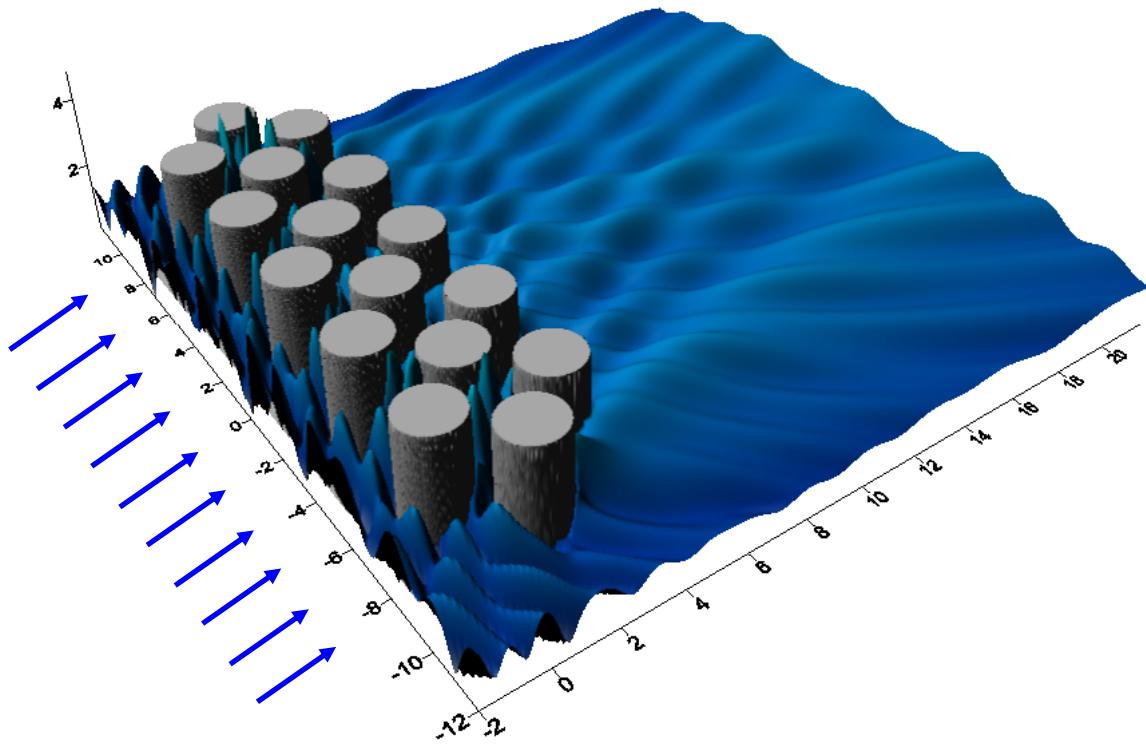
Figure 3-14 Suppression of near-trapped modes by using disorder ($a/b=0.8$, $M=20$, $H = 2$)



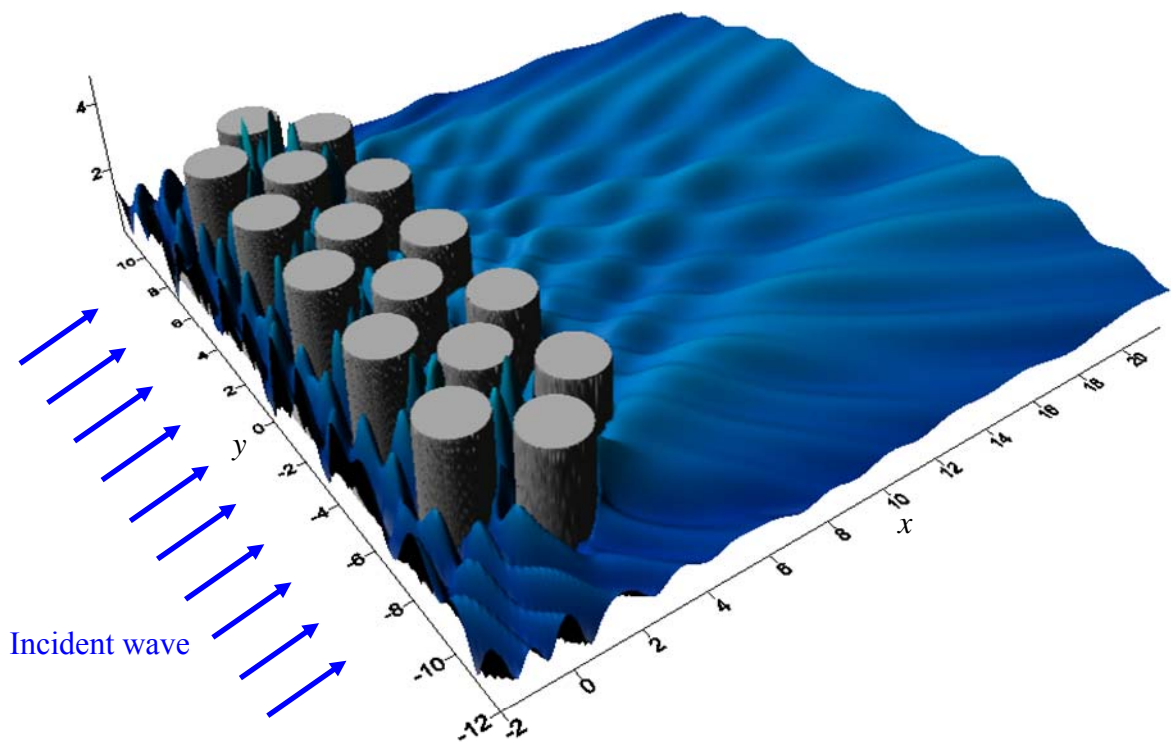
(a) displaced array ($\tau = 0.1$)



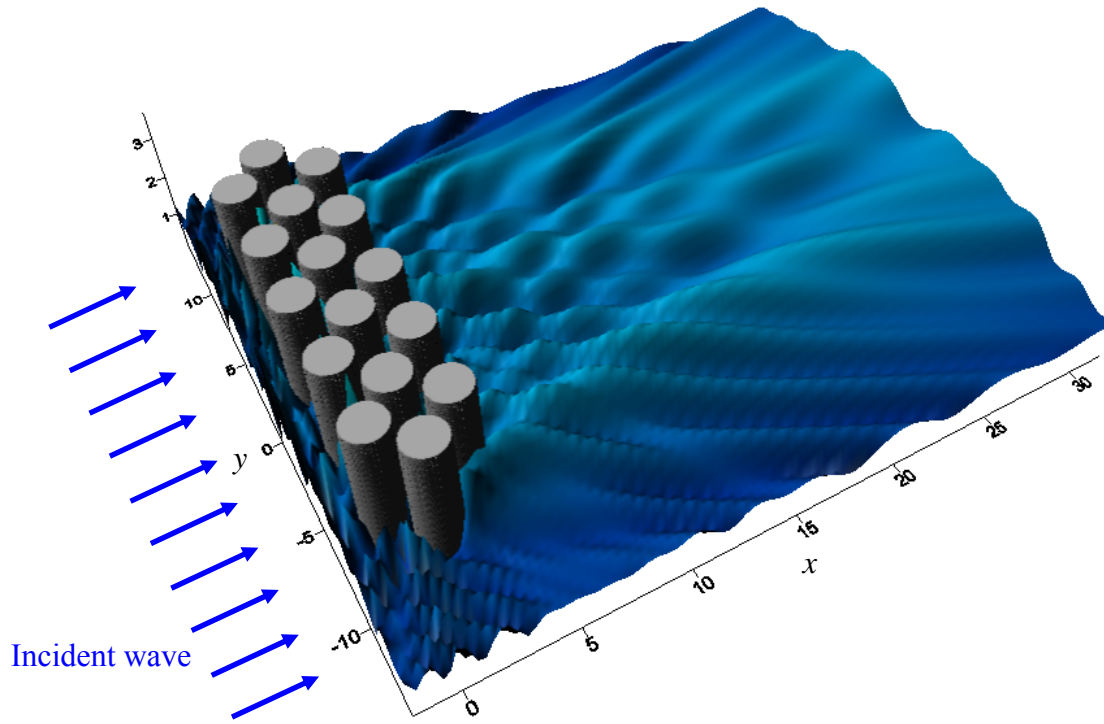
(b) displaced array ($\tau = 0.3$)



(c) displaced array ($\tau = 0.5$)

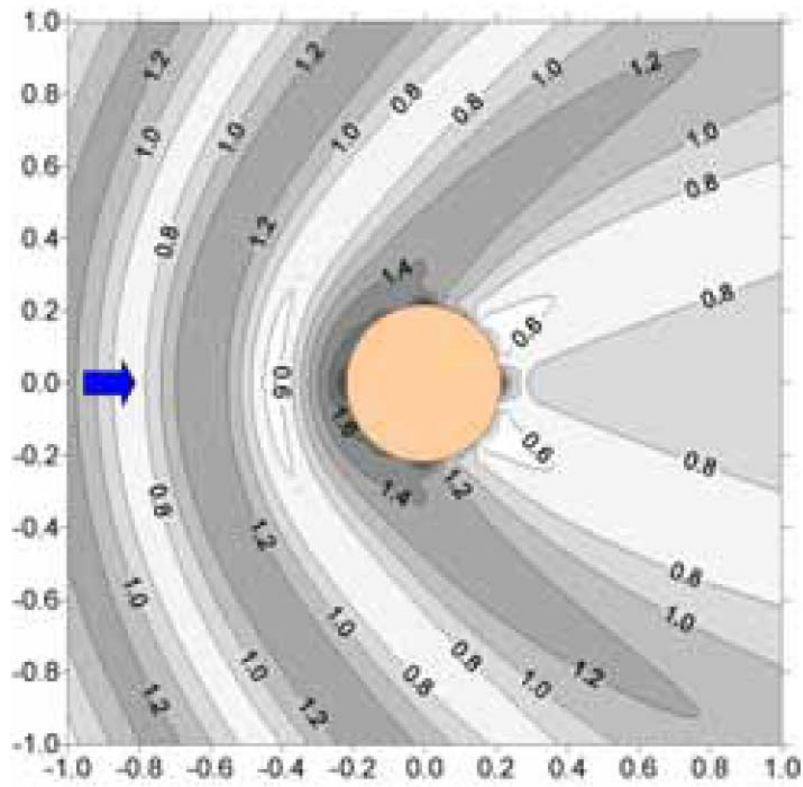


(d) displaced array ($\tau = 0.7$)

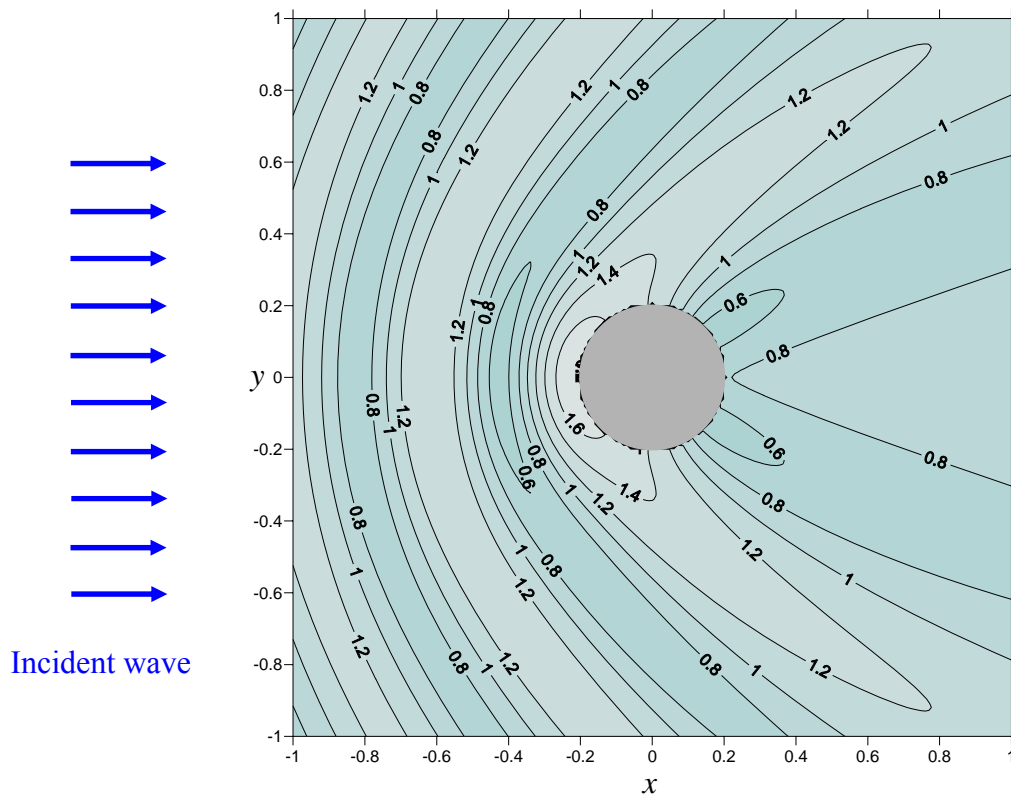


(e) displaced array ($\tau = 0.9$)

Figure 3-15 Free surface elevations for a perturbation of position ($kd / \pi = 1.625293$, $a/b=0.8$, $M=20$, $H = 2$)



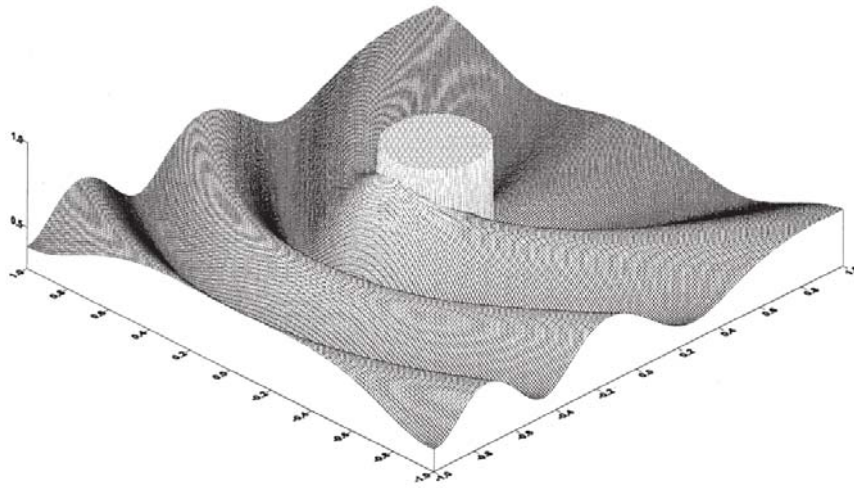
(a) BEM [5]



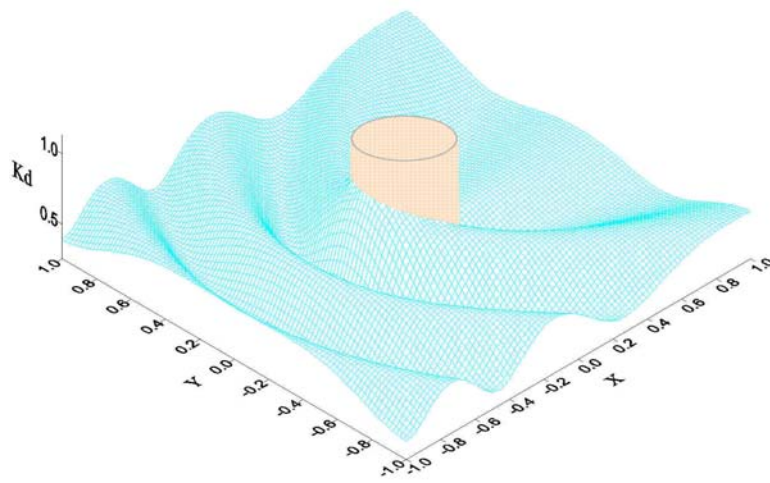
(b) Null field BIEM ($M=20$)

Figure 3-16 Contour plots of free-surface elevation of a single impermeable cylinder

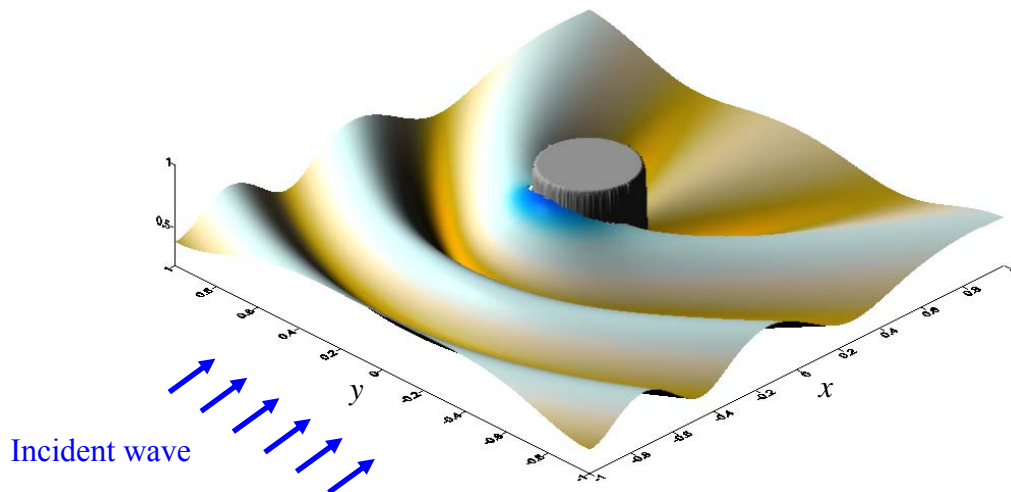
$$(G=0.0, \theta_{inc} = 0^\circ, h/a = 5 \text{ and } ka = \frac{\pi}{2}, H = 2)$$



(a) Linton and Evan approach [51]



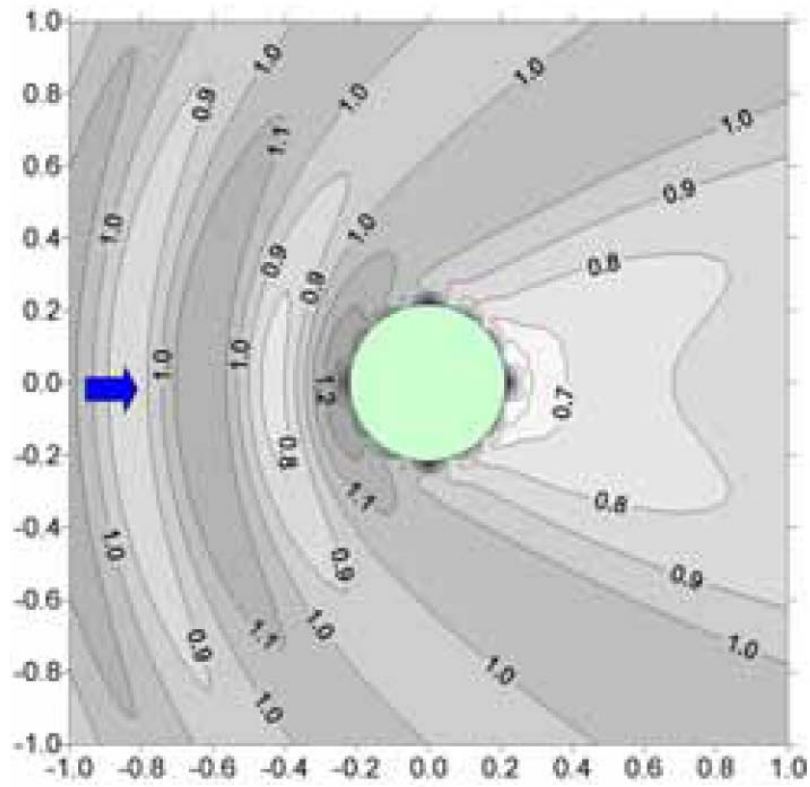
(b) BEM [5]



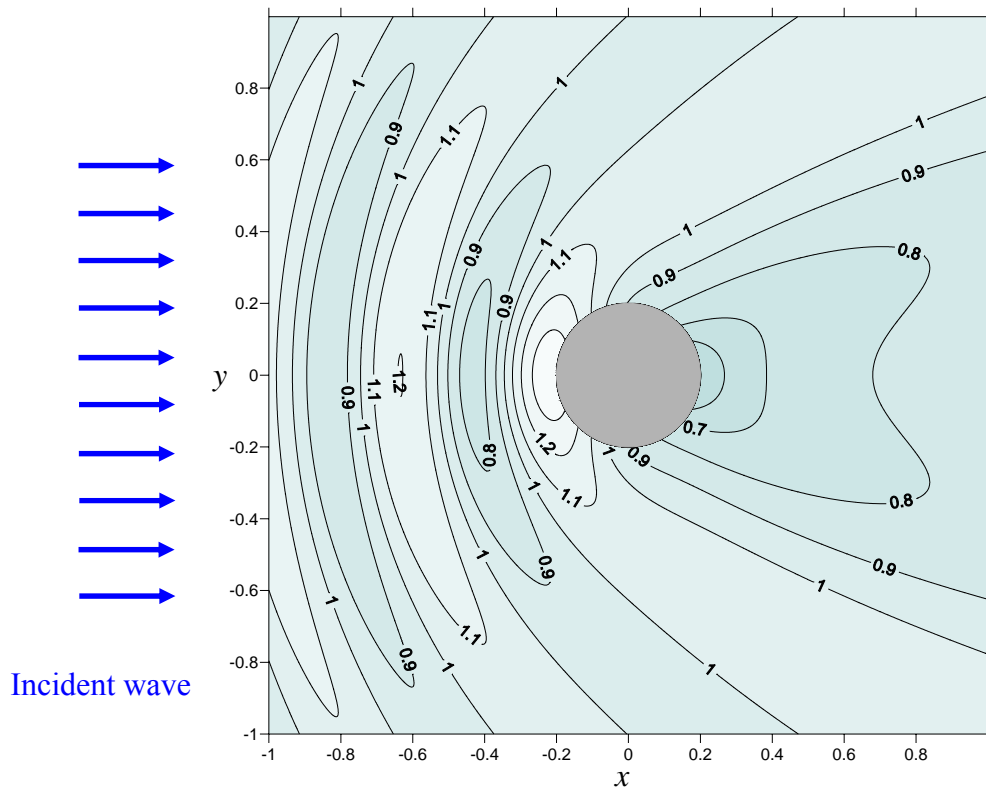
(c) Null field BIEM ($M=20$)

Figure 3-17 Free-surface elevation of the single impermeable cylinder

$$(G=0.0, \theta_{inc} = 0^\circ, h/a = 5, ka = \frac{\pi}{2}, H = 1)$$



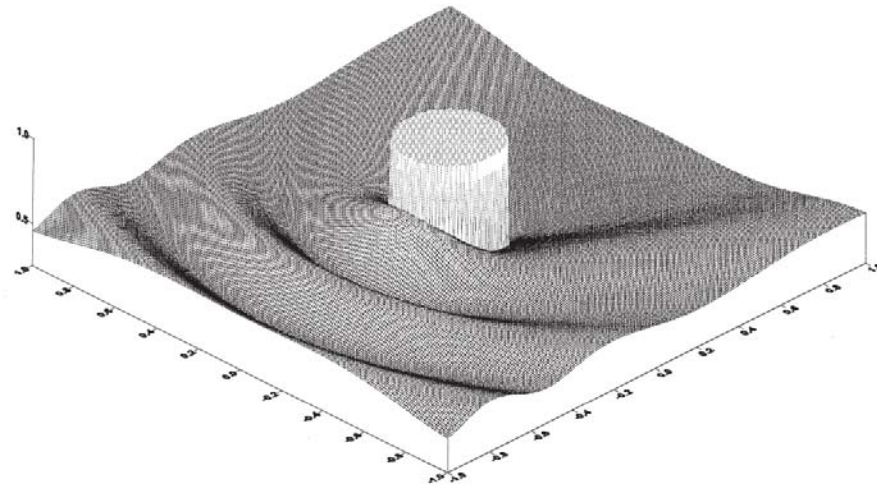
(a) BEM [5]



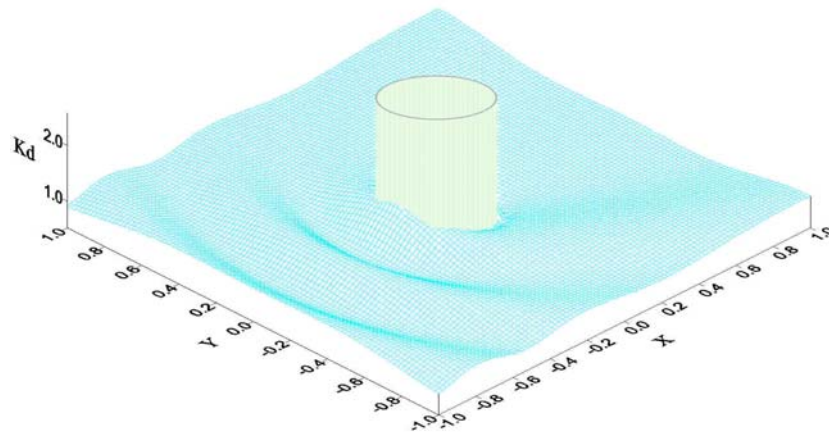
(b) Null-field BIEM ($M=20$)

Figure 3-18 Contour plots of free-surface elevation of a single porous cylinder

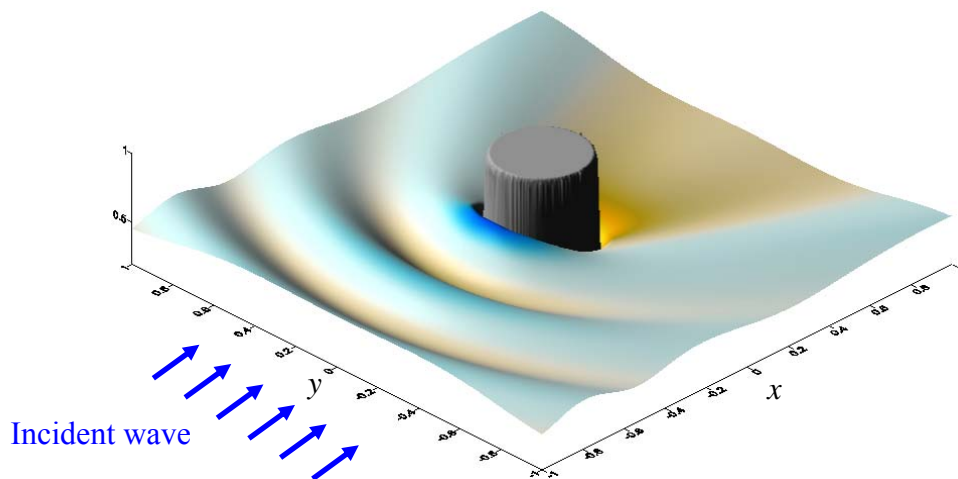
$$(G=1.0, \theta_{inc} = 0^\circ, h/a = 5 \text{ and } ka = \frac{\pi}{2}, H = 2)$$



(a) Linton and Evan approach [51]



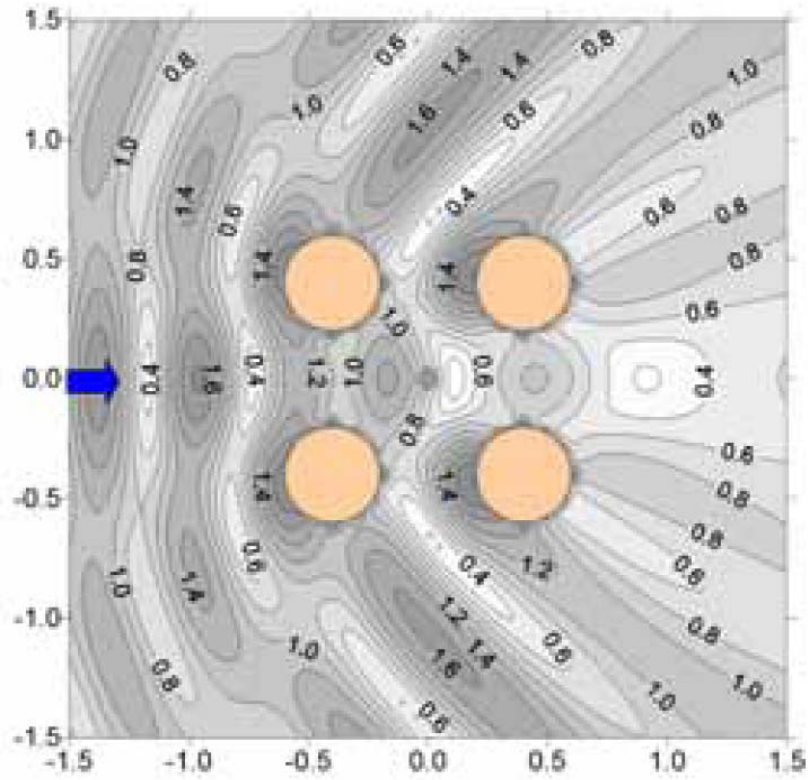
(b) BEM [5]



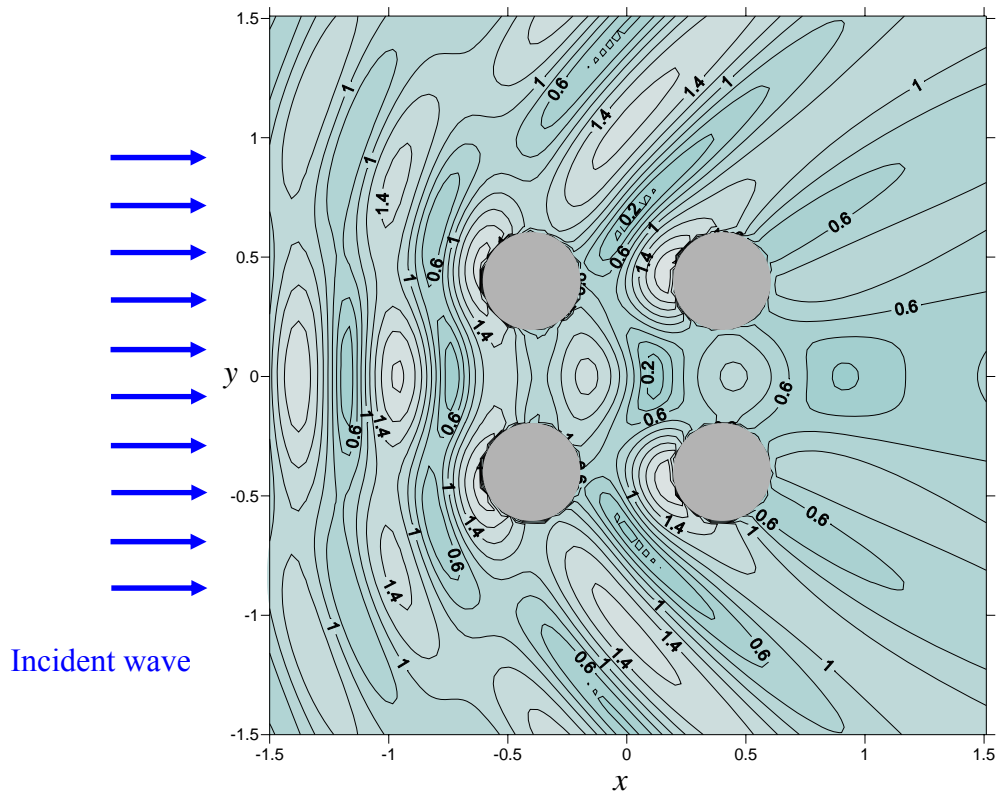
(c) Null-field BIEM ($M=20$)

Figure 3-19 Free-surface elevation of a single porous cylinder

$$(G=1.0, \theta_{inc} = 0^\circ, h/a = 5 \text{ and } ka = \frac{\pi}{2}, H = 1)$$



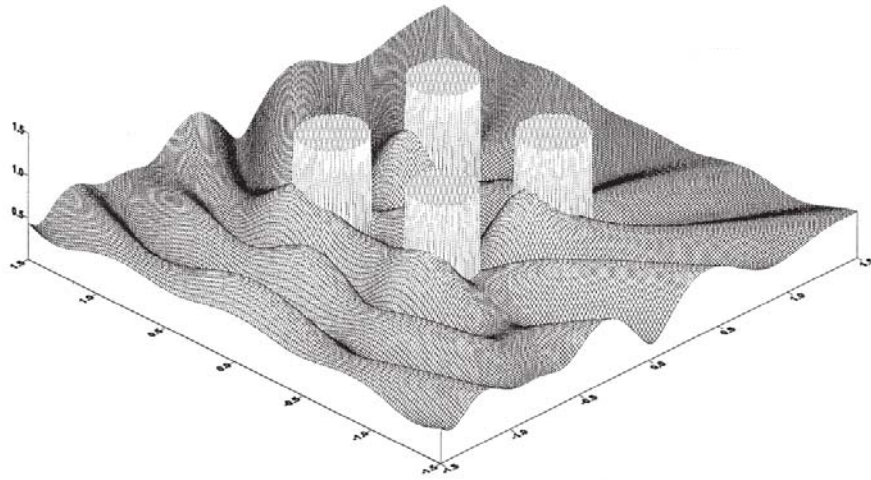
(a) BEM [5]



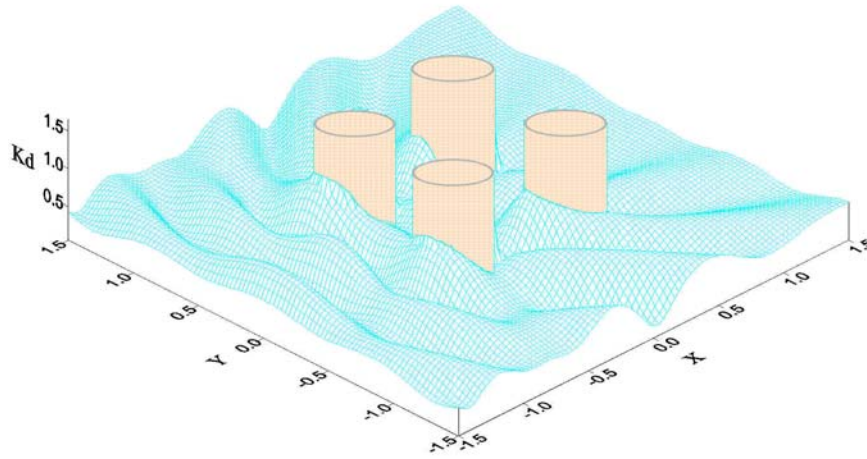
(b) Null-field BIEM ($M=20$)

Figure 3-20 Contour plots of free-surface elevation of the four impermeable cylinders

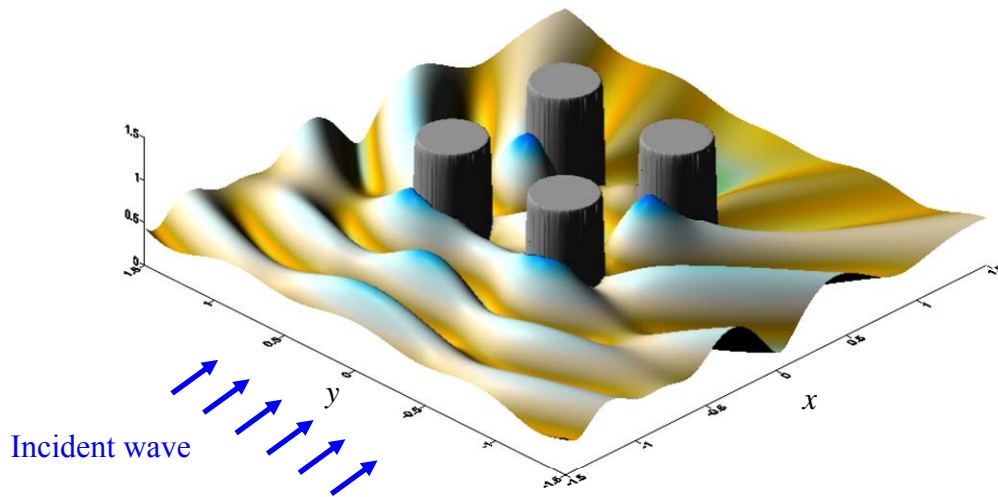
$$(G=0.0, \theta_{inc} = 0^\circ, h/a = 5, 2b/a = 4 \text{ and } ka = \frac{\pi}{2}, H = 2)$$



(a) Linton and Evan approach [51]



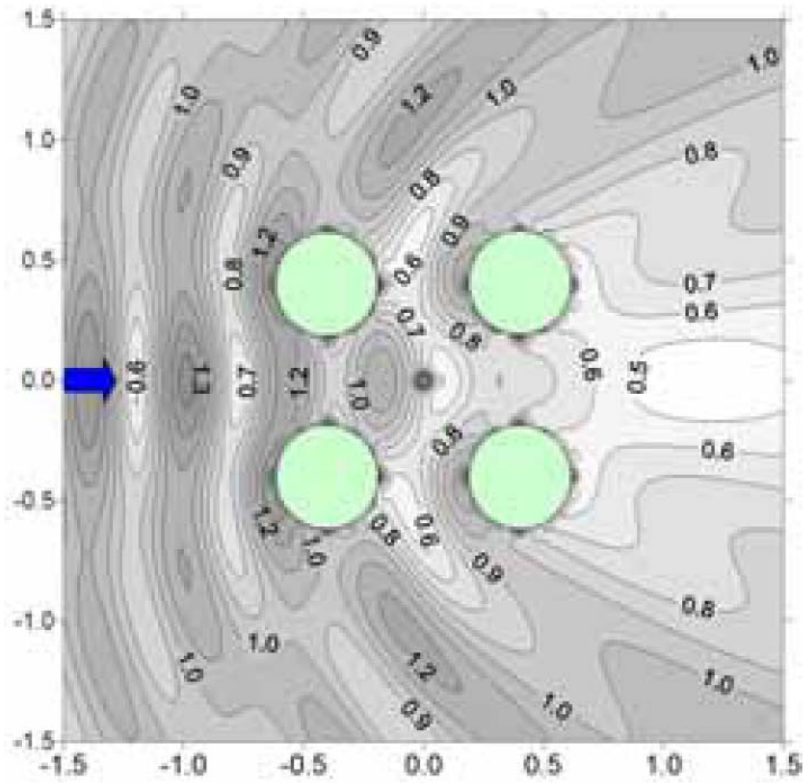
(b) BEM [5]



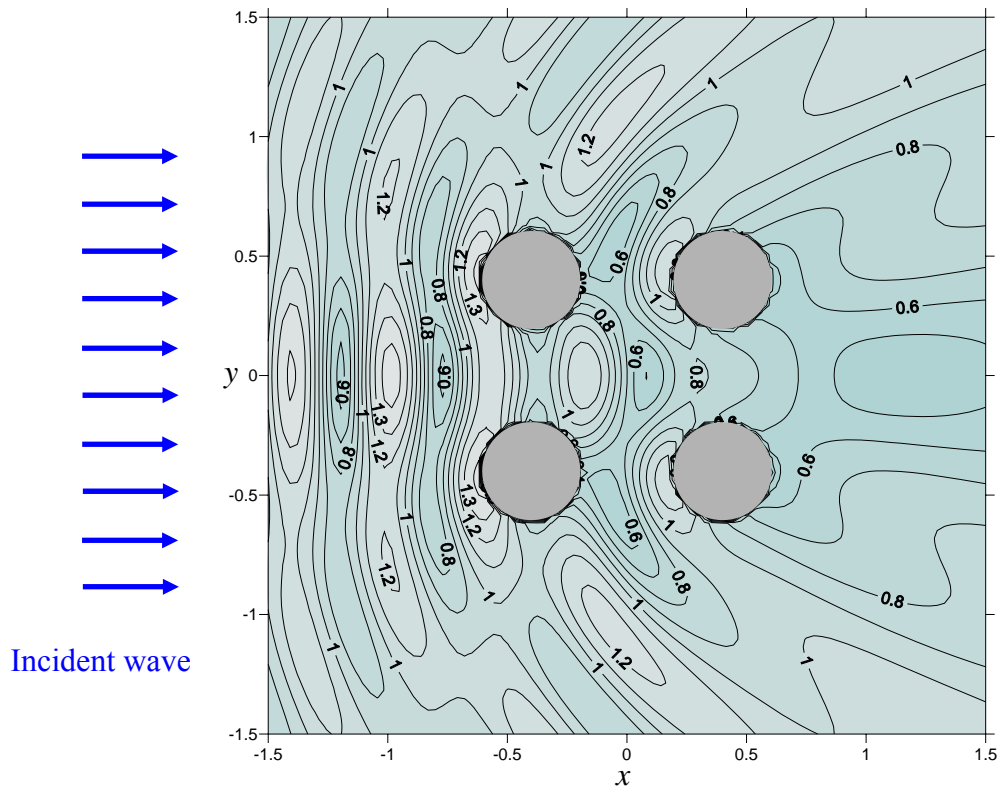
(c) Null-field BIEM ($M=20$)

Figure 3-21 Free-surface elevation of the arrays of four impermeable cylinders arrays.

$$(G=0.0, \theta_{mc} = 0^\circ, h/a = 5, 2b/a = 4 \text{ and } ka = \frac{\pi}{2}, H = 1)$$



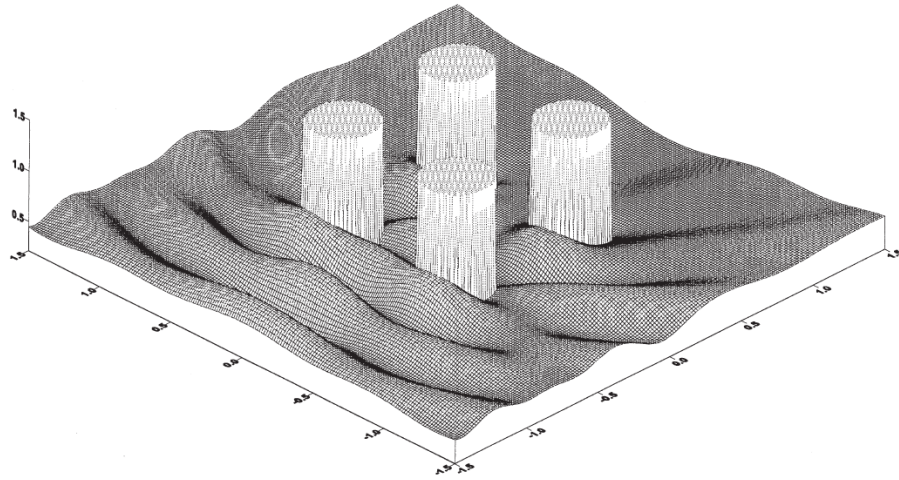
(a) BEM [5]



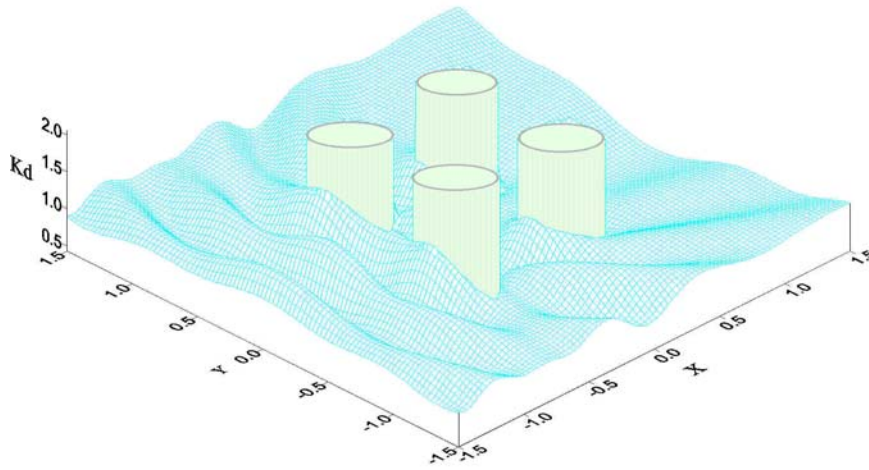
(b) Null-field BIEM ($M=20$)

Figure 3-22 Contour plots of free-surface elevation of the four porous cylinders.

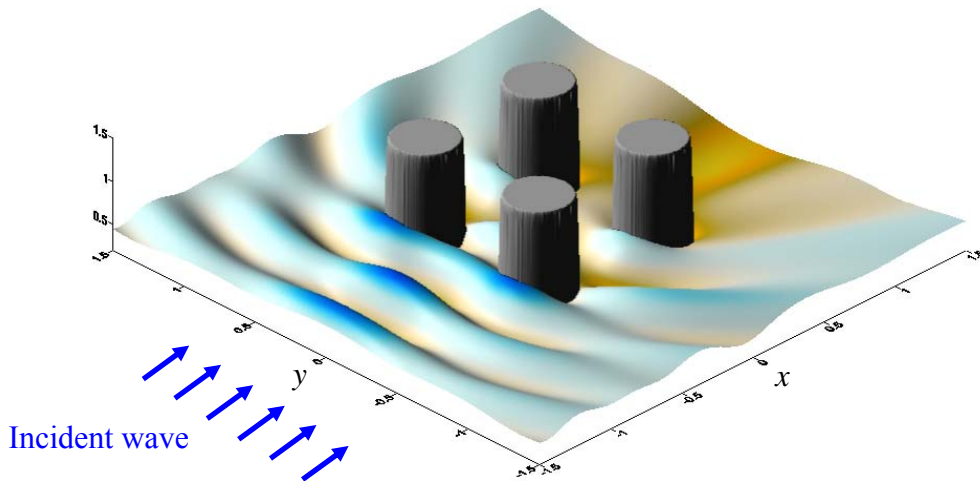
$$(G=1.0, \theta_{inc} = 0^\circ, h/a = 5, 2b/a = 4 \text{ and } ka = \frac{\pi}{2}, H = 2)$$



(a) Linton and Evan approach [51]



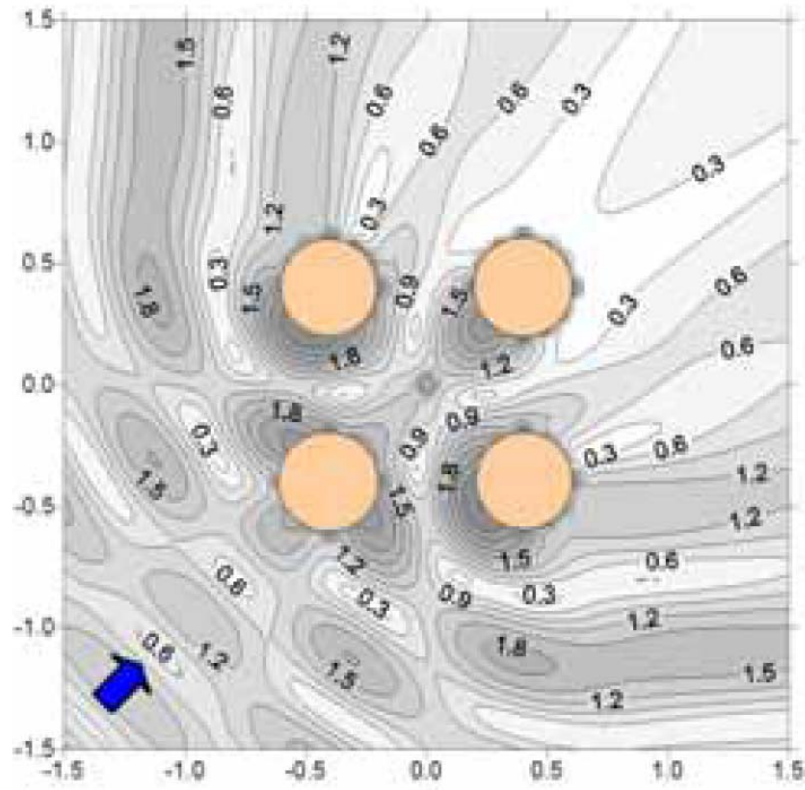
(b) BEM [5]



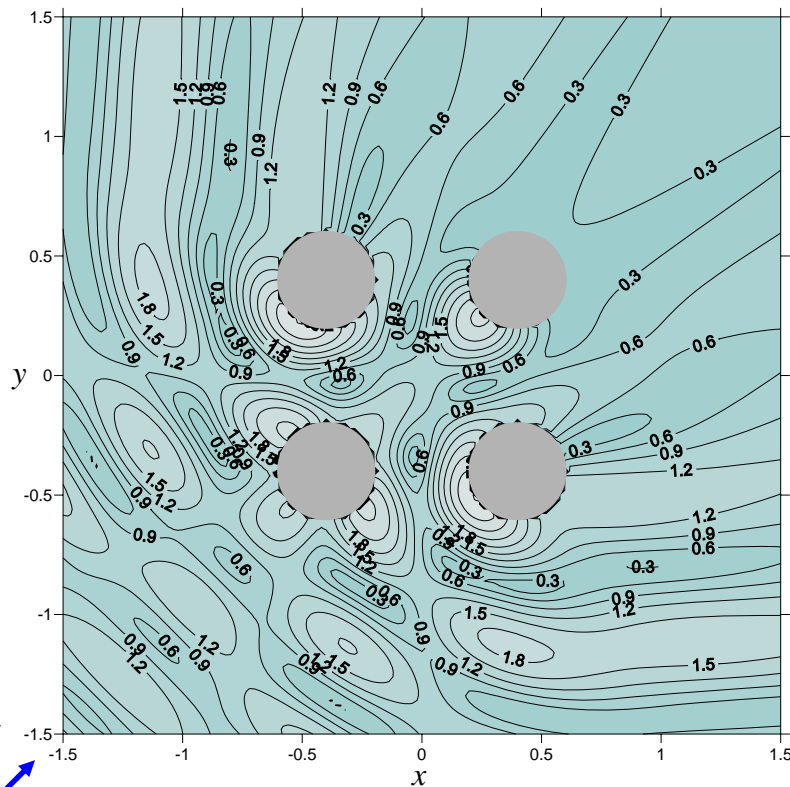
(c) Null-field BIEM ($M=20$)

Figure 3-23 Free-surface elevation of the arrays of four porous cylinders.

$$(G=1.0, \theta_{inc} = 0^\circ, h/a = 5, 2b/a = 4 \text{ and } ka = \frac{\pi}{2}, H = 1)$$



(a) BEM [5]

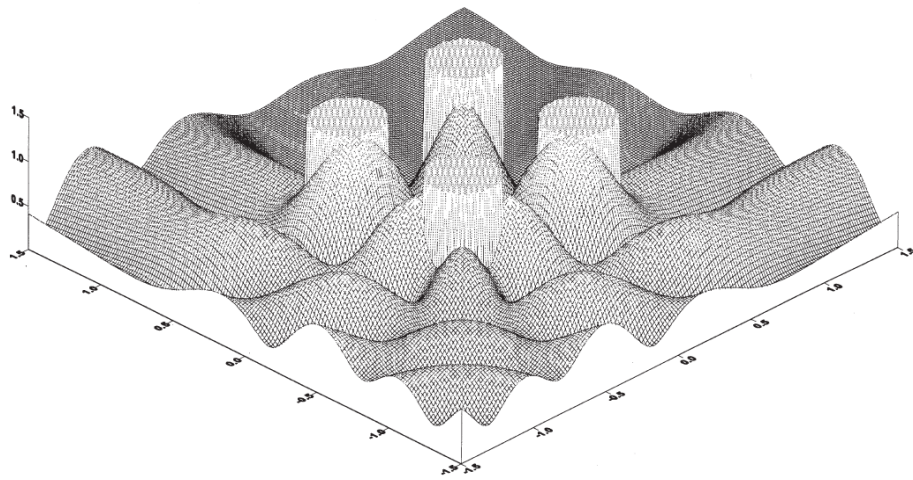


Incident wave

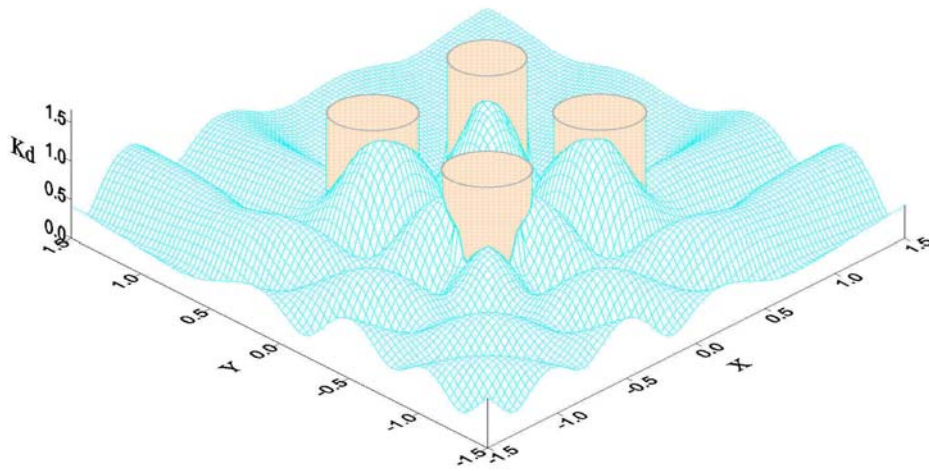
(b) Null-field BIEM ($M=20$)

Figure 3-24 Contour plots of free-surface elevation of the four impermeable cylinders.

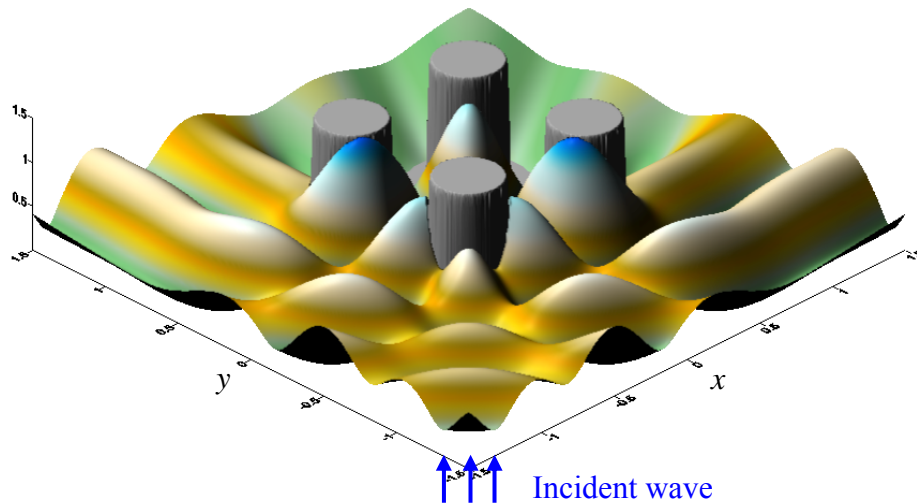
$$(G=0.0, \theta_{inc} = 45^\circ, h/a = 5, 2b/a = 4 \text{ and } ka = \frac{\pi}{2}, H = 2)$$



(a) Linton and Evan approach [51]



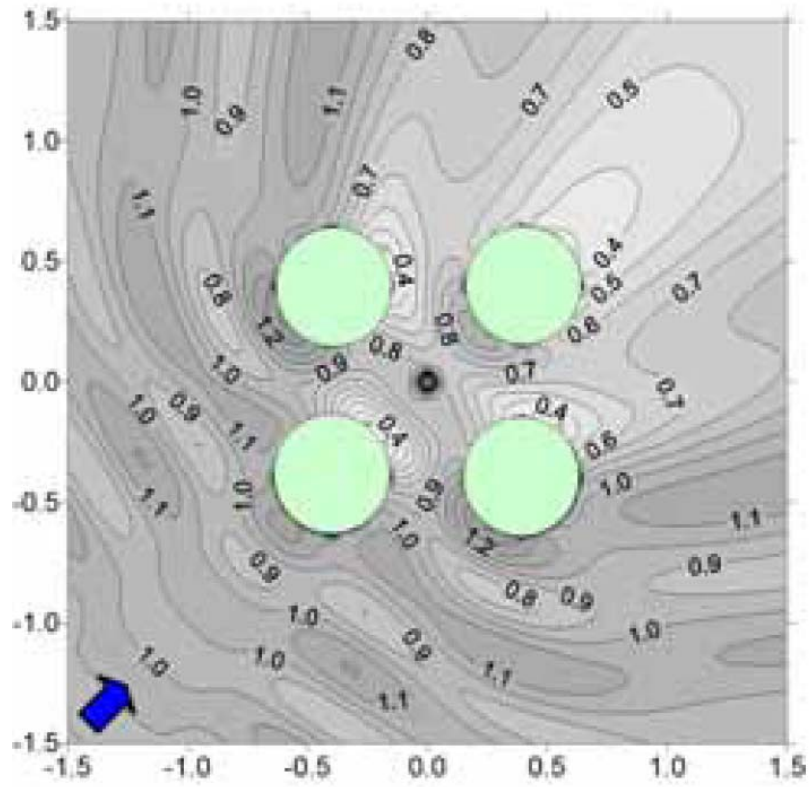
(b) BEM [5]



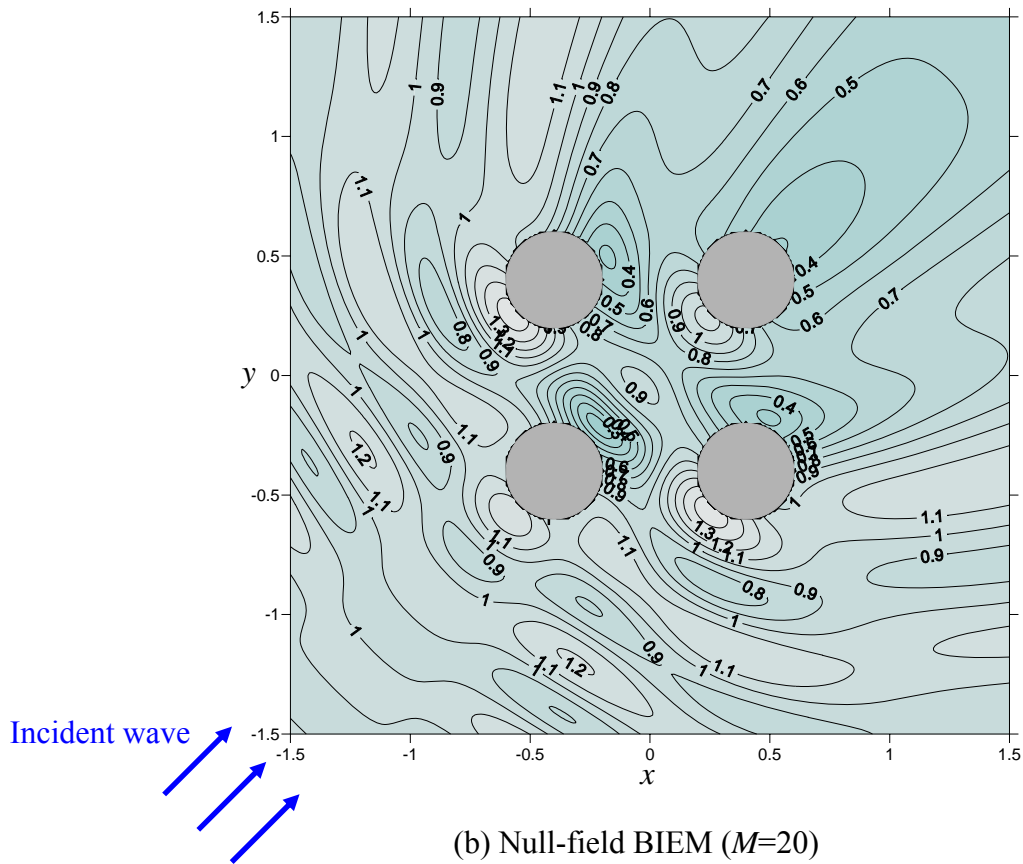
(c) Null-field BIEM ($M=20$)

Figure 3-25 Free-surface elevation of the arrays of four impermeable cylinders.

$$(G=0.0, \theta_{inc} = 45^\circ, h/a = 5, 2b/a = 4 \text{ and } ka = \frac{\pi}{2}, H = 1)$$



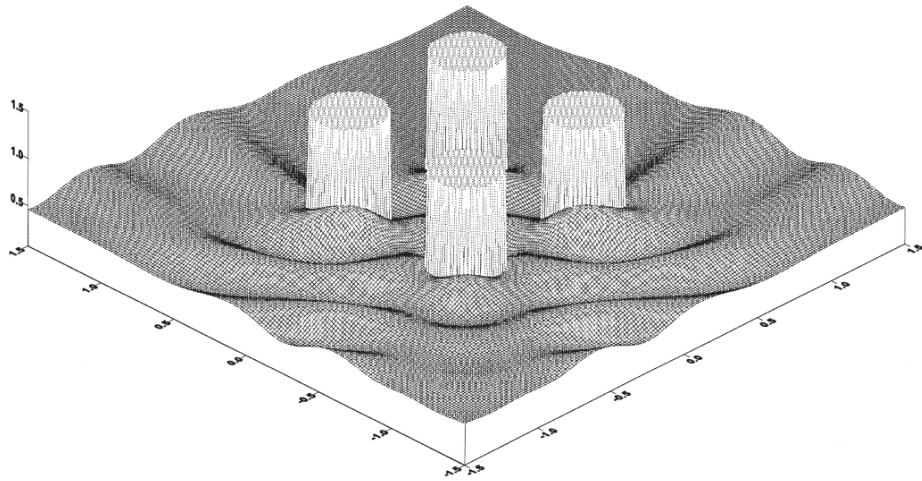
(a) BEM [5]



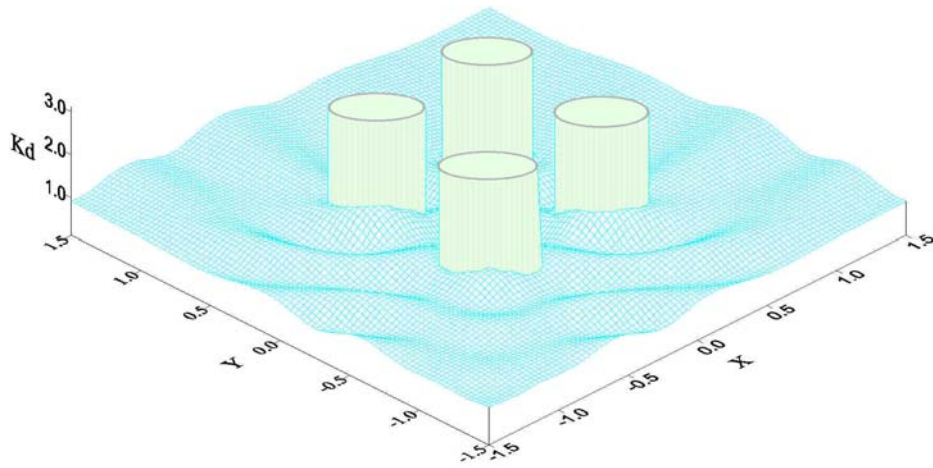
(b) Null-field BIEM ($M=20$)

Figure 3-26 Contour plots of free-surface elevation of the four porous cylinders.

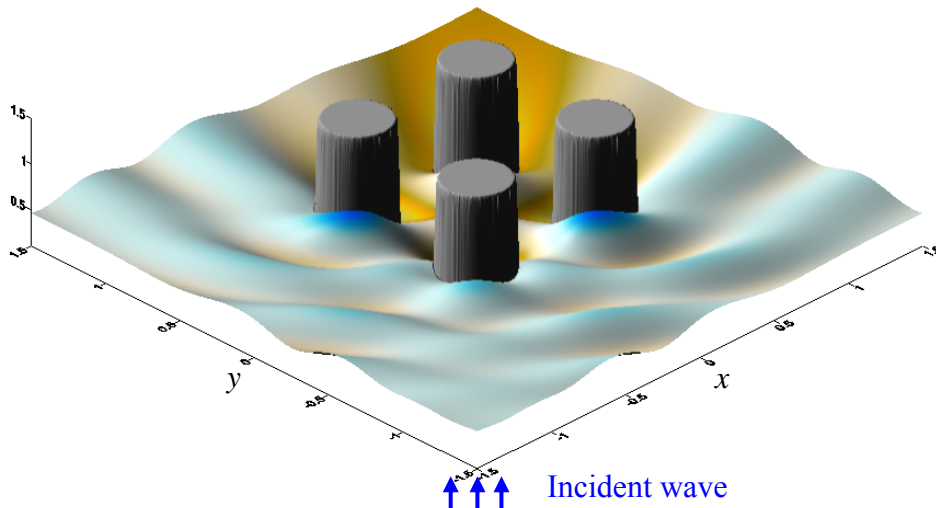
$$(G=1.0, \theta_{inc} = 45^\circ, h/a = 5, 2b/a = 4 \text{ and } ka = \frac{\pi}{2}, H = 2)$$



(a) Linton and Evan approach [51]



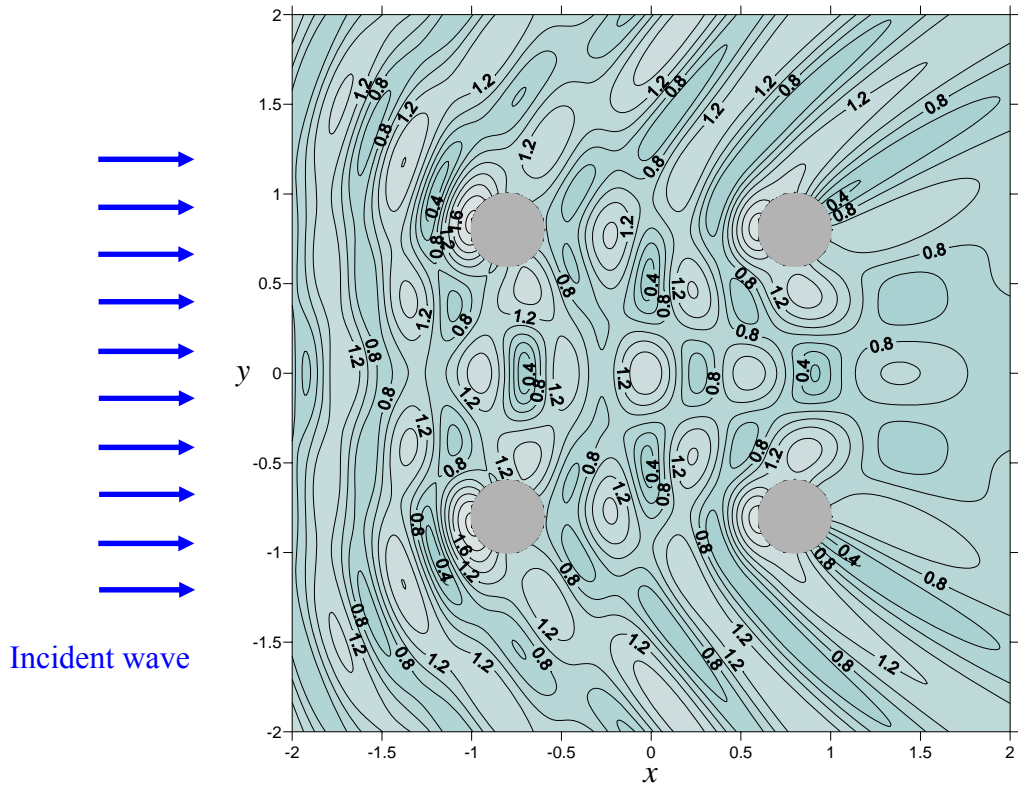
(b) BEM [5]



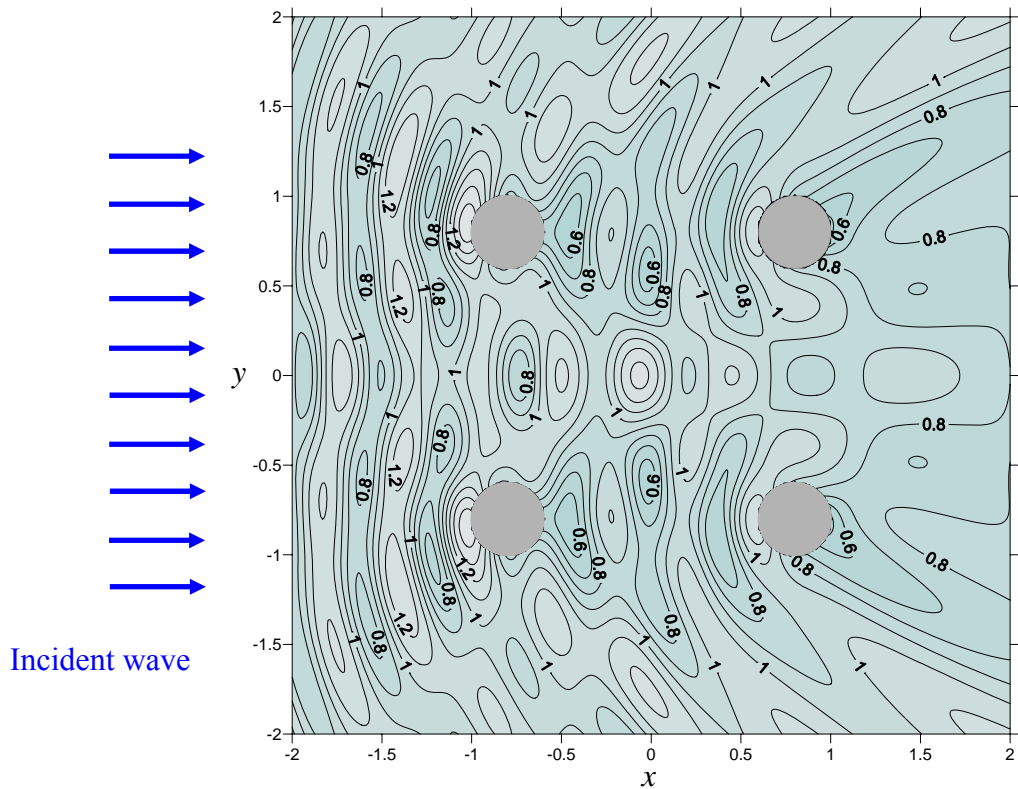
(c) Null-field BIEM ($M=20$)

Figure 3-27 Free-surface elevation of the four-cylinder array

$$(G=1.0, \theta_{inc} = 45^\circ, h/a = 5, 2b/a = 4 \text{ and } ka = \frac{\pi}{2}, H = 1)$$



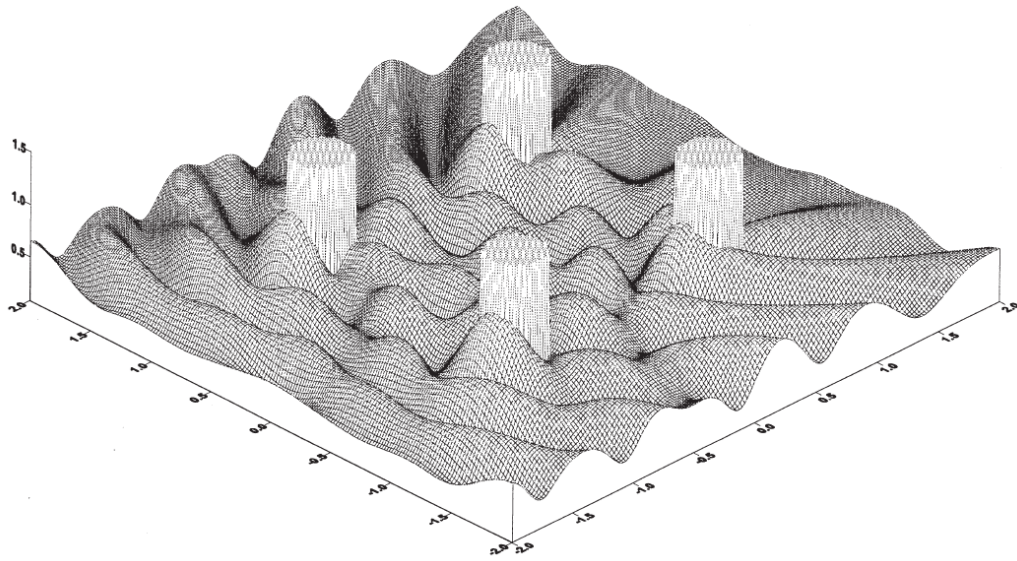
(a) Null-field BIEM ($G=0.0$, $M=20$)



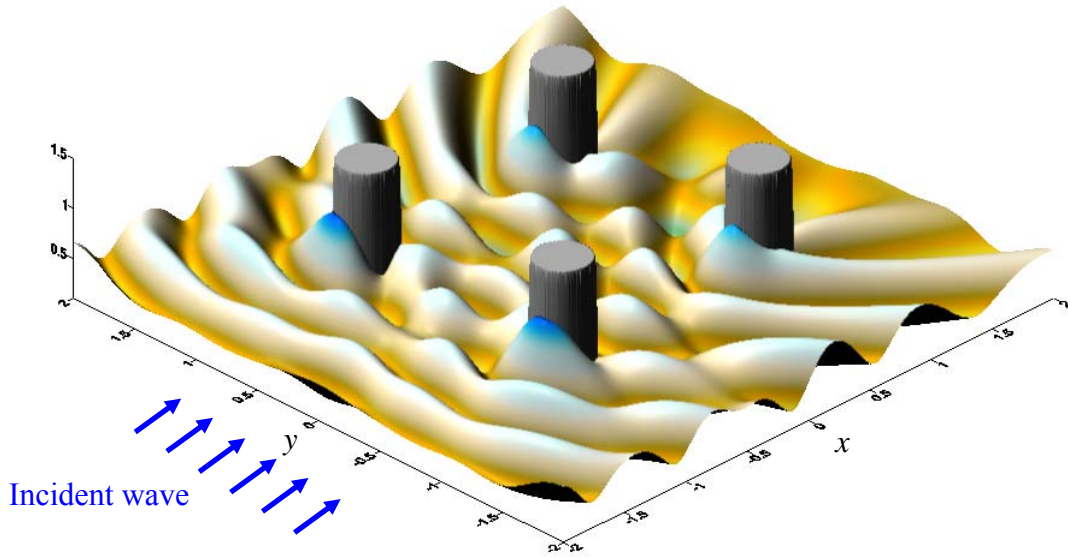
(b) Null-field BIEM ($G=1.0$, $M=20$)

Figure 3-28 Contour plots of free-surface elevation of the four cylinders

$$(\theta_{inc} = 0^\circ, h/a = 5, 2b/a = 8 \text{ and } ka = \frac{\pi}{2}, H = 2)$$



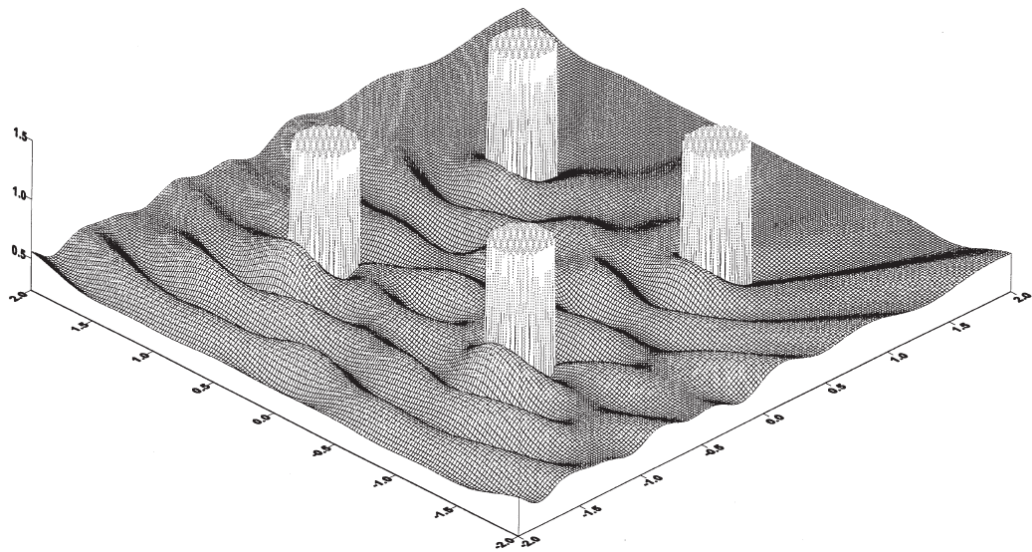
(a) Linton and Evan approach [51]



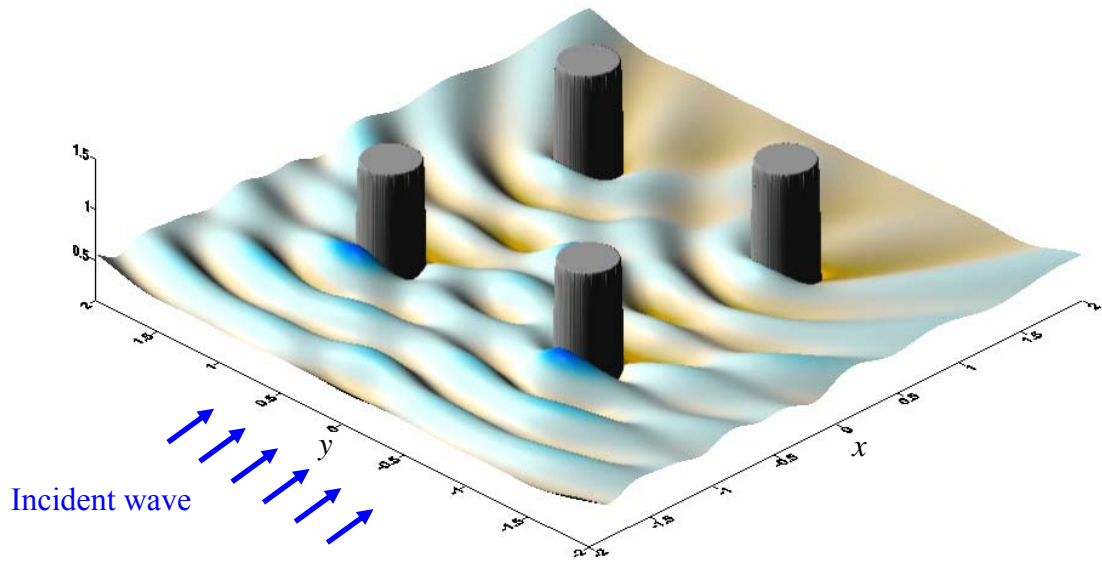
(b) Null-field BIEM ($M=20$)

Figure 3-29 Free-surface elevation of the arrays of four impermeable cylinders

$$(G=0.0, \theta_{inc} = 0^\circ, h/a = 5, 2b/a = 8 \text{ and } ka = \frac{\pi}{2}, H = 1)$$



(a) Linton and Evan approach [51]



(b) Null-field BIEM ($M=20$)

Figure 3-30 Free-surface elevation of the four porous cylinders

$$(G=1.0, \theta_{inc} = 0^\circ, h/a = 5, 2b/a = 8 \text{ and } ka = \frac{\pi}{2}, H = 1)$$

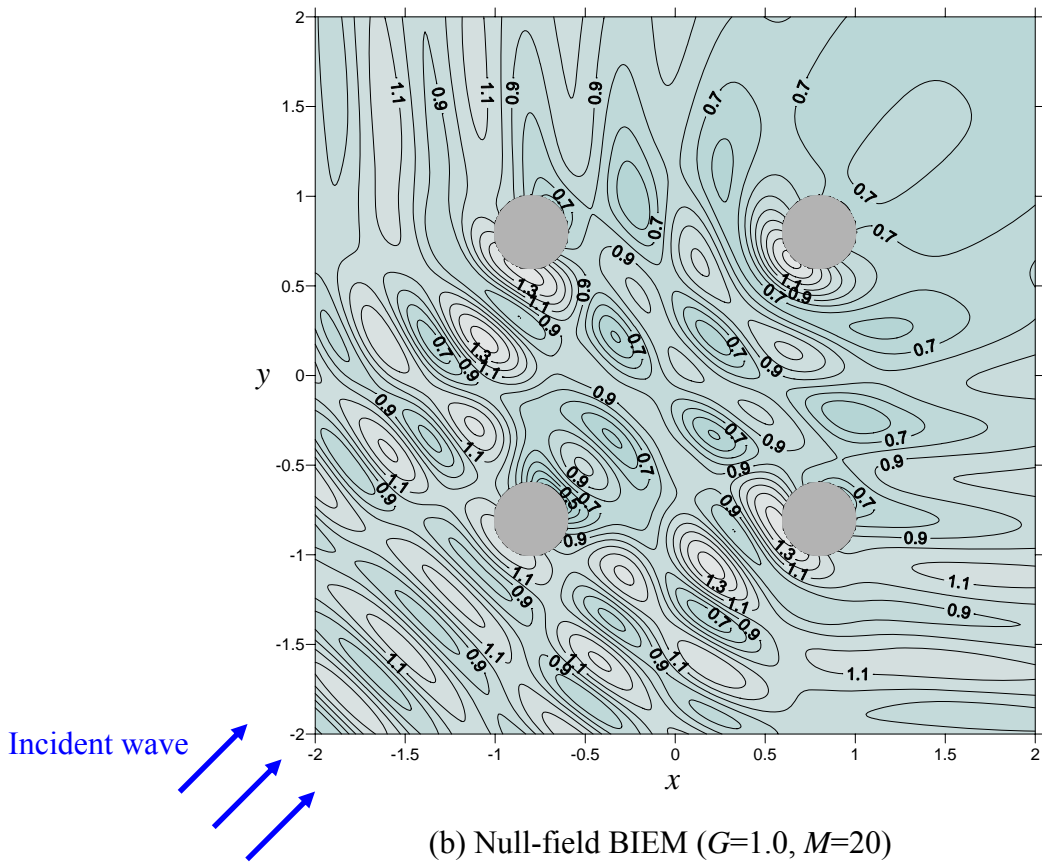
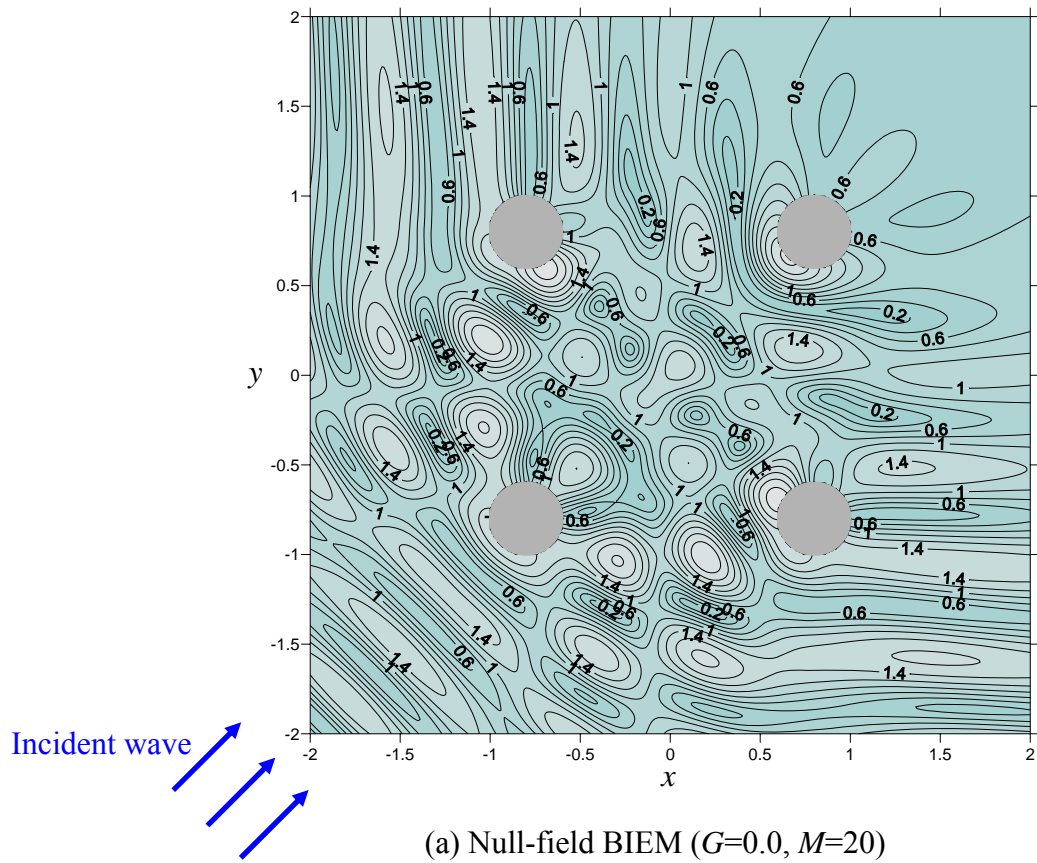
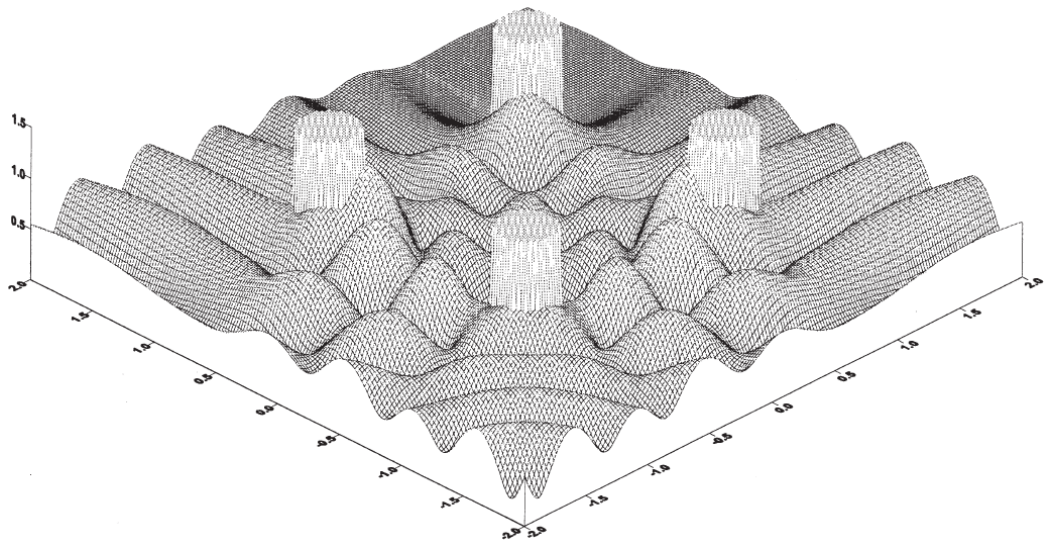
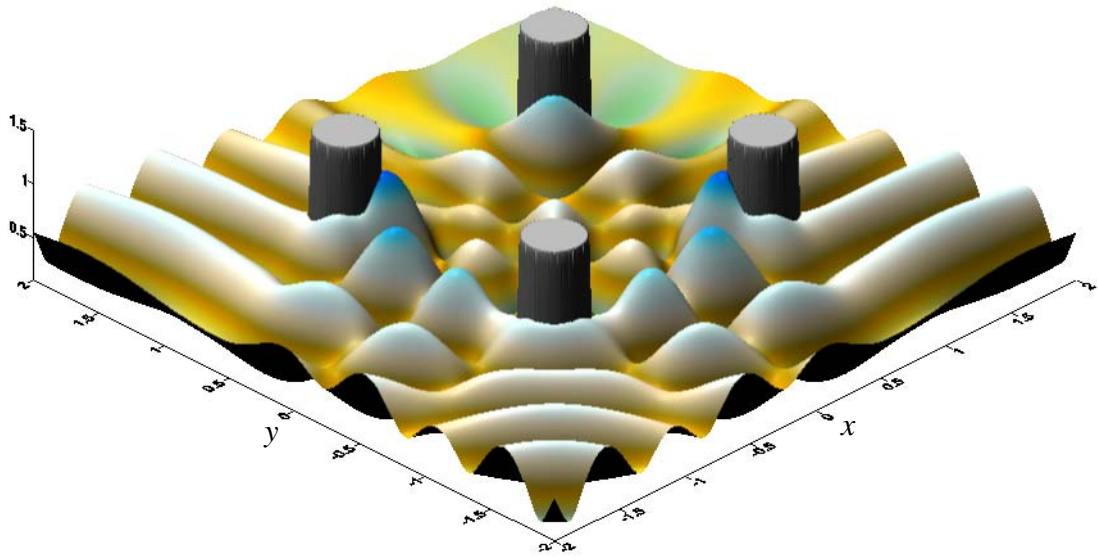


Figure 3-31 Contour plots of free-surface elevation of the four cylinders

$$(\theta_{inc} = 45^\circ, h/a = 5, 2b/a = 8 \text{ and } ka = \frac{\pi}{2}, H = 2)$$



(a) Linton and Evan approach [51]

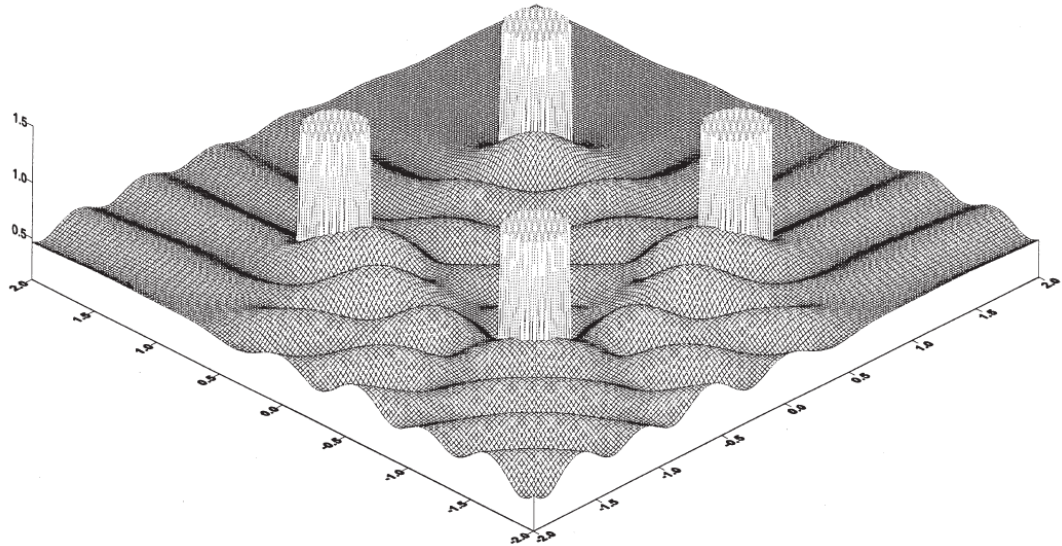


↑↑↑ Incident wave

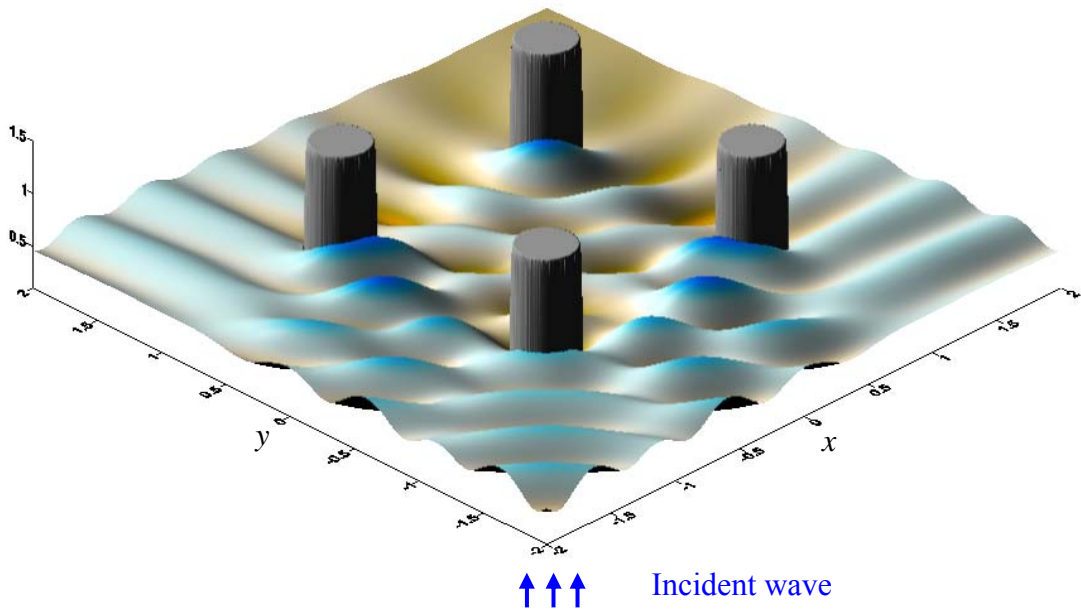
(b) Null-field BIEM ($M=20$)

Figure 3-32 Free-surface elevation of the arrays of four impermeable cylinders

$$(G=0.0, \theta_{inc} = 45^\circ, h/a = 5, 2b/a = 8 \text{ and } ka = \frac{\pi}{2}, H = 1)$$



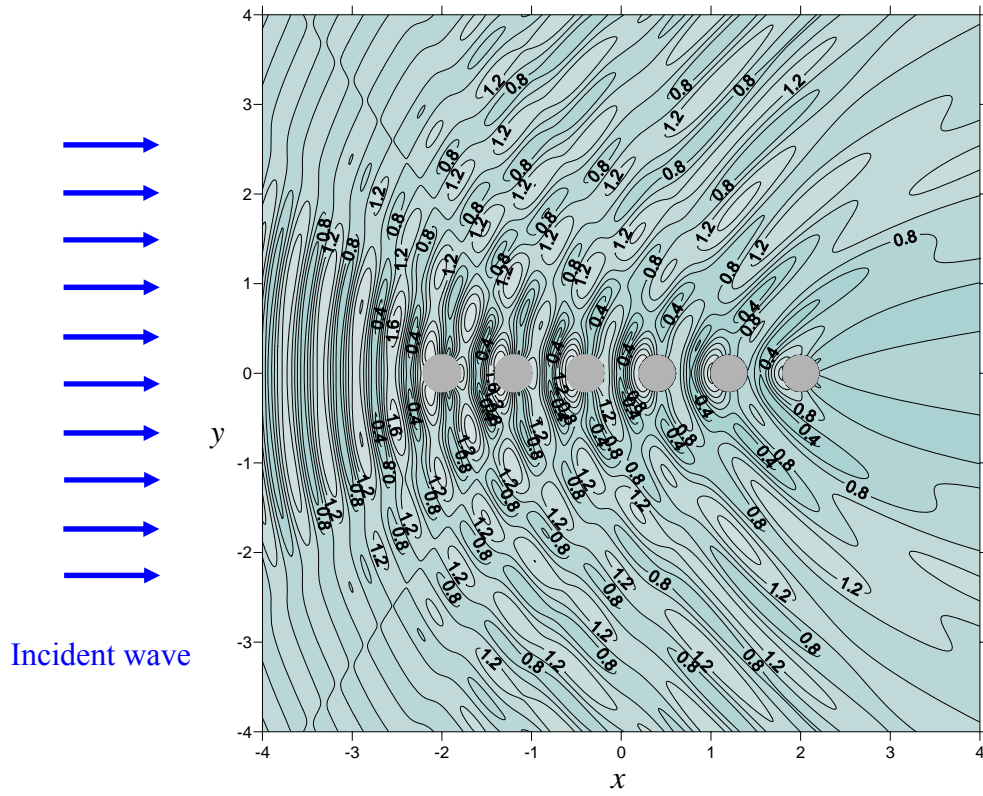
(a) Linton and Evan approach [51]



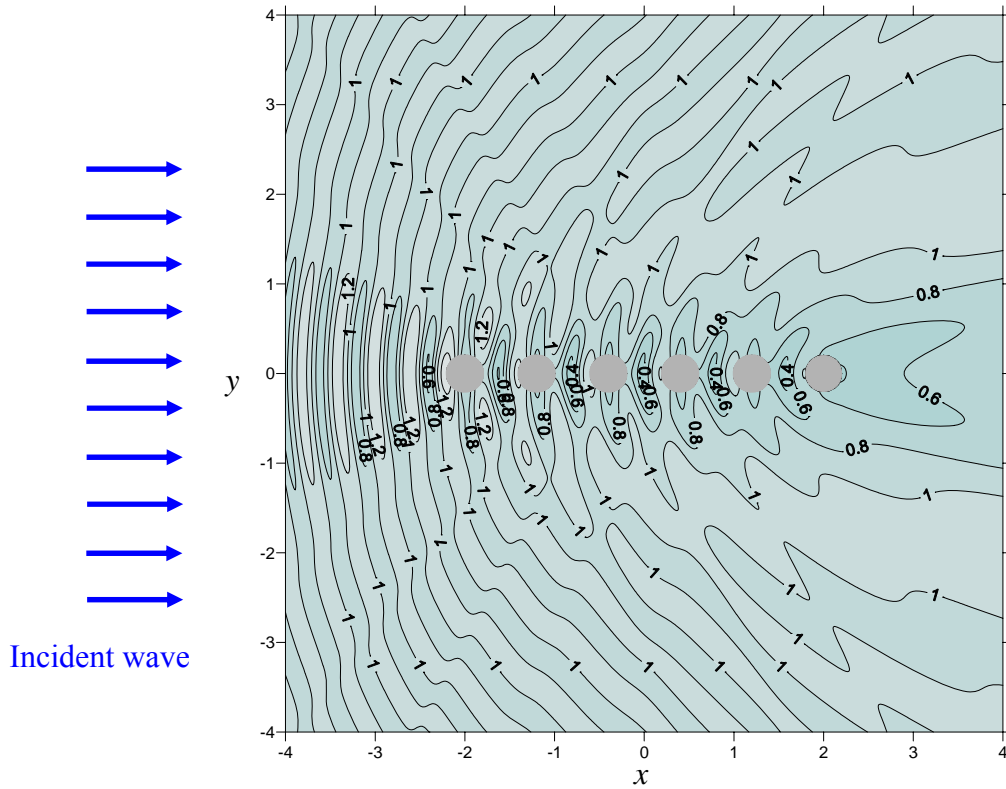
(b) Null-field BIEM ($M=20$)

Figure 3-33 Free-surface elevation of the four porous cylinders

$$(G=1.0, \theta_{inc} = 45^\circ, h/a = 5, 2b/a = 8 \text{ and } ka = \frac{\pi}{2}, H = 1)$$



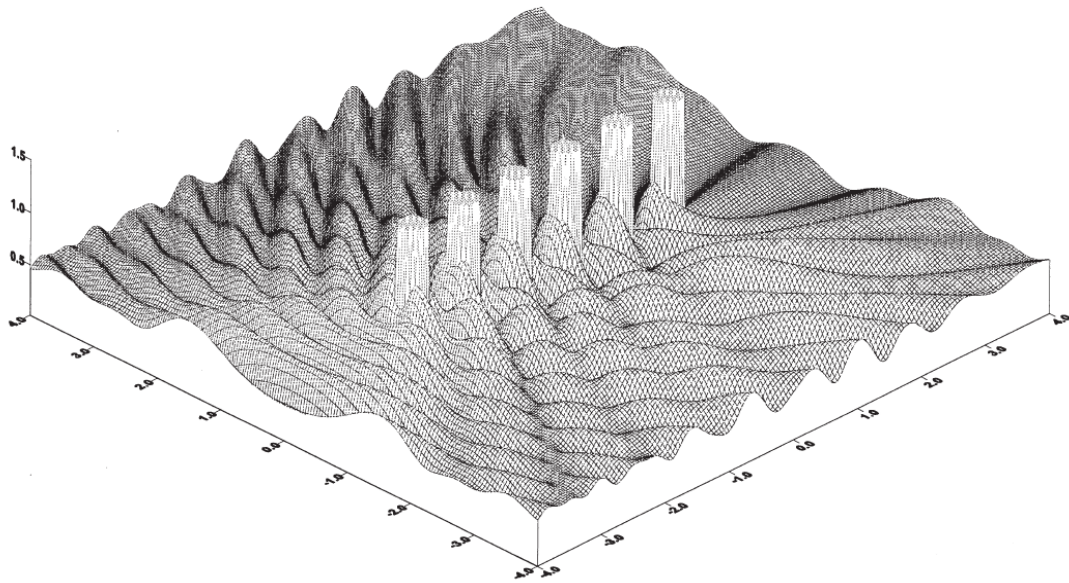
(a) Null-field BIEM ($G=0.0$, $M=20$)



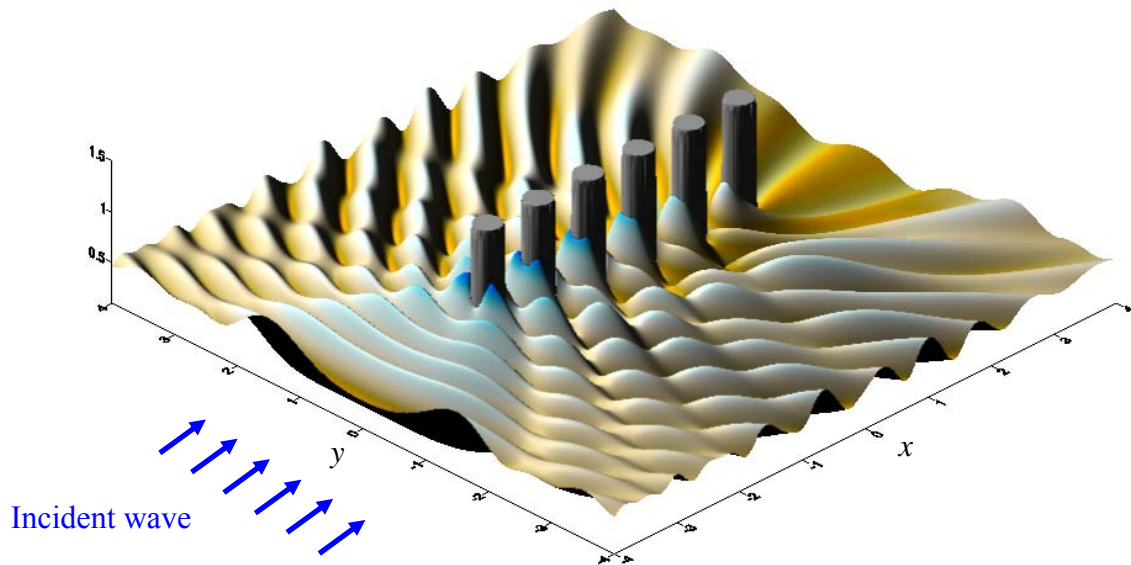
(b) Null-field BIEM ($G=1.0$, $M=20$)

Figure 3-34 Contour plots of free-surface elevation of the six cylinders

$$(\theta_{inc} = 0^\circ, h/a = 5, 2b/a = 4 \text{ and } ka = \frac{\pi}{2}, H = 2)$$



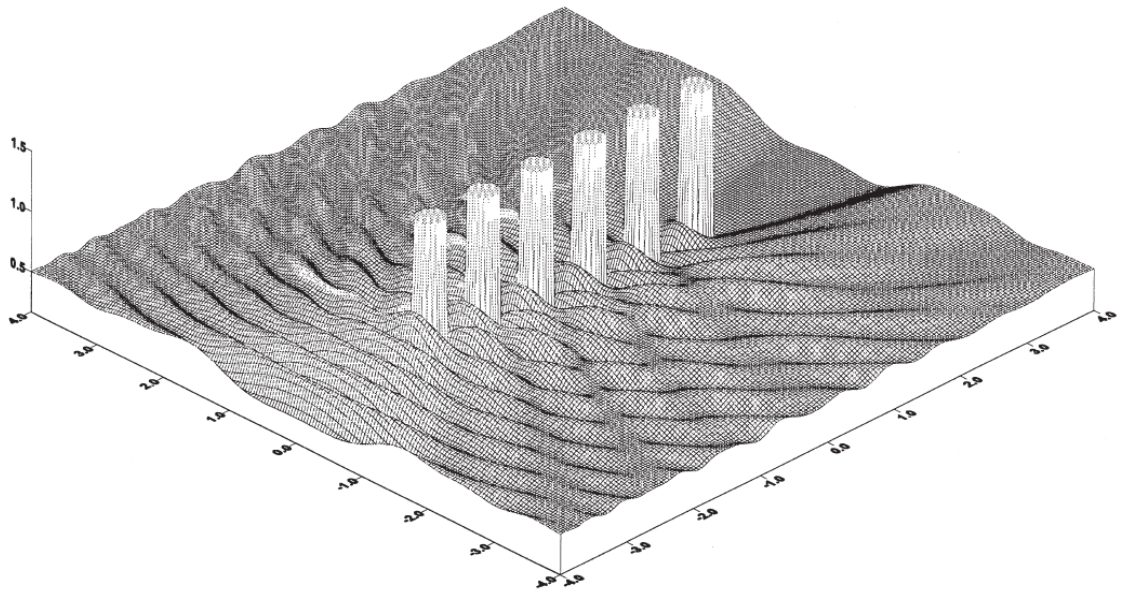
(a) Linton and Evan approach [51]



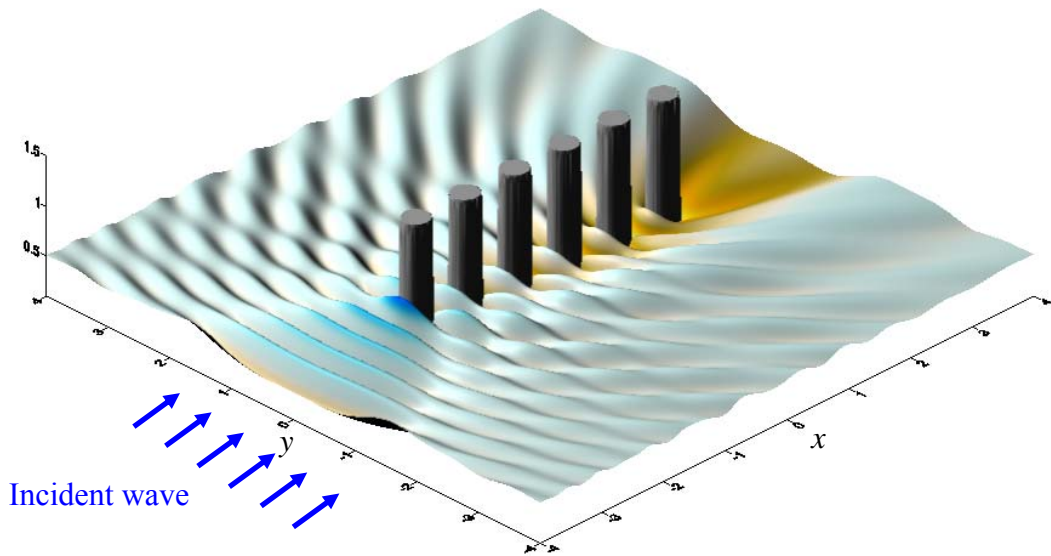
(b) Null-field BIEM ($M=20$)

Figure 3-35 Free-surface elevation of the arrays of six impermeable cylinders

$$(G=0.0, \theta_{inc} = 0^\circ, h/a = 5, 2b/a = 4 \text{ and } ka = \frac{\pi}{2}, H = 1)$$



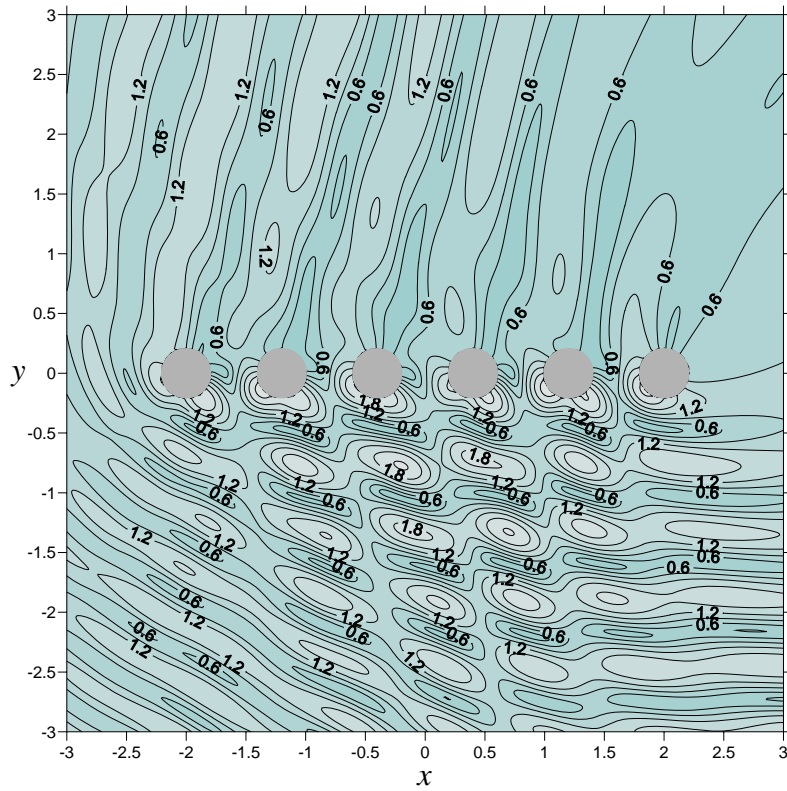
(a) Linton and Evan approach [51]



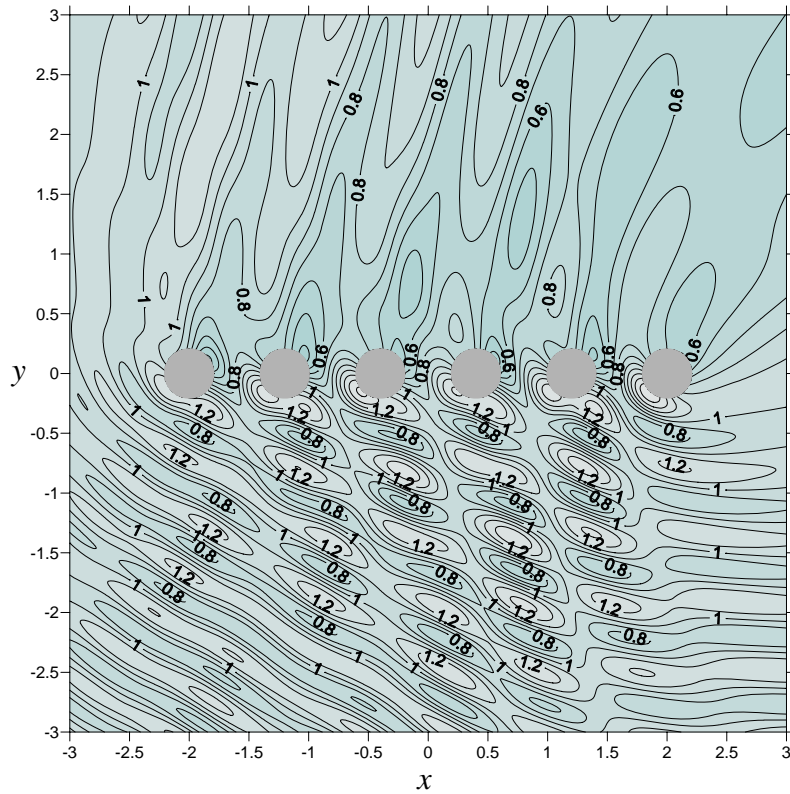
(b) Null-field BIEM ($M=20$)

Figure 3-36 Free-surface elevation of the six porous cylinders

$$(G=1.0, \theta_{inc} = 0^\circ, h/a = 5, 2b/a = 4 \text{ and } ka = \frac{\pi}{2}, H = 1)$$



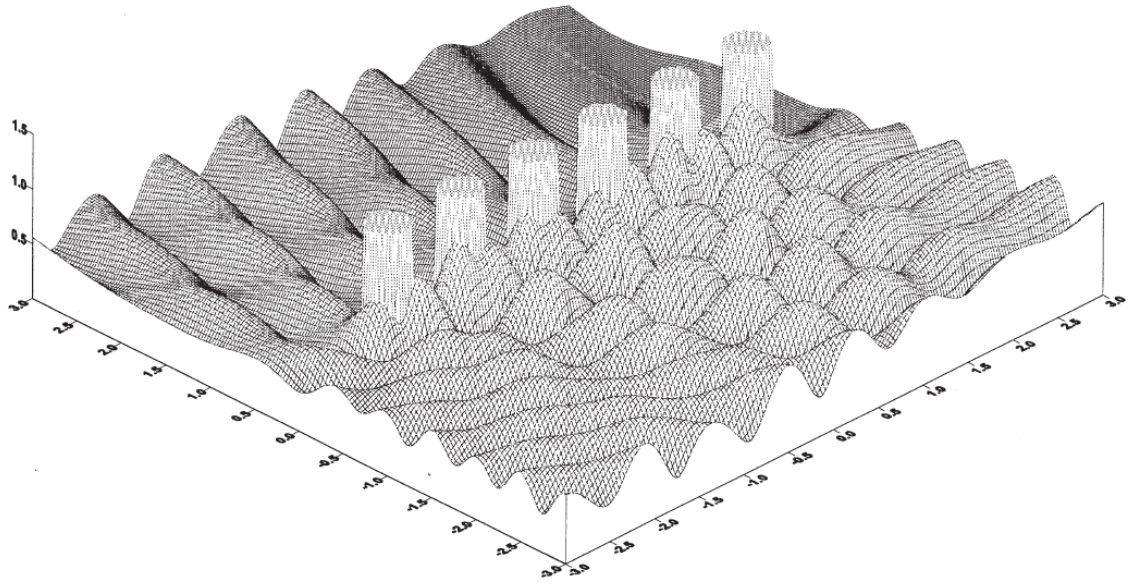
(a) Null-field BIEM ($G=0.0$, $M=20$)



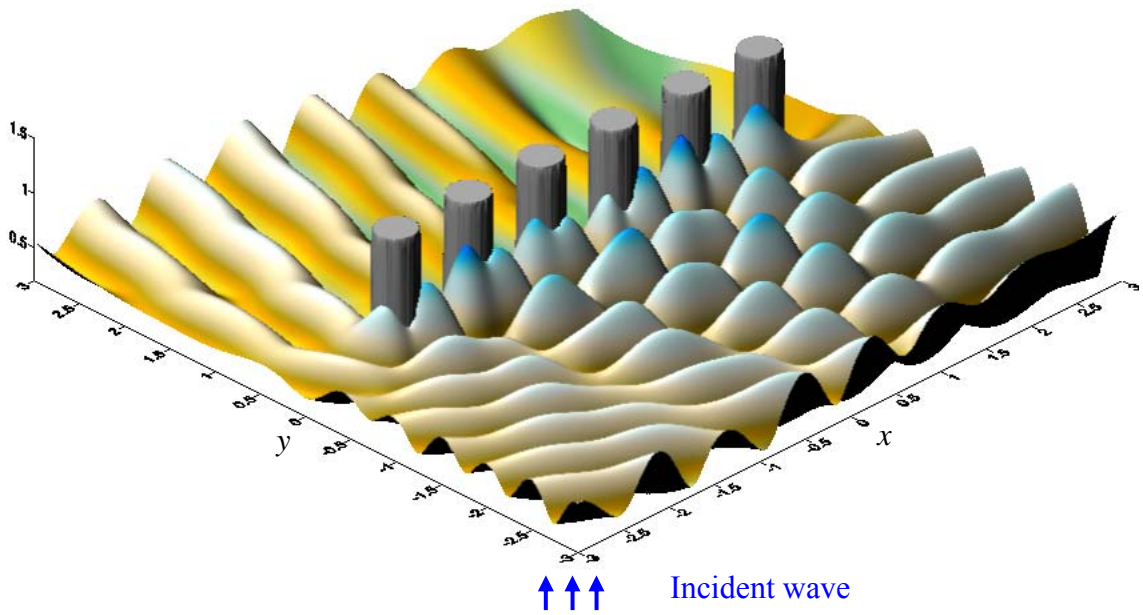
(b) Null-field BIEM ($G=1.0$, $M=20$)

Figure 3-37 Contour plots of free-surface elevation of the six cylinders

$$(\theta_{inc} = 0^\circ, h/a = 5, 2b/a = 4 \text{ and } ka = \frac{\pi}{2}, H = 2)$$



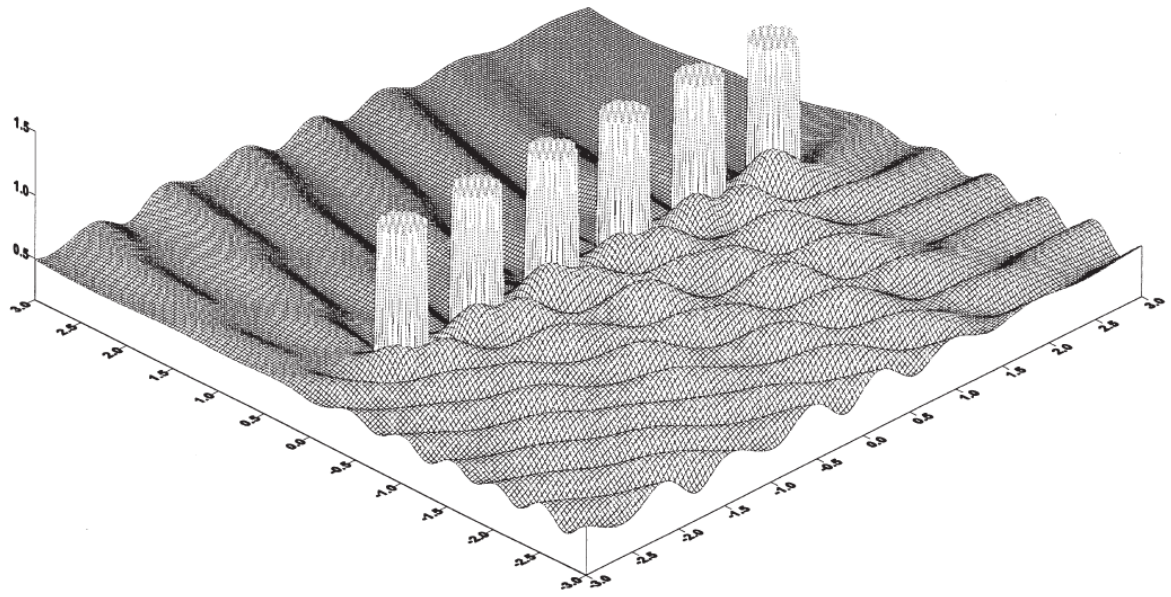
(a) Linton and Evan approach [51]



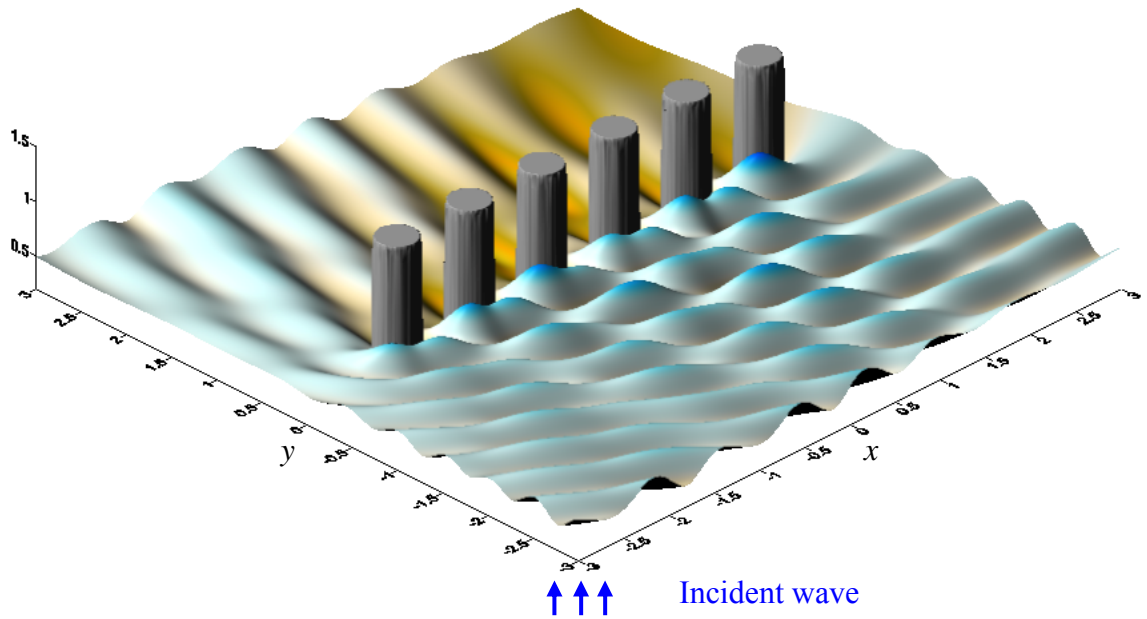
(b) Null-field BIEM ($M=20$)

Figure 3-38 Free-surface elevation of the six impermeable cylinder arrays

$$(G=0.0, \theta_{inc} = 45^\circ, h/a = 5, 2b/a = 4 \text{ and } ka = \frac{\pi}{2}, H = 1)$$



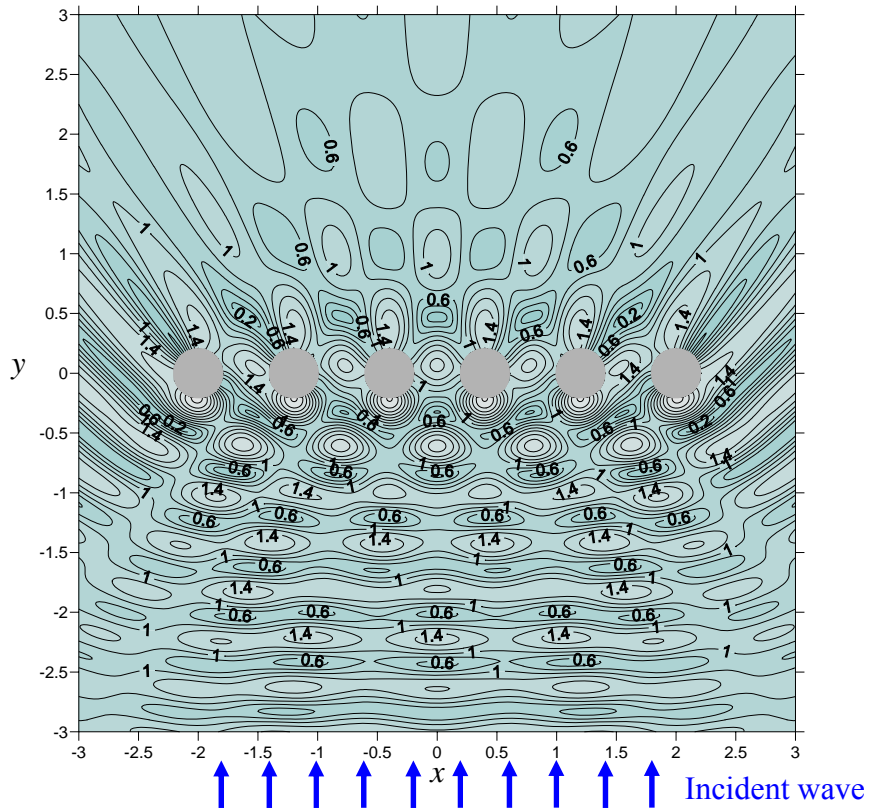
(a) Linton and Evan approach [51]



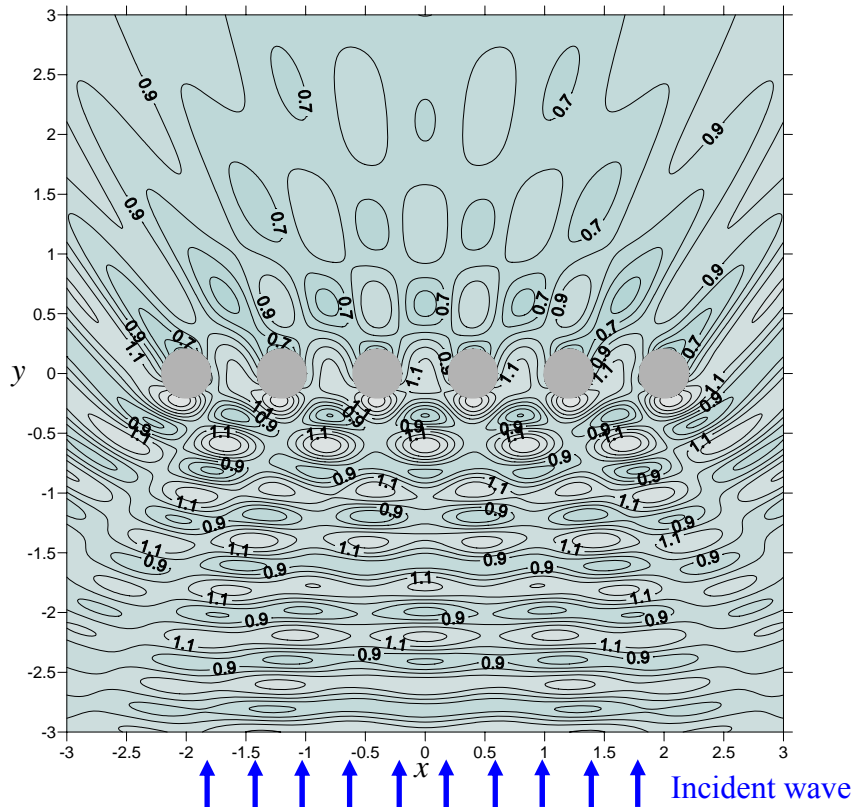
(b) Null-field BIEM ($M=20$)

Figure 3-39 Free-surface elevation of the six porous cylinders

$$(G=1.0, \theta_{inc} = 45^\circ, h/a = 5, 2b/a = 4 \text{ and } ka = \frac{\pi}{2}, H = 1)$$



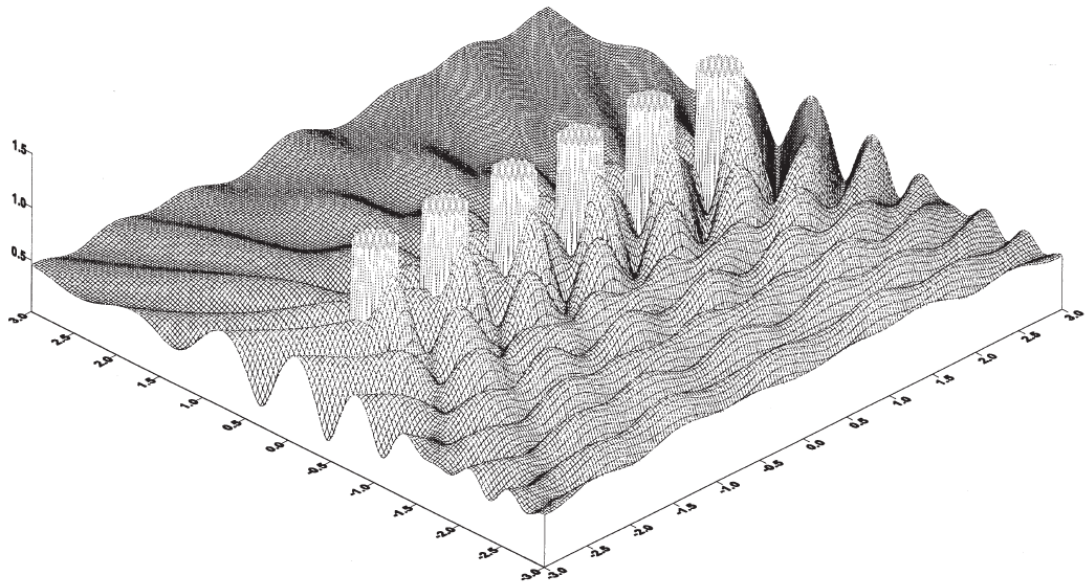
(a) Null-field BIEM ($G=0.0, M=20$)



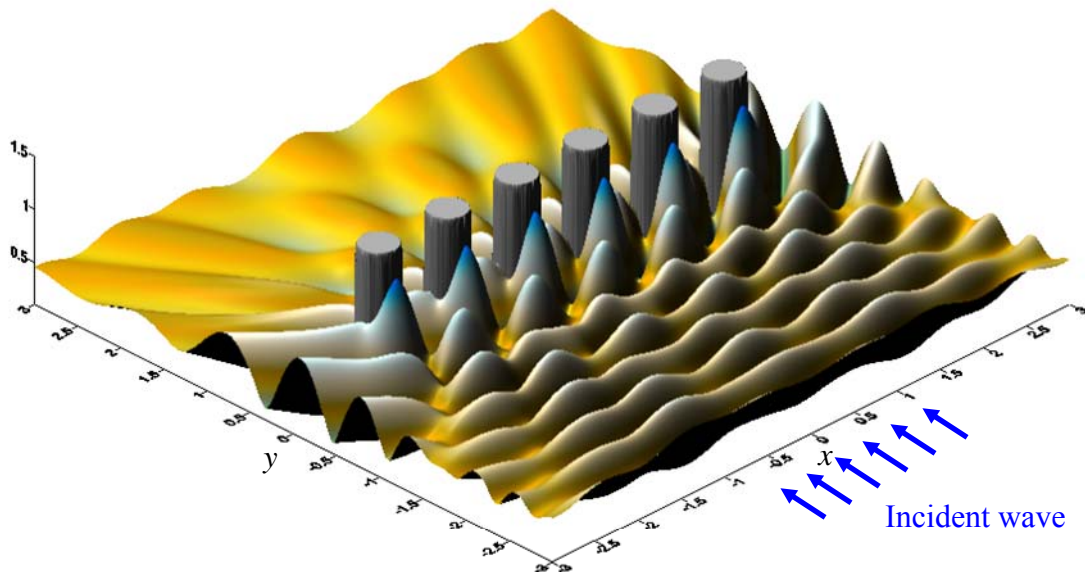
(b) Null-field BIEM ($G=1.0, M=20$)

Figure 3-40 Contour plots of free-surface elevation of six cylinders

$$(\theta_{inc} = 0^\circ, h/a = 5, 2b/a = 4 \text{ and } ka = \frac{\pi}{2}, H = 2)$$



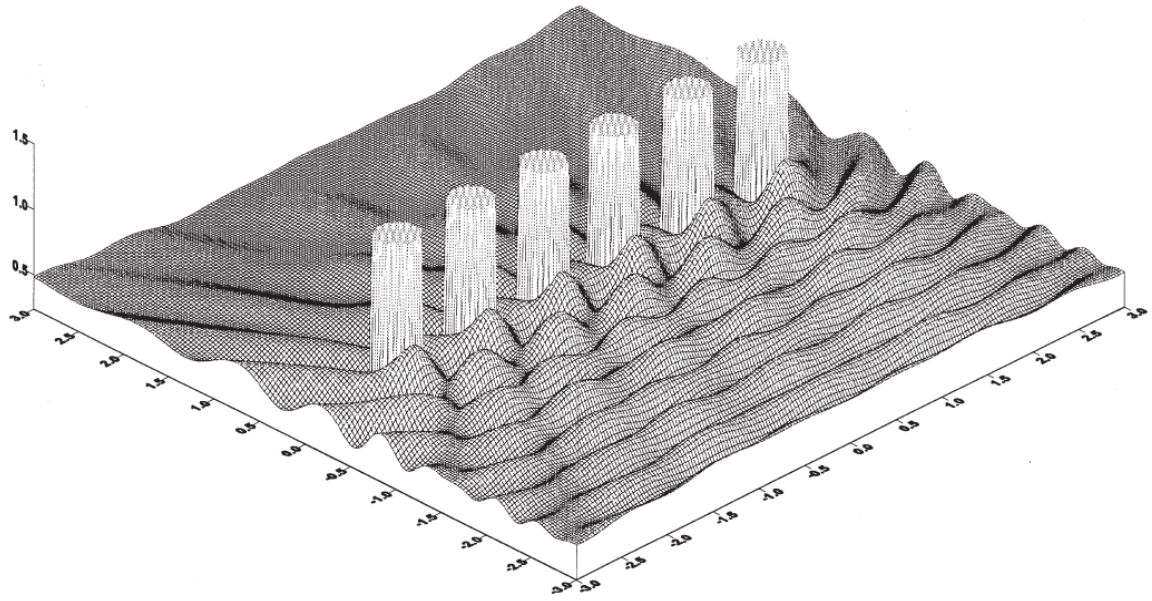
(a) Linton and Evan approach [51]



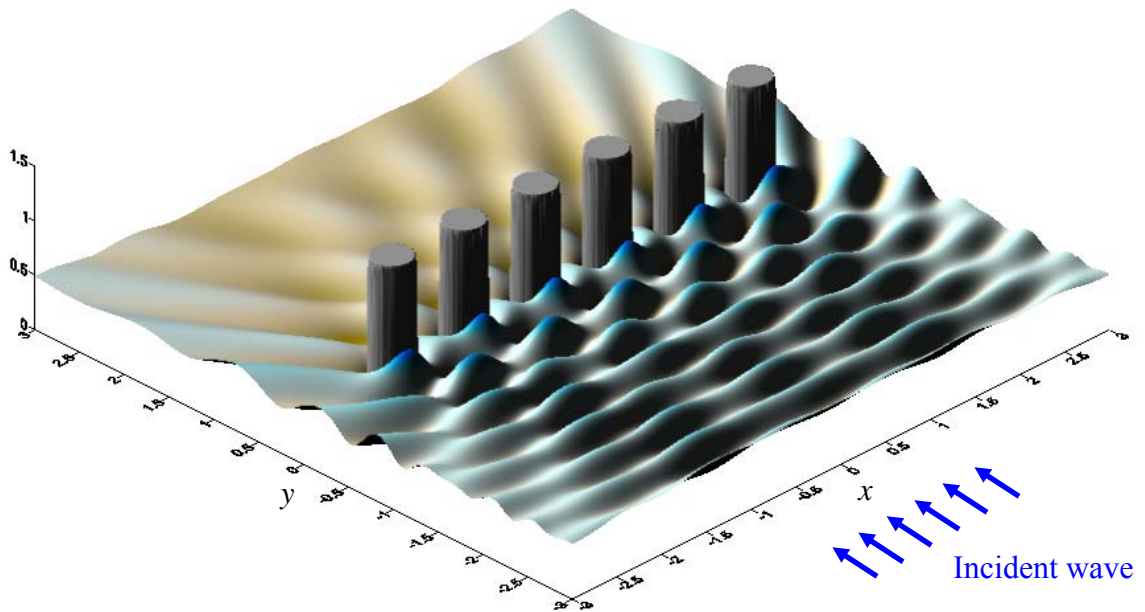
(b) Null-field BIEM ($M=20$)

Figure 3-41 Free-surface elevation of the six impermeable cylinders

$$(G=0.0, \theta_{inc} = 90^\circ, h/a = 5, 2b/a = 4 \text{ and } ka = \frac{\pi}{2}, H = 1)$$



(a) Linton and Evan approach [51]



(b) Null-field BIEM ($M=20$)

Figure 3-42 Free-surface elevation of the six porous cylinders

$$(G=1.0, \theta_{inc} = 90^\circ, h/a = 5, 2b/a = 4 \text{ and } ka = \frac{\pi}{2}, H = 1)$$

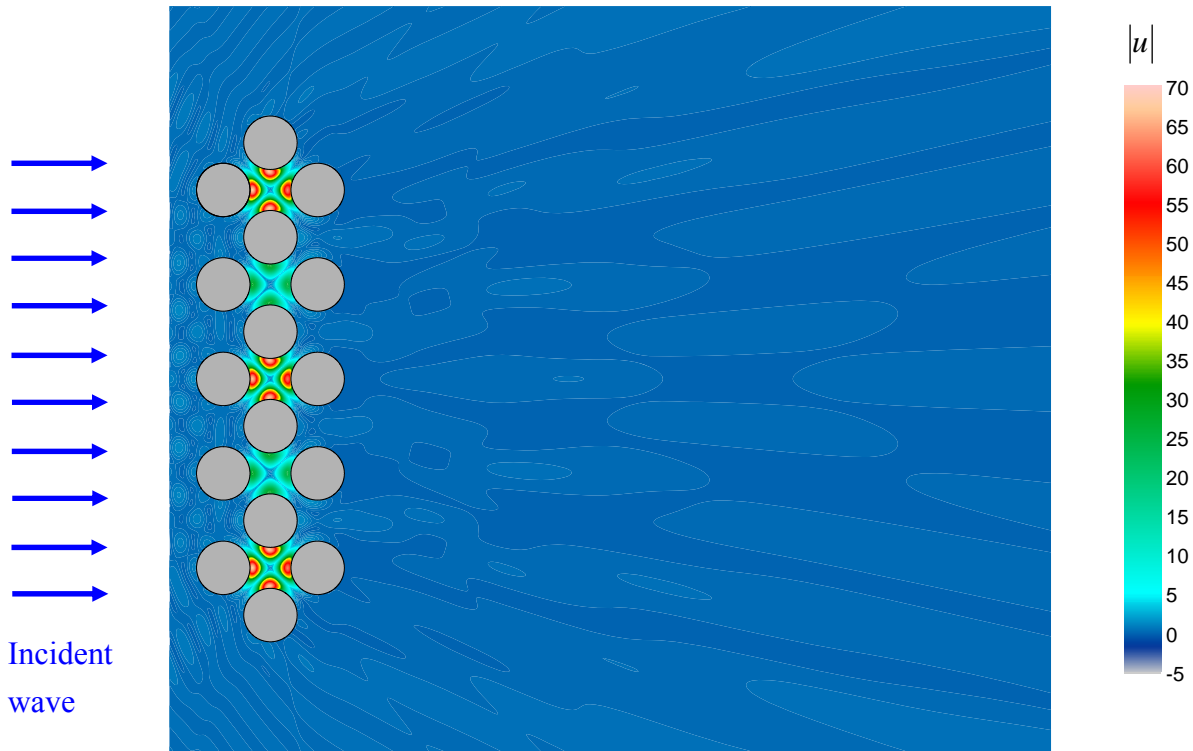


Figure 3-43 Contour of the maximum free-surface elevation amplitude for porous cylinders ($a/b=0.8, G=1.0, \tau = 0, M=20, H = 2$)

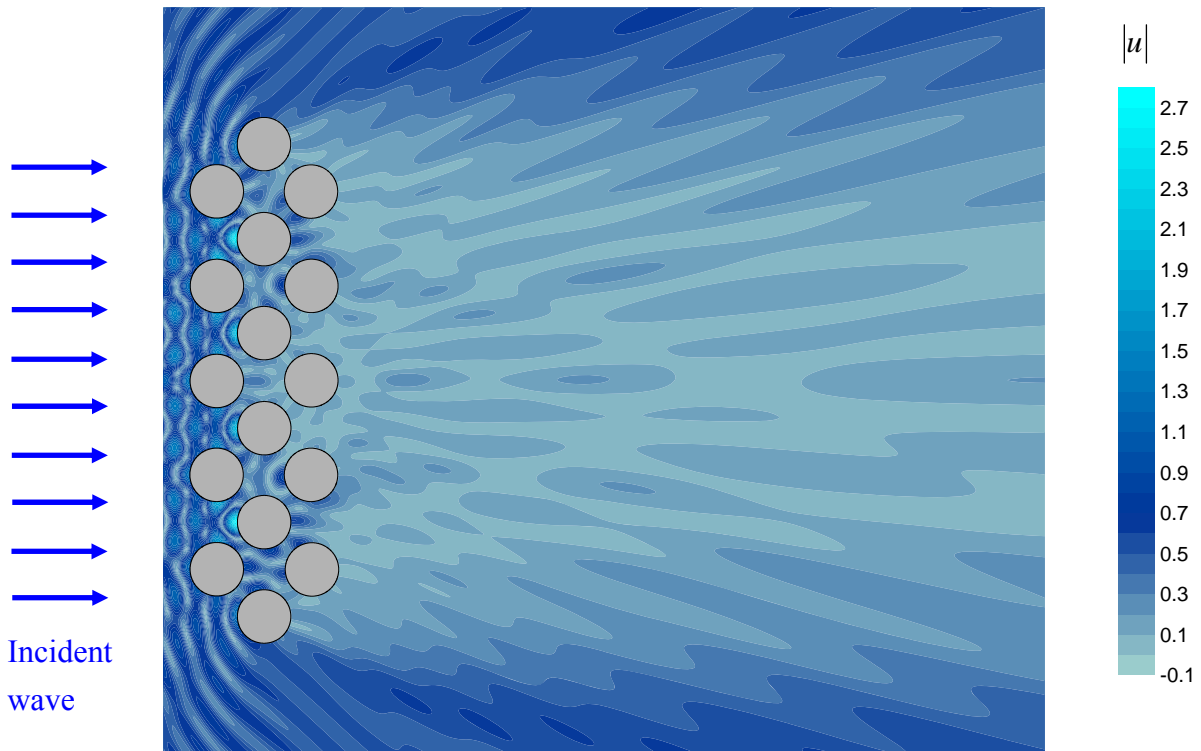


Figure 3-44 Contour of the maximum free-surface elevation amplitude for the disorder and porous cylinders ($a/b=0.8, G=1.0, \tau = 0.1, M=20, H = 2$)

Chapter 4 Conclusions and further research

4.1 Conclusions

In this thesis, we employed the null-field integral equation approach to deal with the Helmholtz problems with circular boundaries. Both acoustics and water wave problems were considered. In the context of this thesis, we have demonstrated that our approach is robust and effective. Based on the proposed formulation for solving the Helmholtz problems of exterior acoustics and water wave impinging on impermeable or porous cylinders, some concluding remarks are drawn below:

1. A systematic approach to solve the Helmholtz problems with circular boundaries and/or porous cylinders was proposed in this thesis by using the null-field integral equation in conjunction with degenerate kernels and Fourier series.
2. Calculations of principal values for singularity and hypersingularity were avoided by using degenerate kernels for interior and exterior regions separated by the circular boundary. Instead of directly calculating principal values by using the bump contour, all the boundary integrals can be performed analytically by using the degenerate kernel and Fourier expansion.
3. Parameter study of the wave number (k) was done for the two-dimensional scattering of sound from a point source by multiple circular cylinders. For the static case ($k = 0$), the Helmholtz problem can be reduced to the Laplace problem. Besides, an alternative method by limiting process ($k \rightarrow 0$) was given in the Appendix 1.
4. After introducing the degenerate kernel, the BIE is nothing more than the linear algebra for the unknown coefficients.
5. A general-purpose program for solving the Helmholtz problems with arbitrary number of circular boundaries of arbitrary radii and various positions involving the

Dirichlet and Neumann BCs was developed.

6. The effect of porous parameter and different on the near-trapped modes was also examined. Numerical results including the free-surface elevation and resultant forces on each cylinder have been presented to illustrate the effect of porous and disorder parameters on the force in case of trapped modes. Good agreement is observed after comparing with the Willam and Li's results.
7. It is found that the disorder is more sensitive to suppress the occurrence of near-trapped modes than the porosity.

4.2 Further research

In this thesis, the point sources and water wave problems have been studied by using the null-field integral equation with degenerate kernel and Fourier series. However, several issues are worth to be further investigated as follows:

1. The extension to the Helmholtz problem with a hill can be studied by using the present approach in conjunction with the multi-domain technique by decomposing the original problem into one interior problem of circular domain and a half-plane problem with a semi-circular canyon.
2. In the further research, the Helmholtz problems with circular boundaries may be extended to other shapes. Instead of incident plane wave, shore-crested incident wave can be also considered.
3. For water-wave scattering with elliptical cylinders, it deserves further study by using our approach.
4. The degenerate kernels are expanded in the polar coordinates and only problems

with circular boundaries are solved. For boundary value problems with crack, further investigation should be done.

5. In the further research, we may extend to consider problems subject to mixed-type BCs by using the null-field integral equation approach.
6. Our approach can deal with Laplace and Helmholtz problems containing circular and elliptical cylinders at the same time. It can not be solved by using Linton and Evans' analytical approach since the addition theorem to translate the polar coordinate to elliptical coordinate is not available in the literature to the author's best knowledge.
7. Although we have discussed the near-trapped mode in the thesis, another nonuniqueness problem of fictitious frequency in the BIEM needs further investigation.
8. Regarding the two-holes problem, stress concentration factor is an important issue and deserves further study.

References

- [1] **Antoine, X.; Chniti, C.; and Ramdani, K.** (2008): On the numerical approximation of High-frequency acoustic multiple scattering problems by circular cylinders. *Journal of Computational Physics*, Vol. **227**, pp. 1754-1771.
- [2] **Au, M. C.; Brebbia, C. A.** (1982): Numerical prediction of wave forces using the boundary element method. *Applied Mathematical Modelling*, Vol. **6**, pp 218-228.
- [3] **Au, M. C.; Brebbia, C. A.** (1983): Diffraction of water waves for vertical cylinders using boundary elements. *Applied Mathematical Modelling*, Vol. **7**, pp 106-114.
- [4] **Chen, H. B.; Lu, P.; Schnack, E.** (2001): Regularized algorithms for the calculation of values on and near boundaries in 2D elastic BEM. *Engineering Analysis with Boundary Elements*, Vol. **25**, pp. 851-876.
- [5] **Chen, Y. H.** (2004): Wave-induced oscillations in harbors by permeable arc breakwaters. Master Thesis, *National Taiwan Ocean University*, Keelung.
- [6] **Chen, J. T.; Hong, H. K.** (1994): Dual boundary integral equations at a corner using contour approach around singularity. *Advances in Engineering Software*, Vol. **21**, pp. 169-178.
- [7] **Chen, J. T.; Chen, K. H.; Chen, I. L.; Liu, L. W.** (2003): A new concept of modal participation factor for numerical instability in the dual BEM for exterior acoustics. *Mechanics Research Communications*, Vol. **26**, No 2, pp 161-174.
- [8] **Chen, J. T.; Shen, W. C.; Wu, A. C.** (2006): Null-field integral equations for stress field around circular holes under anti-plane shear. *Engineering Analysis with Boundary Elements*, Vol. **30**, pp. 205-217.
- [9] **Chen, J. T.; Chen, C. T.; Chen, I. L.** (2008): Null-field integral equation approach for eigenproblems with circular boundaries. *Journal of Computational Acoustics*, Vol. **15**, pp. 1-28.

- [10] **Chen, J. T.; Chen, P. Y.; Chen, C. T.** (2008): Surface motion of multiple alluvial valleys for incident plane SH-waves by using a semi-analytical approach. *Soil Dynamics and Earthquake Engineering*, Vol. **28**, pp. 58-72.
- [11] **Chen, J. T.; Chen, C. T.; Chen, P. Y.; Chen, I. L.** (2007): A semi-analytical approach for radiation and scattering problems with circular boundaries. *Computer Methods in Applied Mechanics and Engineering*, Vol. **196**, pp. 2751-2764.
- [12] **Chen, J. T.; Chou, K.H.; Kao, S.K.** (2008): Derivation of Green's function using addition theorem. *Mechanics Research Communications*, Vol. **32**, pp. 108-121
- [13] **Chen, J. T.; Lee, W. M.; Liao, H. Z.** (2008): Isotropic clamped-free thin annular circular plate subjected to a concentrated load. *ASME Journal of Applied Mechanics*, Vol. **75**, pp. 658-663.
- [14] **Chen, J. T.; Ke, J. N.** (2008): Derivation of anti-plane dynamic Green's function for several circular inclusions with imperfect interfaces. *Computer Modeling in Engineering and Science*, Vol. **29**, pp. 111-135.
- [15] **Chen, J. T.; Shen, W. C.** (2009): Null-field approach for Laplace problems with circular boundaries using degenerate kernels. *Numerical Methods for Partial Differential Equations*, Vol. **25**, pp. 63-86
- [16] **Chen, J. T.; Lee, Y. T.; Lin, Y. J.** (2009): Interaction of water waves with arbitrary vertical cylinders using null-field integral equations. *Applied Ocean Research*, Accepted.
- [17] **Chen, J. T.; Chen, C. T.; Chen, P. Y.; Chen, I. L.** (2007): A semi-analytical approach for radiation and scattering. *Computer Methods in Applied Mechanics and Engineering*, Vol. **196**, pp. 2751-2764.
- [18] **Chatjigeorgiou, I. K.; Mavrakos, S. A.** (2009): Hydrodynamic diffraction by multiple elliptical cylinders. *The 24th International Workshop on Water Waves and Floating Bodies*, Zelenogorsk, Russia.
- [19] **Crouch, S. L.; Mogilevskaya, S. G.** (2003): On the use of Somigliana's formula and Fourier series for elasticity problems with circular boundaries. *International Journal for Numerical Methods in Engineering*, Vol. **58**, pp.

- 537-578.
- [20] **Duclos, G.; Clément, A. H.** (2004): Wave propagation through arrays of unevenly spaced vertical piles. *Ocean Engineering*, Vol. **31**, pp. 1655-1668.
- [21] **Evans, D. V.; Porter, R.** (1997): Trapped modes about multiple cylinders in a channel. *Journal of Fluid Mechanics*, Vol. **339**, pp. 331-356.
- [22] **Evans, D. V.; Porter, R.** (1999): Trapping and near-trapping by arrays of cylinders in waves. *Journal of Fluid Mechanics*, Vol. **35**, pp. 149-179.
- [23] **Golberg, M. A.** (1995): The method of fundamental solutions for Poisson's equation. *Engineering Analysis with Boundary Elements*, Vol. **16**, pp. 205-213.
- [24] **Golberg, M. A.; Chen, C. S.; Bowman, H.; Power, H.** (1998): Some comments on the use of radial basis functions in the dual reciprocity method. *Computational Mechanics*, Vol. **22**, pp. 61-69.
- [25] **Golberg, M. A.; Chen, C. S.; Bowman, H.** (1999): Some recent results and proposals for the use of radial basis functions in the BEM. *Engineering Analysis with Boundary Elements*, Vol. **23**, pp. 285-296.
- [26] **Golberg, M. A.; Chen, C. S.; Ganesh, M.** (2000): Particular solutions of 3D Helmholtz-type equations using compactly supported radial basis functions. *Engineering Analysis with Boundary Elements*, Vol. **24**, pp. 539-547.
- [27] **Guiggiani, M.** (1995): Hypersingular boundary integral equations have an additional free term. *Computational Mechanics*, Vol. **16**, pp. 245-248.
- [28] **Gray, L. J.; Manne, L. L.** (1993): Hypersingular boundary integrals at a corner. *Engineering Analysis with Boundary Elements*, Vol. **11**, pp. 327-334.
- [29] **Henin, B. H.; Elsherbeni, A. Z.; Sharkawy, M. A.** (2007): Oblique incidence plane wave scattering from an array of circular dielectric cylinders. *Progress In Electromagnetics Research*, Vol. **68**, pp. 261-279.
- [30] **Kress, R.** (1989): Linear integral equations, *Springer-Verlag*, Berlin.
- [31] **Li Z. C.; Lu T. T.; Hu H. Y.; Cheng A. H. D.** (2007): Trefftz and Collocation Methods. *WIT press*, Southampton, Boston.
- [32] **Lee, W. M.; Chen, J. T.; Lee, Y. T.** (2007): Free vibration analysis of circular plates with multiple circular holes using indirect BIEMs. *Journal of Sound and Vibration*, Vol. **304**, pp. 811-830.

- [33] **Longuet-higgins, M. S.** (1967): On the trapping of wave energy round islands. *Journal of Fluid Mechanics*, Vol. **29**, pp. 781-821.
- [34] **Love, A. E. H.** (1966): Some problems of geodynamics. *Cambridge university press*.
- [35] **Linton, C. M.; Evans, D. V.** (1990): The interaction of waves with arrays of vertical circular cylinders. *Journal of Fluid Mechanics*, Vol. **215**, pp. 549-569.
- [36] **Linton, C. M.; McIver, P.** (2007): Embedded trapped modes in water waves and acoustics. *Wave Motion*, Vol. **45**, pp. 16-29.
- [37] **Morse, P. M.; Feshbach, H.** (1978): Methods of theoretical physics, New York: McGraw-Hill.
- [38] **Martin, P. A.** (2006): Multiple Scattering. Interaction of time-harmonic waves with N obstacles. New York: Cambridge University Press.
- [39] **Maniar, H. D.; and Newman, J. N.** (1997): Wave diffraction by a long array of cylinders, *Journal of Fluid Mechanics*, Vol. **339**, pp. 309-330.
- [40] **Mogilevskaya, S. G.; Crouch, S. L.** (2001): A Galerkin boundary integral method for multiple circular elastic inclusions. *International Journal for Numerical Methods in Engineering*, Vol. **52**, pp. 1069-1106.
- [41] **MacCamy, R. C.; Fuchs, R. A.** (1954): Wave force on piles: A diffraction theory. *Technical Memorandum No. 69 U. S. Army Coastal Engineering Research Center (formerly Beach Erosion Board)*.
- [42] **Pao, Y. H.** (1983): Elastic waves in solids. *ASME Journal of Applied Mechanics*, Vol. **50**, pp. 1152-1983.
- [43] **Row, R. V.** (1953): Microwave diffraction measurements in a parallel-plate region. *Journal of Applied Physics*, Vol. **24**, pp. 1448-1452.
- [44] **Row, R. V.** (1955): Theoretical and experimental study of electromagnetic scattering by two identical conducting cylinders. *Journal of Applied Physics*, Vol. **26**, pp. 666-675.
- [45] **Sherer, S. E.** (2004): Scattering of sound from axisymmetric sources by multiple circular cylinders. *The Journal of the Acoustical Society of America*, Vol. **115**, pp. 488-496
- [46] **Snodgrass, F. E.; Mund, W. H.; Miller, G. R.** (1962): Long period waves over

- California's continental borderland, part I. background spectra. *Journal of marine research*, Vol. **20**, pp. 3-30.
- [47] **Spring, B. H.; Monkmeyer, P. L.** (1974): Interaction of plane waves with vertical cylinders. Proceeding 14th International Conference on Coastal Engineering, pp. 1828-1845.
- [48] **Sladek, V.; Sladek, J.** (1991): Elimination of the boundary layer effect in BEM computation of stresses. *Communications in Applied Numerical Methods*, vol. **7**, pp. 539-550.
- [49] **Thompson, I.; Linton, C. M.; Porter, R.** (2008): A new approximation method for scattering by long finite arrays. *The Quarterly Journal of Mechanics and Applied Mathematics*, Vol. **25**, pp. 333-352.
- [50] **Wu, T. W.** (2000): Boundary Element Acoustics: Fundamentals and Computer Codes. University of Kentucky, USA.
- [51] **Williams, A. N.; Li, W.** (2000): Water wave interaction with an array of bottom-mounted surface-piercing porous cylinders. *Ocean Engineering*, Vol. **27**, pp. 841-866.
- [52] **Xie, H.; Nogami, T.; Wang, J. G.** (2003): A radial boundary node method for two-dimensional elastic analysis. *Engineering Analysis with Boundary Elements*, Vol. **27**, pp. 853-862.
- [53] **Yousif, H. A.; Köhler, S.** (1988): Scattering by two penetrable cylinders at oblique incidence. *Journal of the Optical Society of America*, Vol. **5**, pp. 1085-1096.
- [54] **Zhu, S. P.; Moule, G.** (1996): An Efficient Numerical Calculation of Wave Loads on an Array of Vertical Cylinders. *Applied Mathematical Modelling*, Vol. **20**, pp. 26-33.

Appendix 1 Limiting case of Helmholtz problem to Laplace case ($k \rightarrow 0$)

	Helmholtz operator	Laplace operator
Governing equation	$(\nabla^2 + k^2)u(\mathbf{x}, \mathbf{s}) = \delta(\mathbf{s} - \mathbf{x})$	$\nabla^2 u(\mathbf{x}, \mathbf{s}) = \delta(\mathbf{s} - \mathbf{x})$
Fundamental solution	$U(\mathbf{s}, \mathbf{x}) = \frac{-iH_0^{(1)}(kr)}{4}$ $= \frac{-i[J_0(kr) + iY_0(kr)]}{4}$ $= \frac{[Y_0(kr) - iJ_0(kr)]}{4}$ $\text{Re} \left\{ \frac{[Y_0(kr) - iJ_0(kr)]}{4} \right\}$ $= \frac{[Y_0(kr)]}{4} \sim \frac{\ln(kr)}{2\pi}$	$U(\mathbf{s}, \mathbf{x}) = \frac{\ln r}{2\pi}$
Limiting case	<p>(1) $\frac{\ln(kr)}{2\pi} - \frac{\ln r}{2\pi} = \frac{\ln(k)}{2\pi}$</p> <p>(2) Substitution $k \rightarrow 0.000001$ yields</p> $\frac{[Y_0(0.000001r)]}{4} - \frac{\ln(0.000001r)}{2\pi} = -0.018451073776577953$ <p>$c = -0.018451073776577953$</p> <p>(3) $\frac{1}{2\pi} \left(\ln \frac{kr}{2} \right) - \frac{\ln r}{2\pi} = \frac{1}{2\pi} (\ln k - \ln 2)$</p> <p>(4) Substitution $k \rightarrow 0.000001$ yields</p> $\frac{[Y_0(0.000001r)]}{4} - \left[\frac{1}{2\pi} (\ln(r) + \ln(0.000001) - \ln 2) \right]$ <p>$c = 0.09186672629915323$</p> <p>(5) $\frac{1}{2\pi} \left(\ln \frac{k}{2} + \gamma \right) = \frac{1}{2\pi} (\ln k - \ln 2 + \gamma)$</p> <p>$\gamma = 0.5772156649015328$ Euler constant</p>	
$u(\mathbf{x})$	$u(\mathbf{x}) = \frac{-iH_0^{(1)}(kr)}{4} + \text{complementary solution} + \frac{1}{2\pi} (\ln k - \ln 2 + \gamma)$	

作者簡歷

中文姓名：林羿州

英文姓名：Yi-Jhou Lin

出生日期：民國 74 年 08 月 31 日

籍貫：台灣省雲林縣

聯絡地址：台北縣土城市學府路一段 98 巷 30 號 11 樓

聯絡電話：(02) 2270-5455

行動電話：0912004490

電子信箱：M96520007@mail.ntou.edu.tw

學 歷：

國立台灣海洋大學河海工程研究所碩士 (2007.09 ~ 2009.07)

國立雲林科技大學營建工程學系 (2005.09 ~ 2007.06)

私立德霖技術學院(原四海工商專校)土木工程系 (2000.09 ~ 2005.06)



著作目錄：

(A) 期刊論文

- 1 **Chen J. T.; Lee Y. T.; Lin Y. J.** (2009): Interaction of water waves with arbitrary vertical cylinders using null-field integral equations, *Applied Ocean Research*, Accepted.
- 2 **Chen J. T.; Kao S. K.; Lee Y. T.; Lin Y. J.** (2009): On the spurious eigenvalues for a concentric sphere in BIEM, *Applied Acoustics*, Revised.
- 3 **Chen J. T.; Lee Y. T.; Lin Y. J.; Chen I. L.** (2008): Scattering of sound from point sources by multiple circular cylinders using addition theorem and superposition technique, Submitted.
- 4 **Chen J. T.; Lin Y. J.; Lee Y. T.** (2009): Water wave interaction with surface-piercing porous cylinders using the null-field integral equations, Submitted.

(B) 會議論文

- 1 **Lin, Y. J.; Lee, Y. T.; Chen, I. L.; Chen, J. T.** (2008): Scattering of sound from point sources by multiple circular cylinders using addition theorem and superposition technique, *The 32nd National Conference on Theoretical and Applied Mechanics*, Chia-Yi, Taiwan.
- 2 **Lin, Y. J.; Lee, Y. T.; Lee J. W.; Chen, J. T.** (2009): Trapping and near-trapping by arrays of porous cylinders in water waves using the addition theorem and superposition technique, *Computational Fluid Dynamics Conference*, Yilan-July, Taiwan.
- 3 **Lin, Y. J.; Lee, Y. T.; Chen, J. T.** (2009): Trapping and near-trapping by arrays of cylinders in water waves using the addition theorem and superposition technique, *CSHydro 2009 Conference*, Keelung, Taiwan.